

Subcellular processes in morphogen gradient formation studied with 3D tracking fluorescence microscopy Holtzer, L.H.F.M.

Citation

Holtzer, L. H. F. M. (2008, December 8). Subcellular processes in morphogen gradient formation studied with 3D tracking fluorescence microscopy. Casimir PhD series 2009-19, Delft-Leiden. Retrieved from https://hdl.handle.net/1887/14504

Version: Corrected Publisher's Version

Licence agreement concerning inclusion of doctoral

License: thesis in the Institutional Repository of the University

of Leiden

Downloaded from: https://hdl.handle.net/1887/14504

Note: To cite this publication please use the final published version (if applicable).

Subcellular processes in morphogen gradient formation studied with 3D-tracking fluorescence microscopy

Laurentius Henricus Franciscus Maria Holtzer

Subcellular processes in morphogen gradient formation studied with 3D-tracking fluorescence microscopy

Proefschrift

ter verkrijging van de graad van Doctor aan de Universiteit Leiden, op gezag van Rector Magnificus prof.mr. P.F. van der Heijden, volgens besluit van het College voor Promoties te verdedigen op dinsdag 8 december 2009 klokke 13.45 uur

door

Laurentius Henricus Franciscus Maria Holtzer

geboren te Steenbergen (NB) in 1980

Promotiecommissie:

Promotor: Prof. dr. T. Schmidt

Referent: Prof. dr. M. González-Gaitán (Université de Genève, Zwitserland)

Overige Leden: Prof. dr. P.-R. ten Wolde (AMOLF, Amsterdam)

Prof. dr. N. H. Dekker (Technische Universiteit Delft)

Prof. dr. H. P. Spaink Prof. dr. M. Orrit Prof. dr. T. J. Aartsma Dr. ir. S. J. T. van Noort

Prof. dr. J. M. van Ruitenbeek

©2009 Laurent Holtzer. All rights reserved.

Cover: Marjolein van Esch

ISBN 978-90-8593-064-8

Casimir PhD Series, Delft-Leiden 2009-19

The work described in this thesis was performed at the University of Leiden, Niels Bohrweg 2, 2333 CA Leiden and is financially supported by the Human Frontier Science Program and the Dutch CYTTRON consortium, sponsored by the Dutch Ministry of Economic Affairs.

Contents

1	Intr	oduction		1	
	1.1	1 The morphogen gradient			
		1.1.1 Morphogens .		2	
		1.1.2 Dpp		2	
		1.1.3 Morphogen spi	reading	4	
	1.2	2 Particle tracking in cells and tissue			
		1.2.1 Single-molecul	e and single-particle localization	6	
		1.2.2 Positional accu	racy	11	
		1.2.3 Tracking		13	
		1.2.4 Trajectory anal	ysis	14	
		1.2.5 Applications .		17	
		1.2.6 Conclusion		23	
	1.3	Scope of this thesis		23	
2	3D 7	racking of Quantum D	ote in calle	33	
_		•			
	2.1	Introduction		34	
	2.2		three dimensions	35	
	2.3		od	37 40	
	2.4	2.4 Conclusion			
	2.5				
	2.A				
		2.A.1 Derivations		42	
		2.A.2 Extension to in	nage stacks	45	
3	Intr	acellular Dpp transport	studied with PICCS	49	
	3.1			50	
	3.2	Intracellular transport	of Dpp	52	
	3.3	-	rrelation spectroscopy		

vi CONTENTS

	3.4	Materials and Methods				
	3.5 Results and discussion					
	ısion					
	3.A		dix			
		3.A.1	Theory - Intracellular trafficking			
		3.A.2	Theory-Particle image cross-correlation spectroscopy.			
		3.A.3	Bleaching			
		3.A.4	Error scaling in PICCS			
4	Endo	osome r	notility and endosomal cargo dynamics	83		
	4.1	Introd	uction	84		
		4.1.1	Intracellular Dpp transport	85		
	4.2	Materi	als and methods	89		
		4.2.1	Sample preparation	89		
		4.2.2	Data acquisition	89		
		4.2.3	Data analysis	91		
	4.3	Results	s-Endosome mobility	96		
		4.3.1	Intracellular transport by endosomes			
		4.3.2	Axial endosomal movement			
	4.4	Results	s-Dpp content of endosomes	103		
		4.4.1	Static characterization	103		
		4.4.2	Dynamic characterization	105		
	4.5	Conclu	asion	113		
Sai	menva	atting		117		
Cu	rricul	lum Vit	ae	125		
Lis	st of P	ublicati	ions	127		
Da	nkwo	ord		129		

Chapter 1

Introduction

One of the most fundamental questions in life is how an organism grows and develops from a single cell into a fully grown adult. A major step forward in solving this question was the discovery of the molecule that contains all the information needed by an organism: DNA. It was further found that every cell in an organism contains an exact copy of this DNA. This immediately posed another question: how do cells, while having the exact same DNA, know where they are located in the organism and what functions they should perform. How does a cell know whether it is a kidney cell and not a heart or brain cell, and even more, how does it know where it is located within the kidney?

The work described in this thesis addresses some aspects of this question by studying a model system, the wing imaginal disc of the fruit fly larva. While the cells in this disc are very similar, they still are able to determine where they are located within the wing by detecting the concentration of specific proteins, called morphogens. These morphogens are produced locally within the tissue and form a gradient throughout the tissue. Morphogens play a key role in growth and patterning of the organism. The subcellular processes that govern the formation, the maintenance and the shape of the morphogen gradient are the main focus of this thesis. This introductory chapter discusses the subjects in the current study: morphogen gradients, endosome transport and single-particle tracking in cells and tissue. It also gives an outline of the scope of this thesis.

1.1 The morphogen gradient

1.1.1 Morphogens

Almost 60 years ago Turing proposed that morphogens are providing the positional information for cells in developing organisms in which they are expressed in all the cells in the tissue [1]. Wolpert in turn proposed that morphogens are actually produced by spatially localized special cells. By spreading throughout the tissue morphogens form a gradient in the neighboring cells, the receiving tissue [2]. There the morphogen is detected by receptors on the cell surface. Depending on the morphogen concentration cells will adapt their gene expression pattern. Figure 1.1 shows a schematic drawing of a morphogen gradient.

Most of the models describing morphogen gradients assume, and experiments have proven, that the system is in a steady state. The formation of morphogen gradients occurs in a much shorter period than the time needed for patterning tissue [3]. In general two models exist that describe a steady morphogen gradient in tissue. When degradation takes place at a discrete location a linear gradient forms [3], while if degradation occurs in all the receiving cells, the morphogen gradient will have an exponential shape [4]. Experimentally the latter was found to be the case in the wing imaginal disc of the fruit fly *Drosophila melanogaster* in which the morphogens Decapentaplegic (Dpp) and Wingless (Wg) play an essential role during development of the wing of the fly [5].

1.1.2 Dpp

Decapentaplegic (Dpp) is a morphogen of size 77 kDa which controls the patterning and development of the different imaginal discs in the fruit fly *Drosophila melanogaster*. The name decapentaplegic comes from the observation that in most *dpp* mutants at least 15 of the 19 imaginal discs show defects [6] (fifteen=decapenta in Latin). Among those discs two, the wing imaginal discs, will develop later into the wings of the fly.

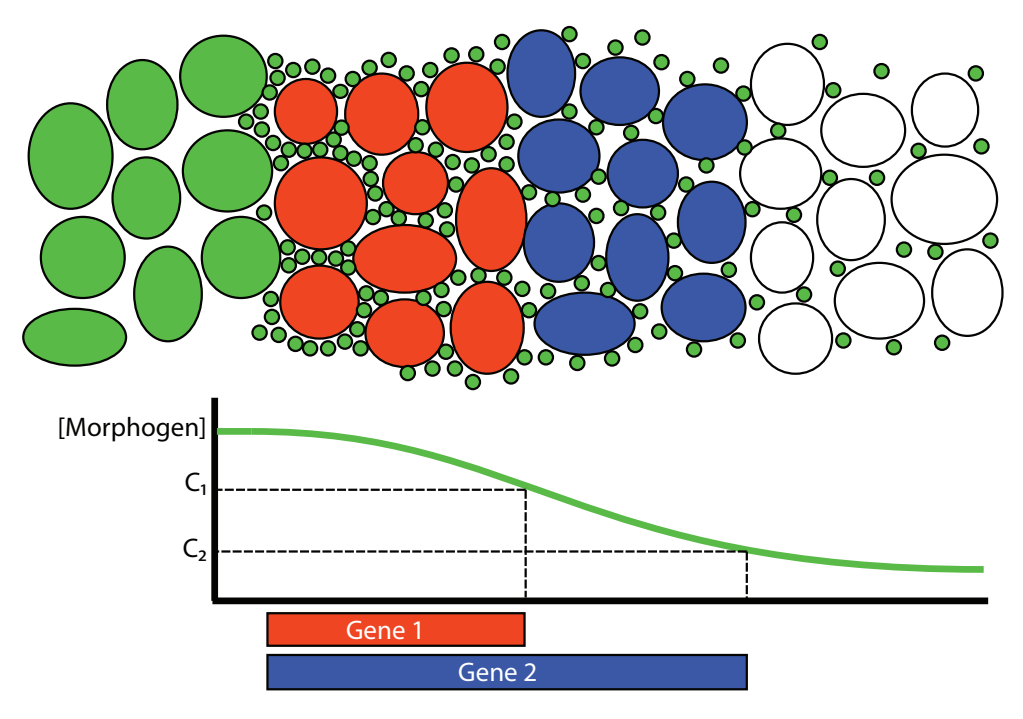


Figure 1.1: Schematic drawing of a morphogen gradient. Morphogens (small green circles) are produced in spatially localized cells (green) and form a gradient in the receiving tissue. Receiving cells express genes (red and blue) depending on the morphogen concentration (C_1 and C_2)

Dpp is a member of the TGF- β superfamily and is homologous to the vertebrate Bone Morphogenetic Protein (BMP). Dpp takes part in a major developmental signaling pathway. The receptor for Dpp was found to be composed of Thickveins (Tkv) [7] and Punt [8]. After formation of the Dpp-receptor complex the intracellular protein Mad (Mothers against dpp) is phosphorylated. Subsequently pMad controls activation of transcription of its target genes *optomotor-blind* (*omb*) and *spalt* (*sal*) in a Dpp concentration-dependent manner [9]. Optomotor-blind is a requirement for the development of the wing [10], Spalt plays a role in the formation and positioning of specific veins in the wing [11]. Besides playing a role in the Dpp signaling pathway, the Dpp receptor is also required for Dpp-receptor internalization. This process plays a major role in Dpp spreading and degradation [12–15].

In the wing imaginal disc Dpp is produced at the anterior-posterior compartment boundary [16] from which it is secreted to the neighboring receiving cells. Dpp forms a steady-state single-exponential gradient which can fully be described by three parameters: the production rate, the diffusion constant and the degradation rate [4].

1.1.3 Morphogen spreading

The spreading of Dpp in the receiving cells has been a subject of study for many years. In most of those studies (confocal) microscopy supplemented with dynamic techniques like fluorescence recovery after photobleaching (FRAP) were combined with sophisticated genetic technologies in order to describe the morphogen gradient and its spreading in terms of a coarse-grained concentration profile in the tissue. Those experiments suggest that Dpp is spread by three different mechanisms:

- 1. Diffusion in the extracellular matrix [17];
- 2. Receptor-mediated transport [18];
- 3. Intracellular transport [12], i.e. multiple endocytosis and subsequent recycling events into the extracellular matrix [19].

The extracellular diffusion and receptor-mediated transport are governing short-range spreading, while intracellular transport is essential for long-range spreading [20]. Theoretical calculations have estimated that one cycle of intracellular transport has a duration between 50 and 150 s [19, 21].

In the current thesis we strive to extend the settled coarse-grained models of intracellular Dpp transport to a more molecular model that involves endosome-mediated Dpp transport. We studied endosome transport by 3D fluorescence microscopy. The experimental approach will be outlined in the next section.

1.2 Particle tracking in cells and tissue¹

For long microscopy has been one of the primary techniques in biological investigation. In particular light microscopy which allows one to directly observe biological processes *in vivo* is used on an every-day's basis in biology laboratories. One of the characteristics of a system *in vivo* - or a live system - is the constant movement of all its components. The mobility of ions, small molecules like ligands, proteins whether membrane-bound [22–29] or located in the cytosol [30–32], and larger assemblies like vesicles [33, 34], the nucleus [35] or viruses [36], is finally determining the way how the system evolves and self-regulates. Hence, in a strive to understand living systems on a microscopic mechanistic basis one wants to characterize the mobility of its components and combine this knowledge to the functional state of the system.

The two main classes of mobility, i.e. unrestrictive diffusion and linear directed motion, are rather the exception in the context of the complex environment of the cell and tissue [37, 38]. Proteins, for example, might for some time diffuse freely through the cytosol. However, due to binding events or restriction in their diffusional space, their mobility may become slowed on longer time and length scales. Likewise a vesicle, which is immobile for an

¹This section is based on: L. Holtzer and T. Schmidt, Single-Molecule Tracking in Cells and Tissue in 'Single Particle Tracking and Single Molecule Energy Transfer: Applications in the Bio and Nano Sciences', C. Bräuchle, J. Michaelis and D.C. Lamb (eds.), Wiley 2009.

initial phase of observation, could be actively transported at a later phase due to molecular motors which follow a microtubular track [39–42]. Recording and classification of such complex mobility behavior in a statistically significant manner asks for a significant and careful effort in technology development and automated analysis tools to render successful.

In what follows we describe the foundations for the technology developed by us and others in order to permit tracking of individual molecules and small molecular assemblies. We will mainly focus on applications in biomembranes, in cells and in tissue, and illustrate by selected examples how biological information is extracted by a detailed analysis of molecular mobility.

1.2.1 Single-molecule and single-particle localization

The use of wide-field fluorescence microscopy allows for parallel, hence fast data acquisition. It is therefore the most appropriate technology for tracking moving molecules and objects. In wide-field fluorescence microscopy an isotropic emitter smaller than the diffraction limit will appear as a diffraction limited spot in the image plane [43]. Its image is characterized by a symmetrical signal distribution around the center with the maximum intensity at the center of the spot. The intensity distribution I(x, y) of such an object on a highly-sensitive CCD camera used in the experiments described, is determined by the point spread function (PSF). A good approximation of the PSF is given by a two-dimensional Gaussian with full-width-at-half-maximum (FWHM) equal to $w = 1.03\lambda/\text{NA}$, with λ the wavelenght of the emitted light and NA the numerical aperture of the microscope objective [22, 44, 45]:

$$I(x,y) = N \frac{4 \ln 2}{\pi w^2} \exp \left[-4 \ln 2 \left(\frac{(x - \mu_x)^2}{w^2} + \frac{(y - \mu_y)^2}{w^2} \right) \right]$$
(1.1)

where μ_x and μ_y are the x and y coordinates of the object, and N the total number of detected photon-counts. It should be mentioned that the positions are determined with nanometer precision although the typical size of the generated image, w, is larger than the object [46]. This fact is called super-resolution and will be described in detail later.

Identification of individual molecules is complicated by unavoidable background signals in living cells due to out-of-focus objects and autofluorescent particles. Therefore image pre-processing and reliable background removal is necessary. It turned out that background signals are satisfactorily removed by applying a spatial low-pass filter to the image with a cut-off frequency of 5/w, frequencies which are far below the frequencies generated by the objects of interest. Subtraction of the filtered image from the original image reliably yields an image with a zero background. Likewise static objects are faithfully removed using a temporal low-pass filter on the movie stack and subsequently subtracted from the original image. The latter method needs to be applied carefully in order not to remove slowly moving or static objects of interest.

After appropriate background subtraction automatic object identification and position analysis is performed. An easy and fast way to determine the position of the object in the object plane is calculating the center of mass, or centroid, of its image for each axis

$$\mu_{x} = \sum_{i=1}^{M_{y}} \sum_{j=1}^{M_{x}} (x_{i} \cdot \mathbf{I}_{ij}) / \sum_{i=1}^{M_{y}} \sum_{j=1}^{M_{x}} \mathbf{I}_{ij}$$
 (1.2)

where I_{ij} is the signal at a pixel (i, j) [47, 48]. It is important that the fluorescence intensity of the image has no offset, as this will bias the position of the particle towards the center. Advantage of this method is that it does not use any prior knowledge about the shape of the intensity profile and can therefore be applied to objects even in case of imaging errors or to objects which are larger than the diffraction limit [49].

The most reliable but computationally more demanding method of determining the position of an object is by fitting the image to the 2D Gaussian intensity profile of the PSF as presented in eq. (1.1), see fig. 1.2a,b. A fit of the intensity distribution to eq. (1.1) determines the position of the object with nanometer precision (fig. 1.2c) [28, 46]. The accuracy is thereby inversely proportional to the signal-to-noise ratio, approximated by $w/\sqrt{8N\ln 2}$ [50]. The approximation assumes that additional noise due to background signals is negligible. In typical applications using autofluorescent molecules a positional ac-

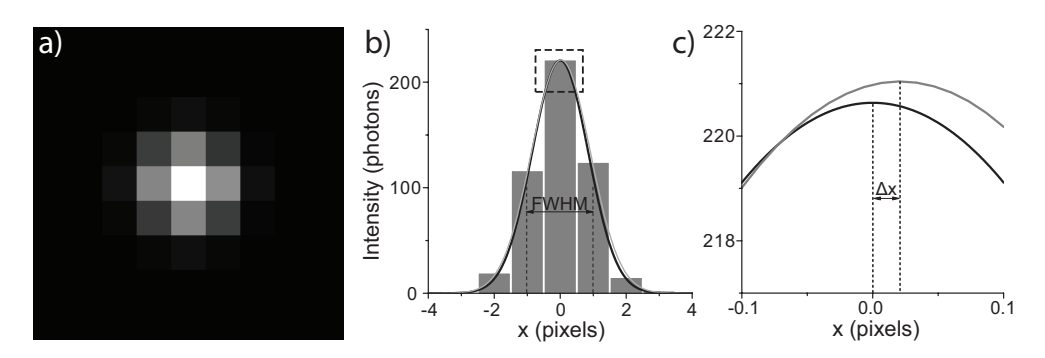


Figure 1.2: **a**) Simulated image of a diffraction limited spot approximated by a 2D Gaussian intensity profile. Poisson noise was added to account for the stochastic nature of photon emission (w = 2 pixels, N = 1000). **b**) Intensity of the image along a horizontal line through the center. In black a 1D Gaussian is shown calculated directly from the input parameters. A fit to the data is shown in gray. **c**) A closer look at the part of (b) indicated by the square. It can be clearly seen that the Gaussian fit determines the position of the particle with high accuracy ($\Delta x = 0.02$ pixels).

curacy of < 30 nm is achieved at video rate (e.g. a frame rate of 25 Hz) [27, 51].

Positional determination as described so far solely allows to extract information on the lateral position of an object. In recent years several methods to determine also the axial position have been described [52–60]. A straightforward and cost-effective method to determine the z-position of a single particle is by introducing a slight astigmatism into the detection beampath [50, 61]. A schematic drawing of the experimental setup is shown in fig. 1.3. This method will be extensively described in chapter 2 of this thesis. The axial accuracy which is obtained by using this method is about 2.5 times that of the lateral positional accuracy. Typically < 75 nm is achieved in live cell experiments.

The one-plane approach as described above allows one to determine axial positions within the Rayleigh-range of \sim 1 μ m. For larger image volumes simultaneous imaging of multiple planes onto one CCD chip must be employed. This is achieved by inserting a beamsplitter in front of the CCD to create two light paths with different image distances [62, 63]. Another comparable method was

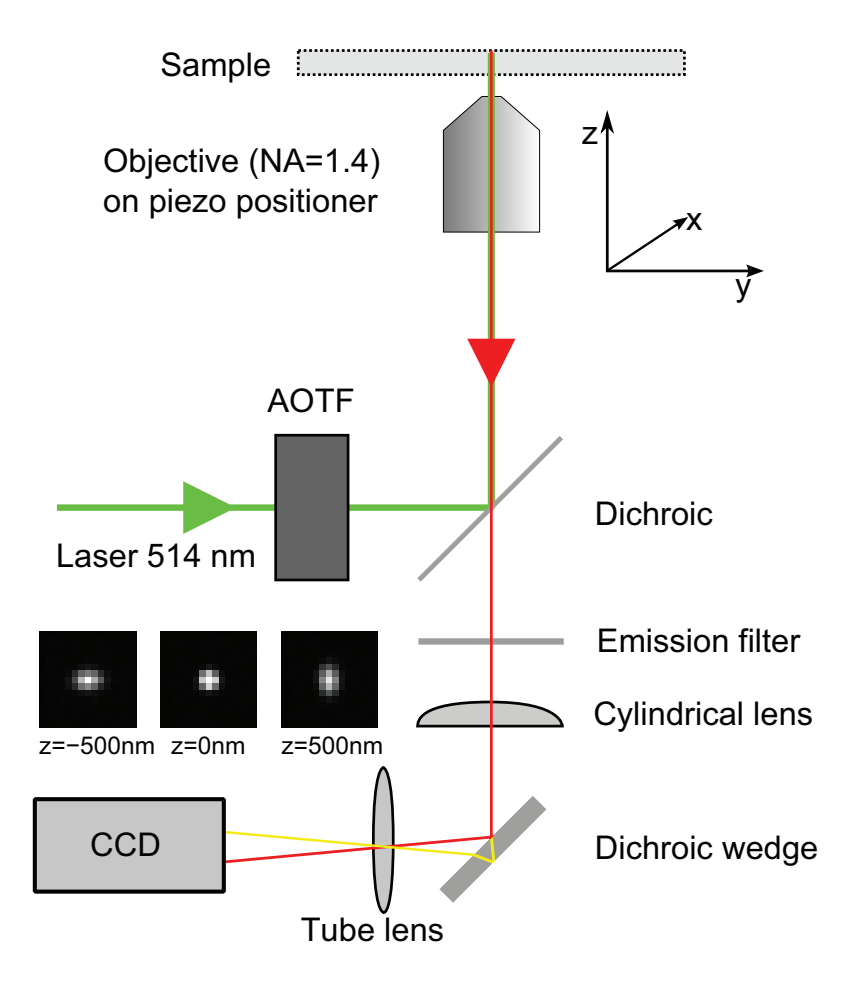


Figure 1.3: Schematic drawing of a 3D wide field fluorescence setup. An AOTF (Acousto-Optic Tunable Filter) is used to select the desired excitation wavelength. The dichroic mirror separates the emitted light from the excitation beam and the emission filter selects for the emission wavelength of the fluorescent molecule. A cylindrical lens (f = 10 m) is introduced to obtain accurate information about the z-position. Finally a dichroic wedge is installed to separate two different fluorescent dyes. The three images shown at three different z-position are of a particle that is imaged using this setup and showing the effect of the cylindrical lens.

developed in which multiple cameras were used each focusing on a different plane in the sample [64, 65]. While the latter method has the advantage that a larger volume can be imaged at a faster rate, it is very costly and more complex software is needed to synchronize all the elements in the setup.

In cases where image rates are less important different planes can be imaged consecutively by moving a piezo-mounted objective in axial direction. The ideal distance between the planes is given by the axial range of the astigmatism method of $\sim 1~\mu m$. Care has to be taken that these stacks of images are taken faster than the typical movement of the particle of interest to avoid movement of the particle during imaging. If this is not possible the difference in time needs to be taken into account in the data analysis. While it is still possible to fit 2D Gaussian profiles to each image in a stack, a better alternative is fitting of all images in a stack in a global fitting approach. For this the 2D Gaussian needs to be extended to 3D. While the total intensity of the Gaussian in each plane is constant, it turned out that one should allow for a varying offset per image within the stack to cope with possible differences in spurious background signal. In focal planes far from the position of the particle, the intensity will be rather spread. This effectively increases the background signal and a variable offset can compensate for this effect.

Experimental conditions in single-molecule fluorescence experiments are usually chosen such that the concentration of fluorescent molecules is low and that only a few molecules are visible in an image of typical size ($10 \times 10 \, \mu m^2$). For low densities, the distance between each molecule is large enough (> 3w) that their intensity profiles are independent. If such low densities are not achievable a recursive fitting approach needs to be applied: after the first initial round of fitting, all-but-one fitted molecules are subtracted from the image. The one molecule that is left is subsequently refitted without the influence of the others. Several of these recursive runs are needed to obtain the correct position and intensity of all individual molecules. In this way densities of up to 1 molecule/ μm^2 are reliably handled. A similar method was published recently [66].

The methods described above are further developed to allow for simultaneous imaging of multiple detection channels, separating for example different

colors or polarizations. A dichroic-wedge in the emission beam path is used to generate two separate images on the CCD coding for two colors, and/or a Wollaston prism is placed in the infinity beam path to generate two images of perpendicular polarization [67]. Such techniques are able to image two different types of particles at the same time by labeling each of the objects with different fluorescent dyes whose emission spectra are well separated. It should be noted that aberrations introduced by placing the dichroic wedge or a Wollaston prism are very small compared to the positional accuracy of the system.

1.2.2 Positional accuracy

Emission of photons is a statistical process. Hence the more photons are detected, the more accurate the position of the particle can be determined. The positional accuracy of an experimental setup depends on many factors, i.e. the camera noise, the amount of photons emitted per particle, the localization method used and the magnification of the setup. A general method to calculate the error in position measurement applied to single molecule imaging shows that the lateral positional accuracy in typical experiments is equal to 30 nm [46, 51].

A fundamental approach to specify the achievable position accuracy is calculated from the amount of information which is contained in a given dataset. This measure is called the Cramer-Rao bound (CRB) specified by the inverse of the Fisher information matrix I [68, 69]. With X the observed data and θ the unknown parameters $I(\theta) = \mathbb{E}\left\{\left[\frac{\partial}{\partial \theta} \ln f(X;\theta)\right]^2 \middle| \theta\right\}$. The CRB yields a lower bound to the variance for any unbiased estimator, i.e. in the case of imaging the precision by which the position of a single particle is determined.

As discussed before the PSF is approximated by a 2D Gaussian intensity profile (eq. (1.1)). If we assume that camera-pixelation and camera read-out-noise is negligible, the lower limit for the positional error for the experimental setup described in chapter 2 is

$$\sigma_{\mu_x} = \frac{w_r/\epsilon}{\sqrt{8N\ln 2}}$$
 ; $\sigma_{\mu_y} = \frac{w_r\epsilon}{\sqrt{8N\ln 2}}$ (1.3)

in lateral direction, and

$$\sigma_{\mu_z} = \frac{1}{\sqrt{N}} \left(\frac{\sqrt{5}z_r^2}{4(z \pm \gamma)} + \frac{\sqrt{5}}{4} (z \pm \gamma) \right) \quad \epsilon \lessgtr 1$$
 (1.4)

in vertical direction, with z_r the Rayleigh-range. Whereas $\sigma_{\mu_{xy}}$ is independent on the lateral position of the object, σ_{μ_z} varies with z and is lowest in focus. For an experimental setup without cylindrical lens $\epsilon=1$ and therefore σ_{μ_x} and σ_{μ_y} are equal and σ_{μ_z} is undefined around the focus.

In order to calculate the limit of the positional accuracy in an actual experiment one has to take into account all sources which influence the image formed on the CCD [68]. This will include camera pixelation, the position of the object relative to the center of a camera pixel, camera noise, the magnification of the setup and any other noise sources present. Furthermore, an Airy function should be used to describe the image formed by the object of interest in place of the simple Gaussian in eq. (1.1). While such extended analytical calculations of the CRB have been performed for some cases [68, 69] we have tested our strategies by means of extensive simulations in which all aspects mentioned were taken into account. The results showed an excellent overlap with the simplified approximation given in eqs. (1.3) and (1.4), see chapter 2.

The high accuracy by which individual molecules are localized has recently been utilized to greatly increase the resolution of light microscopy. In methods, now coined PALM [70], FPALM [71], STORM [72, 73] and STED [74] the positions of individual molecules are determined, to be subsequently used for generation of an image in which each molecule contributes with a PSF according to eq. (1.1) but with a width given by the positional accuracy $w/\sqrt{(8N \ln 2)}$ in place of w. In this way the 'Abbe-limit' describing the optical resolution of the microscope has been broken by an order of magnitude. It has been realized recently that in principal there is no limit to the resolution in a microscope as the resolution is solely set by the signal which can be obtained from an individual object:

$$R = 1.22 \frac{\lambda}{2\text{NA}} \frac{1}{\sqrt{N}} \tag{1.5}$$

1.2.3 Tracking

Obtaining trajectories of sparsely distributed and relatively immobile objects is straightforward [75, 76]. However, larger particle densities per frame and higher mobility of the particles renders the connection of particles in consecutive images increasingly complex [47]. The computational effort for solving such connectivity maps is equivalent to the well-known 'traveling-salesman' problem in operations research. Our tracking algorithms are based on a numerical approximation developed by Vogel for the field of operations research [77]. First a translational matrix $p_i(j,k)$ is built up that describes the probabilities that particle j in image i (containing L objects) at position $\vec{r}_{j,i}$ moves to particle k in image i+1 (containing M objects) at position $\vec{r}_{k,i+1}$ by diffusion in a d-dimensional system characterized by a diffusion constant D:

$$p_i(j,k) = \exp\left\{-\frac{(\vec{r}_{j,i} - \vec{r}_{k,i+1})^2}{2dDt}\right\}$$
(1.6)

The translational matrix further allows particles to disappear from the observed area by diffusion or photobleaching, $p(j, k > L) = p_{\text{bleach}}$, and particles are allowed to move into the observed area or get reactivated, $p(j > M, k) = p_{\text{activation}}$. Probabilities to account for particles that are accidentally not detected in an image are also included. Taken together this leads to a probability matrix p of size $\{(L + M) \times (L + M)\}$. Trajectories are constructed by optimizing the total probability of all connections between two images, $\max(\log(P) = \sum_{j,k} \log(p(j,k)))$. Even in the case of a sizable amount of molecules per image, the Vogel algorithm enhances the number of faithfully reconstructed trajectories. More elaborate algorithms have been developed for more complex systems with e.g. high particle density, particle motion heterogeneity or particle splitting or merging [78–82].

For a reliable analysis of molecular mobility, unavoidable mechanical drift must be corrected for. A simple and efficient way of drift correction is the calculation of the center-of-mass of all objects, given that a sufficient number of continuously tracked objects (n > 10) is available per frame. Such bootstraptype correction algorithms are particularly suited in diffusion-governed sys-

tems since all movements should average to zero and any deviation from zero directly measures the correction needed. In case that not sufficient continuous trajectories are available, significantly more molecular positions have to be averaged in order to reduce drift correction below the positional accuracy. For an image of size X the number of objects in that case must be larger than $(X/\sigma_{\mu_{xy}})^2$. In order to achieve a resolution of $\sigma_{\mu_{xy}} = 10$ nm in a full-view image of $X = 10 \ \mu m$, 10^6 positions must be averaged.

1.2.4 Trajectory analysis

A multitude of information is extracted from trajectories of individual objects, ranging from the diffusion constant to the presence of multiple fractions of a certain type [83, 84]. A straightforward method to obtain information about the mobility of an object is to calculate its mean squared-displacement (MSD) versus time between two observations. The MSD is the average movement of an object in a certain amount of time and is calculated for each object using

$$MSD = \langle (\Delta r_t)^2 \rangle = \frac{\sum_{i=1}^{T-t} (r_i - r_{i+t})^2}{T - t}$$
 (1.7)

in which T is the total length of the trajectory. The type of motion of the object is subsequently extracted from the MSD versus time plot. For free diffusion the MSD has a linear dependence on time

$$MSD = 2dDt_{lag} + 2d\sigma_d^2$$
 (1.8)

in which d is the dimension of the movement and σ_d the positional accuracy in d dimensions. When a particle is transported, for example by molecular motors inside a cell [36], the MSD shows a supralinear dependence on time:

$$MSD = 2dDt_{lag} + (vt_{lag})^{2} + 2d\sigma_{d}^{2}$$
 (1.9)

in which v is the velocity of the particle. A particle which is diffusing in a 2D confined area of side length L will have an associated MSD which levels off for large t_{lag} :

$$MSD = \frac{L^2}{3} \cdot \left[1 - \exp\left(\frac{-12D_0 t_{\text{lag}}}{L^2}\right) \right] + 4\sigma_{xy}^2$$
 (1.10)

in which D_0 denotes the initial diffusion constant [29].

Hence the MSD versus time behavior provides a global characterization of the type of motion. Often however this behavior is of transient nature, especially for e.g. the transport of particles like vesicles [24, 37, 85] or the motion of receptors in the cell membrane. A standard MSD-analysis will therefore fail to detect short periods of a certain type of motion within a trajectory [84]. The difficulty comes from the fact that the accuracy of a mean value for a complex motion scales inversely proportional to the square root of number of independent observations, in this particular case the number of independent motion steps within a short part of a trajectory [86]. With a rigorous method, introduced by Huet et al. [87], different types of transient motion can be detected and distinguished within a single trajectory at a probability level prior set. For each type of motion a specific parameter is calculated along the trajectory using a rolling analysis window whose width is variable.

For a stalled particle the diffusion coefficient D will be close to the detection limit of the setup. This limit can be experimentally determined using eq. (1.8) by measuring the diffusion coefficient $D_{\rm im}$ for immobilized beads on a coverslip at a signal-to-noise ratio similar to the experiment. Particles which diffuse with a diffusion constant D which is 10 times $D_{\rm min}$ are classified as mobile with high confidence. If however D for a particle, calculated from a rolling window analysis, drops below $D_{\rm min}$ for a prior set period, it is classified as being stalled during this period. To reliably obtain D it is desired to calculate the MSD from as many data points as possible, i.e. to use a large rolling window size. A linear fit to the first $N_{\rm diff}$ points of the MSD plot then gives a reliable D [86, 88]. On the other hand to detect short periods of immobilization the number of data points needs to be small. As a compromise the minimum number of time points $W_{\rm min}^{\rm stall}$ needed to calculate the MSD is set to 51, while keeping $N_{\rm diff} = 5$.

To detect confined motion we exploit the fact that the MSD of a confined particle shows downward curvature in comparison to a particle undergoing free diffusion. For small t the MSD for a confined particle is very similar to the MSD for free diffusion (see eq. (1.10)). Therefore the first $N_{\rm diff}$ points of a rolling MSD analysis are used to calculate an initial MSD for a particle undergoing simple diffusion. The deviation between the MSD for longer time lag and the

initial value is a robust parameter which indicates confined diffusion:

$$Conf = \frac{1}{N_{\text{Conf}}} \sum_{n=1}^{n=N_{\text{Conf}}} \frac{\langle r^2(n\Delta t) \rangle - \langle r^2(n\Delta t) \rangle_{\text{diff}}}{\langle r^2(n\Delta t) \rangle_{\text{diff}}}$$
(1.11)

For Conf < 0 confined mobility is likely, whereas for Conf > 0 it is unlikely. To obtain a reliable value for Conf we set $N_{Conf}/N_{diff} = 10$. Since the error in the MSD becomes increasingly large for high values of t_{lag} the number of points from the MSD curve used for calculating Conf should not exceed the first 2N/3 points of this curve.

While it is possible to detect directed motion directly from an MSD curve, it is more efficient to look at the shape of a trajectory, as directed motion will lead to a highly asymmetric trajectory. For this the radius of gyration tensor of a trajectory, $\mathbf{R}_{\mathbf{g}}$, is calculated:

$$\mathbf{R_g}(i,j) = \langle r_i r_j \rangle - \langle r_i \rangle \langle r_j \rangle \tag{1.12}$$

where r_i and r_j are the three axes and the averages are defined over all N_{Asym} steps of the analyzed rolling window. Typically $N_{\text{Asym}} = N_{\text{diff}}$. The radii of gyration for each direction are the square roots of the eigenvalues $\mathbf{R_g}$. From those, the asymmetry parameter is calculated:

$$Asym = -\log\left(1 - \frac{(R_1^2 - R_2^2)^2 + (R_1^2 - R_3^2)^2 + (R_2^2 - R_3^2)^2}{2(R_1^2 + R_2^2 + R_3^2)^2}\right)$$
(1.13)

For *Asym* > 1 directed motion is likely, whereas for *Asym* < 1 directed motion is unlikely.

To reliably detect different types of motion there is an obvious tradeoff between statistical significance and window size. These values depend on the system under study and thus several typical trajectories are used to optimize the values for a particular sample. In the case of Huet et al. and in our own studies the minimum window size $W_{\min}^{\text{conf}} = 75$ consecutive time points for confined motion, and $W_{\min}^{\text{dir}} = 11$ consecutive time points for directed motion.

When single particle trajectories are too short to calculate the MSD on a single trajectory with sufficient accuracy (typically one needs 100 consecutive

time points) the displacements of all particles in adjacent frames are analyzed. For the 2D case, the cumulative distribution function (cdf) for the squared displacements r^2 is [22]

$$P(r^2, t_{\text{lag}}) = 1 - \exp\left(-\frac{r^2}{\text{MSD}(t_{\text{lag}})}\right)$$
(1.14)

 $P(r^2, t_{\text{lag}})$ describes the probability that a particle starting at the origin will be found in a circle of radius r after a time t_{lag} . The cdf is very useful for a system where there are two fractions of a certain particle, which are experimentally only distinguishable by their different D [27, 89, 90]. For two fractions eq. (1.14) becomes

$$P(r^2, t_{\text{lag}}) = 1 - \left[\alpha \cdot \exp\left(-\frac{r^2}{\text{MSD}_1(t_{\text{lag}})}\right) + (1 - \alpha) \cdot \exp\left(-\frac{r^2}{\text{MSD}_2(t_{\text{lag}})}\right)\right]$$
(1.15)

in which α indicates the fraction size, and $MSD_1(t_{lag})$ and $MSD_2(t_{lag})$ the two mean squared-displacements at t_{lag} , respectively. It should be noted, that such ensemble-type analysis does not even require a previous, computationally demanding, trajectory analysis as outlined in the section 1.2.3. The position data can be likewise directly analyzed using particle image correlation analysis (PICS) as developed by Semrau et al. [91].

1.2.5 Applications

The examples in figs. 1.4 to 1.6 show that the previously described techniques are powerful tools to obtain information about biological systems. Figure 1.4 provides an example coming from an experiment where the diffusional behavior of several membrane anchors (K-Ras, H-Ras and Lck) in live cells is compared to study the occurrence and size of lipid rafts in the cytoplasmic leaflet [92]. It was speculated that association of particular sets of proteins with lipid rafts plays an important role in a variety of signal transduction pathways [93]. While there is evidence for lipid rafts in the exoplasmic leaflet, not much was known for the cytoplasmic leaflet. A link between the lipid rafts in the two

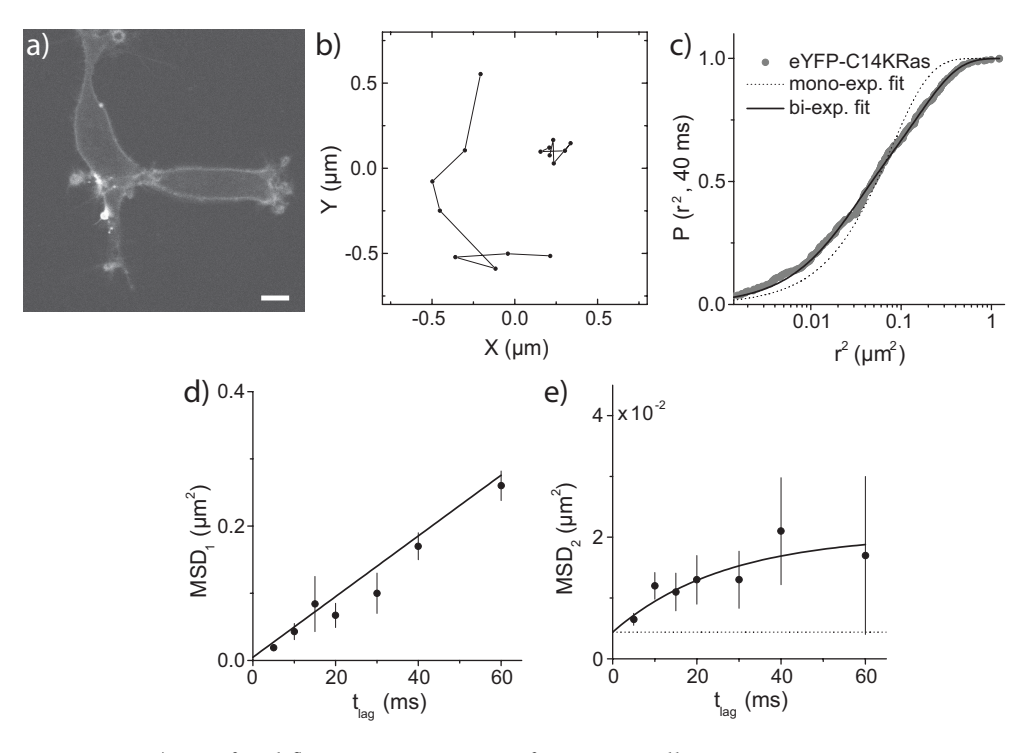


Figure 1.4: **a)** Confocal fluorescence image of 3T3-A14 cells expressing eYFP-C14KRas, 2 days after transfection. Clear plasma membrane localization was observed (scale bar, 10 µm). **b)** Trajectories of eYFP-C14KRas molecules diffusing in the apical membrane of a 3T3-A14 cell. The time between consecutive points was 20 ms. **c)** Cumulative probability, $P(r^2, t_{lag})$, versus square displacements, r^2 with a time lag of 40 ms. Fits to a one-component model (*dashed line*) and a two-component model (*solid line*) clearly showed that the latter model fits better. **d)** The mean squared displacements of the fast fraction plotted versus t_{lag} . The data were fitted according to a free-diffusion model and a diffusion constant $D = 1.00 \pm 0.04 \, \mu \text{m}^2/\text{s}$ was obtained. **e)** The MSDs of the slow fraction plotted versus t_{lag} . A fit according to a confined diffusion model is shown as a solid line. An average domain size of $L = 219 \pm 71$ nm was found. The dotted line represents the offset due to the limited positional accuracy. The same offset was present in (d), although there the dotted line is omitted for clarity.

leaflets is predicted to be of importance in the transduction of cellular signals from the outside to the inside of the cell. In fig. 3a 3T3-A14 cells are shown expressing eYFP-C14KRas [92]. K-Ras is generally used as a non-raft marker and comparison with the raft-marker Lck should give insights into the presence of lipid rafts.

A large number of trajectories (>2500) for eYFP-c14Kras was imaged and used for the analysis. Two of such tracjectories are shown in fig. 1.4b. Note that trajectories are relatively short because of rapid photobleaching of eYFP. From these trajectories square displacement distribution were constructed as described in section 1.2.4. The cumulative probability distribution versus the square displacement for a time lag of 40 ms is shown in fig. 1.4c. A fit of the data to eq. (1.14) clearly shows that the data cannot be described by a onecomponent model. The fit improves significantly when a two-component model is used (eq. (1.15)), while a three-component model did not improve the goodness-of-fit. Fitting the data to eq. (1.15) yielded a fast-diffusing fraction, $\alpha = 0.62 \pm 0.13$, with MSD₁ = $0.16 \pm 0.04 \, \mu \text{m}^2$ and a slow-diffusing fraction with $MSD_2 = 0.021 \pm 0.006 \,\mu\text{m}^2$. This analysis was subsequently performed for all time lags from 5 to 60 ms, and the resulting MSDs were plotted versus time lag. Figures 1.4d, e show the MSD versus time lag for the fast- and slow-diffusing fraction of the eYFP-C14KRas membrane anchor. A fit to eq. (1.8) yielded a diffusion constant $D = 1.00 \pm 0.04 \,\mu\text{m}^2/\text{s}$ for the fast-diffusing fraction (fig. 1.4d). For the slow-diffusing fraction the MSD-plot (fig. 1.4e) indicates that the movement of this fraction is confined. A fit of the data to eq. (1.10) yielded an average domain size of 219 \pm 71 nm. Studying the diffusional behavior of the Lck anchor in a similar manner, showed that the Lck anchor was not significantly slowed down as compared to the K-Ras anchor. This result does not exclude the presence of rafts in the cytoplasmic leaflet, however the size of these rafts was estimated to be smaller than 130 nm, the detection limit achieved in those experiments.

While the previous example focused on the mobility of proteins in the cell membrane, processes inside of the cell were subsequently studied using 3D wide-field microscopy as described in previous subsections. The use of quantum dots (QD) as a fluorescent marker of biomolecules in cells enables

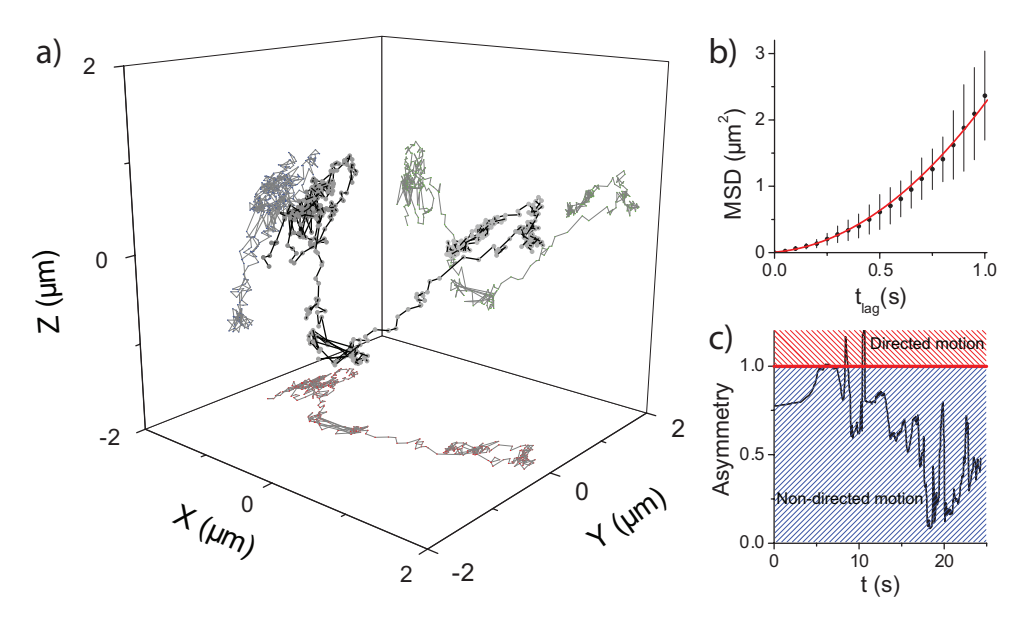


Figure 1.5: **a)** Trajectory of a QD loaded in to HEK293-cells obtained with a frame rate of 20 Hz for a total time of 25 s. Only one plane was imaged for each time point. In two parts of the trajectory directed transport can be clearly seen. **b)** MSD versus time for the first part of the trajectory where directed motion is observed. The supralinear behavior of the MSD confirms that transport takes place. A fit to the data shows that the QD has a velocity of $\nu = 1.4 \pm 0.1 \, \mu \text{m/s}$. **c)** Calculation of the asymmetry parameter clearly shows the two parts of the trajectory where directed motion takes place. (*Asym* > 1)

researchers to follow those molecules for very long time periods, only limited by the lifespan of cells. Figure 1.5 shows results of an experiment where human embryonic kidney cells (HEK293) were incubated with a solution containing 0.1 nM QDs [50]. Within two hours the QDs were internalized, after which the HEK-cells were imaged with a 3D wide-field fluorescence setup using the astigmatism method. Multiple QDs were followed simultaneously in three dimension with high accuracy (30 nm) and at high frame rates (f = 20 Hz) without producing image stacks. In fig. 1.5a one of these trajectories is shown. What was suspected by looking at the trajectory, namely two short periods of directed transport, was confirmed unambiguously. For the first period of directed transport the MSD curve is plotted in fig. 1.5b. The supralinear behavior of the MSD curve confirmed that transport took place. Fitting the 3D-MSD yielded a velocity of $v = 1.41 \pm 0.14 \,\mu\text{m/s}$. Figure 1.5c shows that the asymmetry parameter reliably identified the two periods of directed transport. Calculating the MSD for the initial part of the trajectory confirmed that the QD followed random diffusion during this period ($D = 0.015 \pm 0.001 \,\mu\text{m}^2/\text{s}$).

Figure 1.6 shows that current techniques can also be applied to more complex systems. In this case the wing imaginal disc of a *Drosophila melanogaster* larva is imaged, as was introduced in section 1.1.2. After dissection the disc was placed onto the microscope and the receiving cells were imaged, in this case at a distance of 20 µm from the Dpp source. Dpp is mainly located in endosomes with up to 250 Dpp molecules per endosome. This made it possible to track endosomes for hundreds of frames even though the Dpp is labeled with a variant of the yellow fluorescent protein. The elongated nature of the cells required making stacks consisting of 7 image planes, each separated by 1 μm. The trajectory of one endosome containing Dpp is shown in fig. 1.6a. From the projections onto the 2D planes, the 3D trajectory clearly showed up and the endosome appeared to be confined in lateral direction. Calculating the MSD curve for the xy-projection of the first 190 seconds (fig. 1.6b) clearly showed that the movement of the endosome is confined during this period. Fitting eq. (1.10) yielded an initial diffusion constant $D_0 = 1.60 \pm 0.02 \cdot 10^{-3} \, \mu \text{m}^2/\text{s}$ and a lateral confinement of side length $L = 580 \pm 2$ nm. It should be mentioned that the size of confinement was significantly less than the lateral size of the

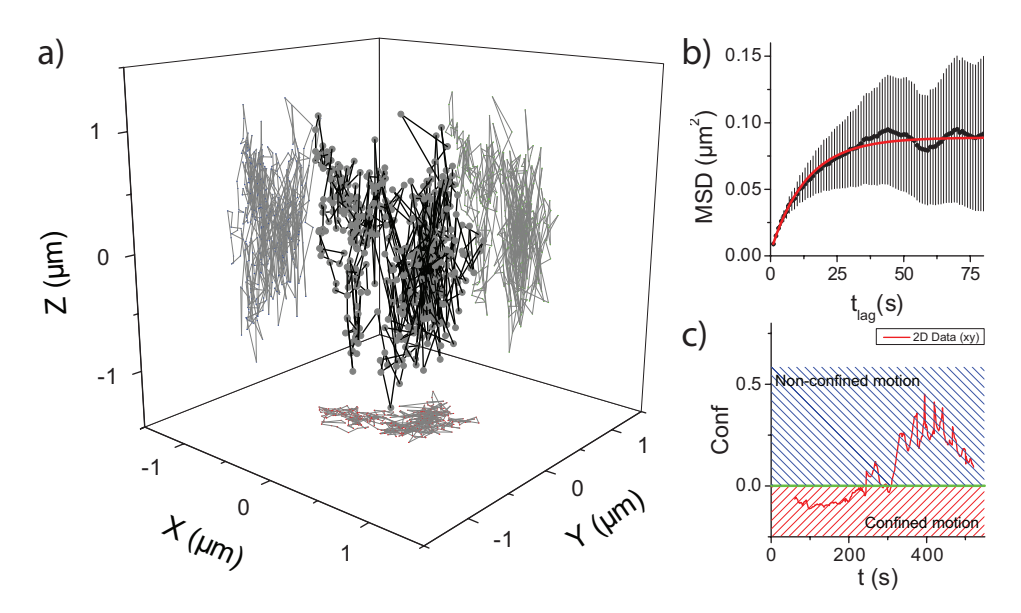


Figure 1.6: **a)** 3D trajectory of an endosome containing Dpp molecules labeled with Venus YFP [4]. The endosome was followed for almost 600 s with a frame rate of 1 Hz. Each image stack consists of 7 image planes. **b)** MSD versus time-plot for the xy-projection of the first 190 seconds of the trajectory. It can be clearly seen that the movement of the endosome is confined during this period. Fitting eq. (1.10) yielded an initial diffusion constant $D_0 = (1.60 \pm 0.02) \cdot 10^{-3} \, \mu \text{m}^2/\text{s}$ and a lateral confinement of side length $L = 508 \pm 2$ nm. **c)** Calculation of the deviation parameter shows that the endosomes shows confined motion in the first part of the trajectory (Conf < 0).

cells of ~ 3 µm. Calculation of the *Conf* parameter (fig. 1.6c) confirmed the observed confinement for this endosome in the first part of the trajectory.

1.2.6 Conclusion

The three examples shown clearly demonstrate that single particle tracking has become an invaluable technique to study processes in life cells and tissue. In the past two-dimensional wide-field fluorescence microscopy has become a widely used technique which has been recently complemented by several methods to provide information about the third dimension with high accuracy. By such extension of an established methodology the range of biological questions which can be addressed is significantly broadened. In combination with superresolution techniques it will prove highly valuable and might help to lift ambiguities in present models of inter- and intra-cellular transport. We do foresee that ultimately single-molecule tracking will permit to follow intricate signalling pathways in space and time even in such complex environments as tissue. The results of such studies will by certain yield unexpected results and, more importantly, will be the solid basis for a quantitative mechanistic understanding of cellular processes in vivo.

1.3 Scope of this thesis

This thesis reports experimental work on the Dpp morphogen gradient formation, especially on the subcellular processes governing intracellular Dpp transport. For this purpose a 3D wide-field fluorescence microscope was developed and used in the experiments. Each chapter was written as a research article addressing different aspects of the experimental method as well as specific parts of intracellular Dpp transport which were studied.

Chapter 2 describes the 3D wide-field fluorescence microscope which was developed to study three-dimensional processes in living tissue. The positional accuracy of this microscope is determined theoretically, with simulations and by experiments involving both immobilized particles and particles which were

internalized by living cells. Data is presented showing that the microscope is a valuable addition to existing techniques and allows for new experiments involving three-dimensional processes in live tissue.

In **chapter 3** the role of the different types of endosomes in intracellulr Dpp transport is investigated. By fluorescently labeling both Dpp and Rab5 (a marker for early endosomes) the average residence time of Dpp in both early and recycling endosomes was determined experimentally. This was done by developing a new method to calculate the cross-correlation between two populations of molecules. The method, called Particle Image Cross-Correlation Spectroscopy (PICCS) has several advantages over existing methods and more reliably calculates cross-correlations between two populations of particles. With PICCS we found that early endosomes contained almost twice as much Dpp on average than other endosomes. Together with a model for intracellular transport we determined rates which are essential for a complete description of the intracellular transport of Dpp.

In **chapter 4** the role of endosome motility and endosomal cargo dynamics in intracellular Dpp transport is studied. By using particle tracking algorithms we found that the motility of endosomes by itself cannot account for intracellular Dpp transport, but that small vesicles traveling between the endosomes are responsible for the majority of intracellular Dpp transport. The average Dpp content of these vesicles was determined by monitoring the concentration of Dpp in individual endosomes. The process that controls the amount of Dpp in vesicles was found to be a passive process. Furthermore we confirmed the existence of an immobile intracellular Dpp fraction.

Bibliography

- [1] Turing, A. Philos T Roy Soc B **237**(641):37–72 (1952).
- [2] Wolpert, L. J Theor Biol 25(1):1–47 (1969).
- [3] Lander, A. D. Cell 128(2):245–56 (2007).
- [4] Kicheva, A., Pantazis, P., Bollenbach, T., Kalaidzidis, Y., Bittig, T., Jülicher, F., and González-Gaitán, M. *Science* **315**(5811):521–5 (2007).
- [5] Strigini, M. and Cohen, S. M. Semin Cell Dev Biol 10(3):335-44 (1999).
- [6] Spencer, F. A., Hoffmann, F. M., and Gelbart, W. M. *Cell* **28**(3):451–61 (1982).
- [7] Nellen, D., Affolter, M., and Basler, K. Cell 78(2):225-237 (1994).
- [8] Letsou, A., Arora, K., Wrana, J. L., Simin, K., Twombly, V., Jamal, J., Staehling-Hampton, K., Hoffmann, F. M., Gelbart, W. M., and Massagué, J. Cell 80(6):899–908 (1995).
- [9] Lecuit, T. and Cohen, S. M. Development 125(24):4901-4907 (1998).
- [10] del Alamo Rodríguez, D., Felix, J. T., and Díaz-Benjumea, F. J. *Developmental Biology* **268**(2):481–92 (2004).
- [11] de Celis, J. F. and Barrio, R. Mech Dev 91(1-2):31-41 (2000).
- [12] Entchev, E., Schwabedissen, A., and González-Gaitán, M. *Cell* **103**(6):981–91 (2000).
- [13] Teleman, A. A. and Cohen, S. M. Cell 103(6):971-80 (2000).
- [14] Entchev, E. V. and González-Gaitán, M. A. *Traffic* **3**(2):98–109 (2002).

- [15] González-Gaitán, M. Mech Dev **120**(11):1265–82 (2003).
- [16] Basler, K. and Struhl, G. Nature 368(6468):208-14 (1994).
- [17] Crick, F. Nature **225**(5231):420–2 (1970).
- [18] Kerszberg, M. and Wolpert, L. J Theor Biol 191(1):103-14 (1998).
- [19] González-Gaitán, M. Nat Rev Mol Cell Biol 4(3):213-24 (2003).
- [20] Kruse, K., Pantazis, P., Bollenbach, T., Jülicher, F., and González-Gaitán, M. *Development* **131**(19):4843–4856 (2004).
- [21] Lander, A., Nie, Q., and Wan, F. Developmental Cell 2(6):785-796 (2002).
- [22] Anderson, C. M., Georgiou, G. N., Morrison, I. E., Stevenson, G. V., and Cherry, R. J. *Journal of Cell Science* **101**(2):415–25 (1992).
- [23] Dahan, M., Lévi, S., Luccardini, C., Rostaing, P., Riveau, B., and Triller, A. *Science* **302**(5644):442–5 (2003).
- [24] Dietrich, C., Yang, B., Fujiwara, T., Kusumi, A., and Jacobson, K. *Biophys J* **82**(1):274–84 (2002).
- [25] Douglass, A. D. and Vale, R. D. Cell 121(6):937-50 (2005).
- [26] Harms, G. S., Cognet, L., Lommerse, P. H., Blab, G. A., Kahr, H., Gamsjäger, R., Spaink, H. P., Soldatov, N. M., Romanin, C., and Schmidt, T. *Biophys J* 81(5):2639–46 (2001).
- [27] Lommerse, P. H. M., Blab, G. A., Cognet, L., Harms, G. S., Snaar-Jagaiska, B. E., Spaink, H. P., and Schmidt, T. *Biophys J* **86**(1):609–616 (2004).
- [28] Schmidt, T., Schütz, G., Baumgartner, W., Gruber, H., and Schindler, H. *Proc.Natl.Acad.Sci.U.S.A.* **93**(7):2926–2929 (1996).
- [29] Kusumi, A., Sako, Y., and Yamamoto, M. *Biophys J* **65**(5):2021–2040 (1993).

- [30] Kubitscheck, U. Single Molecules 3(5-6):267-274 (2002).
- [31] Goulian, M. and Simon, S. *Biophys J* **79**(4):2188–2198 (2000).
- [32] Köhler, R. H., Schwille, P., Webb, W. W., and Hanson, M. R. *Journal of Cell Science* **113**(22):3921–30 (2000).
- [33] Schütz, G., Axmann, M., Freudenthaler, S., Schindler, H., Kandror, K., Roder, J. C., and Jeromin, A. *Microscopy Research and Technique* **63**(3):159–67 (2004).
- [34] Chen, H., Yang, J., Low, P. S., and Cheng, J.-X. *Biophys J* **94**(4):1508–1520 (2008).
- [35] Babcock, H. P., Chen, C., and Zhuang, X. *Biophys J* **87**(4):2749–58 (2004).
- [36] Seisenberger, G., Ried, M. U., Endress, T., Büning, H., Hallek, M., and Bräuchle, C. *Science* **294**(5548):1929–32 (2001).
- [37] Simson, R., Sheets, E. D., and Jacobson, K. *Biophys J* **69**(3):989–93 (1995).
- [38] Feder, T., BrustMascher, I., Slattery, J., Baird, B., and Webb, W. W. *Biophys J* **70**(6):2767–2773 (1996).
- [39] Gelles, J., Schnapp, B. J., and Sheetz, M. Nature 331(6155):450-3 (1988).
- [40] Kural, C., Kim, H., Syed, S., Goshima, G., Gelfand, V., and Selvin, P. R. *Science* **308**(5727):1469–1472 (2005).
- [41] Nan, X., Sims, P. A., Chen, P., and Xie, X. *J.Phys.Chem.B* **109**(51):24220–24224 (2005).
- [42] Courty, S., Luccardini, C., Bellaiche, Y., Cappello, G., and Dahan, M. *Nano Letters* **6**(7):1491–1495 (2006).
- [43] Hecht, E. Optics (1987).

[44] Schmidt, T., Schütz, G., Baumgartner, W., Gruber, H., and Schindler, H. *J.Phys.Chem.* **99**(49):17662–17668 (1995).

- [45] Zhang, B., Zerubia, J., and Olivo-Marin, J.-C. *Applied Optics* **46**(10):1819–1829 (2007).
- [46] Thompson, R., Larson, D., and Webb, W. W. *Biophys J* **82**(5):2775–2783 (2002).
- [47] Cheezum, M., Walker, W., and Guilford, W. *Biophys J* **81**(4):2378–2388 (2001).
- [48] Carter, B. C., Shubeita, G., and Gross, S. P. Phys Biol 2(1):60-72 (2005).
- [49] Falcón-Pérez, J. M., Nazarian, R., Sabatti, C., and Dell'Angelica, E. C. *Journal of Cell Science* **118**(22):5243–55 (2005).
- [50] Holtzer, L., Meckel, T., and Schmidt, T. Applied Physics Letters **90**(5):053902 (2007).
- [51] Bobroff, N. Review of Scientific Instruments **57**(6):1152–1157 (1986).
- [52] Peters, I., de Grooth, B., Schins, J., Figdor, C., and Greve, J. *Review of Scientific Instruments* **69**(7):2762–2766 (1998).
- [53] Gustafsson, M. G., Agard, D. A., and Sedat, J. W. *Journal of Microscopy-Oxford* **195**(1):10–16 (1999).
- [54] McNally, J., Karpova, T., Cooper, J., and Conchello, J.-A. *Methods-A Companion to Methods in Enzymology* **19**(3):373–385 (1999).
- [55] Schütz, G., Axmann, M., and Schindler, H. Single Molecules 2(2):69–73 (2001).
- [56] Speidel, M., Jonás, A., and Florin, E.-L. Opt.Lett. 28(2):69-71 (2003).
- [57] Li, D., Xiong, J., Qu, A., and Xu, T. *Biophys J* 87(3):1991–2001 (2004).

[58] Levi, V., Ruan, Q., and Gratton, E. *Biophys J* **88**(4):2919–2928 (2005).

- [59] Lu, P. J., Sims, P. A., Oki, H., Macarthur, J. B., and Weitz, D. A. *Optics Express* **15**(14):8702–8712 (2007).
- [60] Lessard, G. A., Goodwin, P. M., and Werner, J. H. *Applied Physics Letters* **91**(22):224106 (2007).
- [61] Kao, H. and Verkman, A. *Biophys J* **67**(3):1291–1300 (1994).
- [62] Toprak, E., Balci, H., Blehm, B. H., and Selvin, P. R. *Nano Letters* 7(7):2043–2045 (2007).
- [63] Juette, M. F., Gould, T. J., Lessard, M. D., Mlodzianoski, M. J., Nagpure, B. S., Bennett, B. T., Hess, S. T., and Bewersdorf, J. *Nat.Methods* **5**(6):527–9 (2008).
- [64] Prabhat, P., Ram, S., Ward, E., and Ober, R. J. *IEEE Trans.Nanobioscience* **3**(4):237–242 (2004).
- [65] Prabhat, P., Gan, Z., Chao, J., Ram, S., Vaccaro, C., Gibbons, S., Ober, R. J., and Ward, E. S. *Proc.Natl.Acad.Sci.U.S.A.* **104**(14):5889–5894 (2007).
- [66] Sergé, A., Bertaux, N., Rigneault, H., and Marguet, D. *Nat.Methods* 5(8):687–694 (2008).
- [67] Cognet, L., Harms, G. S., Blab, G. A., Lommerse, P. H. M., and Schmidt, T. Applied Physics Letters 77(24):4052–4054 (2000).
- [68] Ober, R. J., Ram, S., and Ward, E. Biophys J 86(2):1185-1200 (2004).
- [69] Aguet, F., Ville, D. V. D., and Unser, M. *Optics Express* **13**(26):10503–10522 (2005).
- [70] Betzig, E., Patterson, G. H., Sougrat, R., Lindwasser, O. W., Olenych, S., Bonifacino, J. S., Davidson, M. W., Lippincott-Schwartz, J., and Hess, H. F. *Science* **313**(5793):1642–1645 (2006).

30 BIBLIOGRAPHY

[71] Hess, S. T., Girirajan, T. P. K., and Mason, M. D. *Biophys J* **91**(11):4258–4272 (2006).

- [72] Rust, M., Bates, M., and Zhuang, X. Nat. Methods 3(10):793-795 (2006).
- [73] Huang, B., Wang, W., Bates, M., and Zhuang, X. *Science* **319**(5864):810–3 (2008).
- [74] Willig, K. I., Rizzoli, S., Westphal, V., Jahn, R., and Hell, S. W. *Nature* **440**(7086):935–939 (2006).
- [75] Geerts, H., Brabander, M. D., Nuydens, R., Geuens, S., Moeremans, M., Mey, J. D., and Hollenbeck, P. *Biophys J* **52**(5):775–782 (1987).
- [76] Ghosh, R. and Webb, W. W. *Biophys J* **66**(5):1301–1318 (1994).
- [77] Reinfeld, N. Mathematical Programming (1958).
- [78] Veenman, C., Reinders, M., and Backer, E. *Ieee T Pattern Anal* **23**(1):54–72 (2001).
- [79] Bonneau, S., Dahan, M., and Cohen, L. *Ieee T Image Process* **14**(9):1384–1395 (2005).
- [80] Sbalzarini, I. and Koumoutsakos, P. *Journal of Structural Biology* **151**(2):182–195 (2005).
- [81] Genovesio, A., Liedl, T., Emiliani, V., Parak, W., Coppey-Moisan, M., and Olivo-Marin, J.-C. *Ieee T Image Process* **15**(5):1062–1070 (2006).
- [82] Jaqaman, K., Loerke, D., Mettlen, M., Kuwata, H., Grinstein, S., Schmid, S. L., and Danuser, G. *Nat.Methods* **5**(8):695–702 (2008).
- [83] Saxton, M. and Jacobson, K. *Annu.Rev.Biophys.Biomol.Struct.* **26**:373–399 (1997).

BIBLIOGRAPHY 31

[84] Coscoy, S., Huguet, E., and Amblard, F. *Bull Math Biol* **69**(8):2467–92 (2007).

- [85] Meilhac, N., Guyader, L. L., Salome, L., and Destainville, N. *Physical Review e* **73**(1) (2006).
- [86] Qian, H., Sheetz, M., and Elson, E. *Biophys J* **60**(4):910–921 (1991).
- [87] Huet, S., Karatekin, E., Tran, V., Fanget, I., Cribier, S., and Henry, J. *Bio-phys J* **91**(9):3542–3559 (2006).
- [88] Saxton, M. Biophys J 72(4):1744–1753 (1997).
- [89] Schütz, G., Schindler, H., and Schmidt, T. *Biophys J* **73**(2):1073–1080 (1997).
- [90] Deverall, M., Gindl, E., Sinner, E., Besir, H., Ruehe, J., Saxton, M., and Naumann, C. *Biophys J* **88**(3):1875–1886 (2005).
- [91] Semrau, S. and Schmidt, T. *Biophys J* **92**(2):613–21 (2007).
- [92] Lommerse, P. H. M., Vastenhoud, K., Pirinen, N. J., Magee, A. I., Spaink, H. P., and Schmidt, T. *Biophys J* **91**(3):1090–7 (2006).
- [93] Simons, K. and Toomre, D. Nat Rev Mol Cell Biol 1(1):31–9 (2000).

Chapter 2

Nanometric three-dimensional tracking of quantum dots in living cells¹

Wide-field single-molecule fluorescence microscopy has become an established tool for the study of dynamic biological processes which occur in the plane of a cellular membrane. In the current study we have extended this technique to the three-dimensional analysis of molecular mobility. Introduction of a cylindrical lens into the emission path of a microscope produced some astigmatism which was used to obtain the full three-dimensional position information. The localization accuracy of fluorescent objects was calculated theoretically and subsequently confirmed by simulations and by experiments. For further validation individual quantum dots were followed when passively diffusing and actively transported within life cells.

¹This chapter is based on: L. Holtzer, T. Meckel and T. Schmidt, Nanometric three-dimensional tracking of quantum dots in living cells. *Applied Physics Letters* **90** (5), 053902 (2007)

2.1 Introduction

Wide-field single-molecule fluorescence microscopy has become an established experimental technique in the biosciences. So far its strength has mainly been exploited in two-dimensional (2D) systems: for the observation of individual molecules immobilized to substrates, and for the tracking of individual proteins in the cellular membranes [1–4]. The latter is typically carried out at video-rate allowing for simultaneous tracking of several molecules with very high lateral accuracy, far below the diffraction limit [5]. An extension of that technology to a full three-dimensional (3D) single-molecule imaging and tracking platform is highly desirable given that most biological processes take place in the 3D environment of the cell. Several methods to acquire information on the third dimension have been recently developed, i.e. using image stacks [6, 7], off-focus imaging [8] or by orbiting a focused laser beam around a particle [9]. While all these methods have shown to yield valuable information, the main disadvantage is either the imaging speed (only slow molecules can be followed) or the ability to image only one or a few molecules at a time.

Here we describe a simple one-camera 3D wide-field fluorescence setup which can image a large area $(50 \ \mu m)^2$ at high frame rates (~25 Hz). The setup was adapted from a previously described 2D wide-field single-molecule fluorescence setup [10]. By adding a cylindrical lens ($f=10 \ m$) into the detection path of the setup, unambiguous information on the 3D position of individual objects far beyond the diffraction limit was obtained. Our detection scheme follows an earlier development on tracking fluorescing 100 nm beads on a time scale of 0.5 s [11] but with higher sensitivity and higher time resolution. The setup was used to track endocytosed semiconductor quantum dots (QDs), yielding information on active transport of vesicular structures and passive diffusion within them.

2.2 Positional accuracy in three dimensions

The positional accuracy which can be achieved in lateral (x, y) and in axial (z) direction in regular imaging was estimated theoretically from the Cramer-Rao-bound assuming a Gaussian-shaped intensity distribution of a single-molecule image [12]. The Cramer-Rao bound for the position and width of the Gaussian is given by $s_{\mu_x}^2 = s_{\mu_y}^2 = \sigma^2/(8N \ln 2)$ and $s_{\sigma^2}^2 = \sigma^4/N$ in which N is the total number of photons detected by the camera and σ the full-width-half-maximum (FWHM) of the intensity distribution. By the change of the Gaussian width with focal distance the z-position was calculated [6],

$$z = \pm \frac{z_r}{\sigma_0} \sqrt{\sigma^2 - \sigma_0^2} \tag{2.1}$$

in which z_r is the focal depth and σ_0 the diffraction-limited FWHM for a point-source in focus. This dependence holds for $|z| < 2z_r \approx 1000$ nm. Error propagation finally leads to an axial accuracy $s_z^2 = \frac{1}{N} \left(\frac{z_r^2}{2z} + \frac{z}{2} \right)^2$ in which the errors in z_r and σ_0 have been neglected. Both values were determined experimentally with high accuracy in independent experiments. Figure 2.1a,b (solid line) shows both the lateral and the axial accuracies plotted versus the defocus position. Obviously the error in z around the focus is very large and negative and positive defocus cannot be distinguished given the symmetric dependence in z.

Introducing a weak cylindrical lens (f = 10 m) into the emission beam path results in an axial astigmatism, γ , and hence provides an easy way to increase resolution in z [11]. The intensity distribution for a point emitter including astigmatism is described by

$$I(x,y) = N \frac{4 \ln 2}{\pi \sigma_r^2} e^{-4 \ln 2 \left[\frac{(x-\mu_x)^2}{\sigma_r^2/\epsilon^2} + \frac{(y-\mu_y)^2}{\sigma_r^2 \epsilon^2} \right]}$$
(2.2)

in which the ellipticity $\epsilon = \sqrt{\sigma_y/\sigma_x}$ and a generalized width $\sigma_r^2 = \sqrt{\sigma_x^2 \sigma_y^2}$ was introduced. σ_x and σ_y are the FWHM of the intensity distribution in x and y direction, respectively. Note that σ_x is not equal to σ_y except for one position

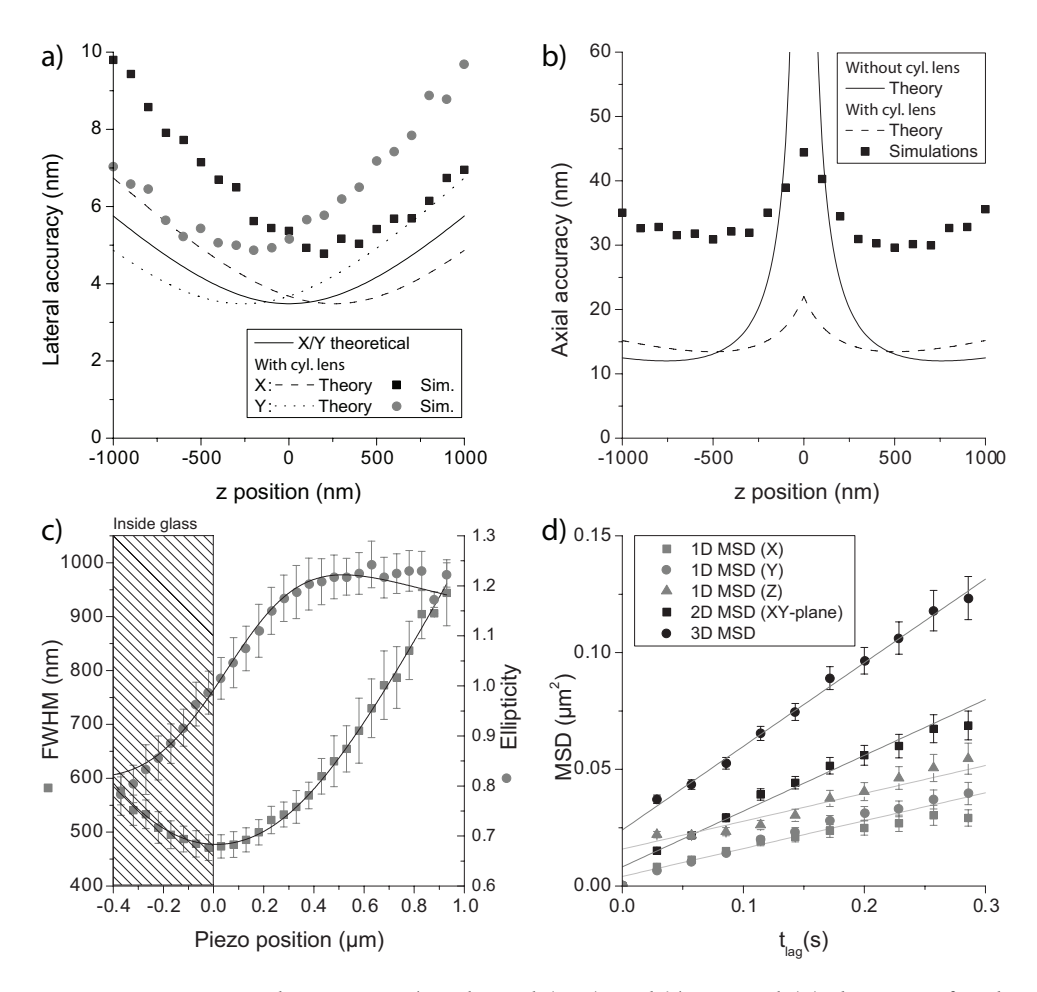


Figure 2.1: Positional accuracy **a**) in lateral (x,y) and **b**) in axial (z) direction for the detection of a fluorescing point object calculated according to the Cramer-Rao bound (lines), and compared to computer simulations (symbols). In the simulation each point object emitted an average of 4000 photons/frame. Each data point is an average of 1000 simulations. **c**) σ_r and ϵ for QDs immobilized onto a glass substrate. 10 images containing 9 QDs on average were taken per point. For z<0 the data deviate from the fit because the focal plane lies inside the coverslip. **d**) MSD-plots of diffusing QDs in a 15% dextran mixture (10 °C, frame rate = 35 Hz).

inbetween the two foci, which we define as z = 0 nm. By substituting z with z + y and z - y in eq. (2.1) to get σ_x and σ_y , and using the definitions for σ_r and ϵ the axial position is given by

$$z(\sigma_r, \epsilon) = \begin{cases} \frac{z_r}{\sigma_0} \sqrt{\frac{\sigma_r^2}{\epsilon^2} - \sigma_0^2} - \gamma & \epsilon < 1\\ -\frac{z_r}{\sigma_0} \sqrt{\sigma_r^2 \epsilon^2 - \sigma_0^2} + \gamma & \epsilon > 1 \end{cases}$$
 (2.3)

Analogous to the earlier treatment the Cramer-Rao bound leads to the accuracy in each direction (see section 2.A.1 for a more detailed derivation):

$$s_{\mu_x}^2 = \frac{1}{N} \frac{\sigma_r^2 / \epsilon^2}{8 \ln 2}$$
 $s_{\mu_y}^2 = \frac{1}{N} \frac{\sigma_r^2 \epsilon^2}{8 \ln 2}$ (2.4a)

$$s_z^2 = \frac{1}{N} \left(\frac{\sqrt{5}z_r^2}{4(z \pm \gamma)} + \frac{\sqrt{5}}{4} (z \pm \gamma) \right)^2 \quad \epsilon \lessgtr 1$$
 (2.4b)

As shown in fig. 2.1a,b the accuracy in z is largely increased compared to the case without cylinder lens while the accuracy in x and y is only slightly reduced.

The theoretical strategy described above was validated by simulations. Intensity profiles for fluorescing molecules were calculated as 2D Gaussians. Camera readout noise (σ_r =23 counts/pixel) and photon-counting statistics of the detector were fully taken into account. Together with pixelation [12] this resulted in a scaling factor between simulations and theory. Additional background noise was neglected. The simulations, in which the signal-to-noise ratio (SNR) was varied from 20 to 1200, confirmed that the positional accuracy scaled with \sqrt{N} [12]. The positional accuracy obtained at a signal of 4000 photons/frame was 6 nm in lateral (x,y) and 30 nm in axial (z) direction (fig. 2.1a,b).

2.3 Validation of the method

For calibration of the setup streptavidin-coated 705 nm QDs were spin coated onto a glass coverslip. QDs were excited for 20 ms at a laser intensity of 0.9

kW/cm² to obtain a SNR of 17 (275 photons/frame). σ_r and ε were measured while scanning the focal plane through the sample (fig. 2.1c). From these data the focal depth $z_r = 474 \pm 4$ nm and the spot size $\sigma_0 = 443 \pm 1$ nm (z = 0 nm) were determined from a fit to the given equations for σ_r and ε . The amount of astigmatism $\gamma = 184$ nm equals that predicted. Compared to the simulations the experimental results have an increased positional accuracy. We attribute this to an overestimation of z_r in the simulations leading to an underestimated increase of the width with defocus in the simulations. Typically 40 nm for the lateral directions (σ_x , σ_y) and 90 nm for the axial direction ($\sigma_z \approx 2.5\sigma_x$) were achieved, confirming that the lateral accuracy is almost unchanged while axial accuracy is largely improved.

Subsequently to the calibration experiments, QDs were dissolved to a final concentration of 0.16 nM in 15% dextran T500. The viscosity of the solution $(\eta \approx 300 \text{ cP at } 10^{\circ}\text{C})$ allowed us to follow the diffusional paths of the QDs for up to several minutes. From image sequences taken at a frequency of 35 Hz the 3D-path was reconstructed. Each trajectory was analyzed in terms of the variation of the mean square displacement (MSD) with time-delay between images. MSD analysis was performed for the full 3D positional information, for the projection of the trajectory onto the image plane (xy), and for the projection onto each of the three spatial directions x, y, and z (fig. 2.1d), respectively. As predicted for free diffusion the MSD increases linearly with time according to MSD = $2nDt + \sum 2\sigma_n^2$, characterized by the diffusion constant D of an *n*-dimensional process. The offset at zero time accounts for the positional accuracy in all three directions, $\sigma_{x,y} = 47$ nm and $\sigma_z = 90$ nm. Fit of the data to this model yielded $D = 0.058 \pm 0.003 \,\mu\text{m}^2/\text{s}$, which is in excellent agreement with the free diffusion of a 22 nm-diameter particle in a solution of viscosity η = 320 cP following the Stokes-Einstein relation.

The methodology as characterized above was subsequently used to study intracellular transport processes. Human embryonic kidney cells (HEK293, see fig. 2.2a) were incubated with a solution containing 0.1 nM QDs. The QDs were internalized within two hours by endocytosis. A corresponding fluorescence image (fig. 2.2b) showed several bright QDs that were easily identified in the low autofluorescence background of the cell. Trajectories for individ-

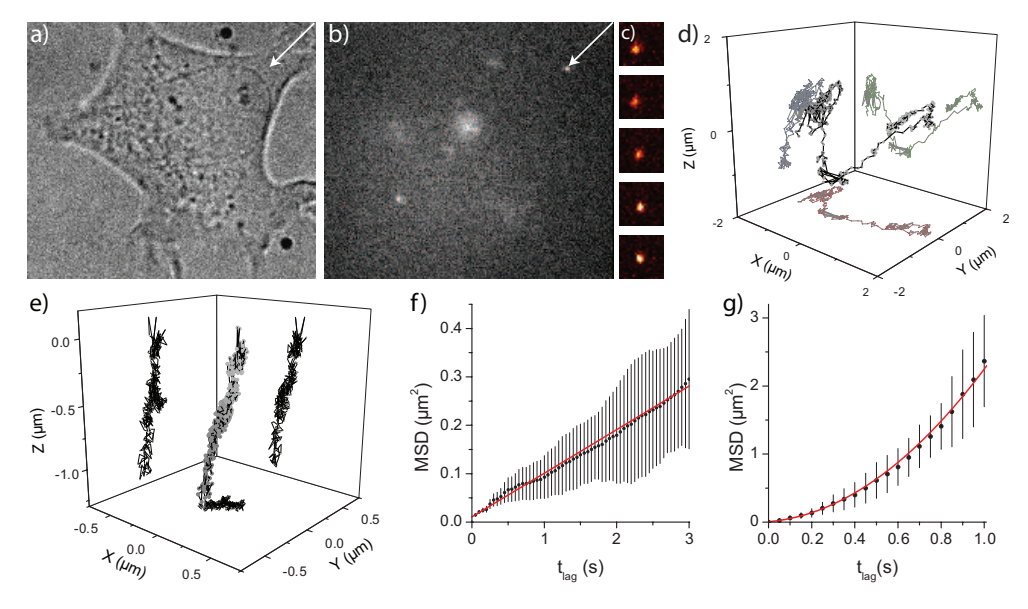


Figure 2.2: HEK293 cell loaded with QDs by endocytosis. **a)** Transmission image of the cell (image: $48x42 \mu m$). **b)** Fluorescence image of the same cell (exposure time = 6 ms, signal = 670 photons/frame). **c)** 5 consecutive images of a QD inside the cell (indicated by the arrow in (a) and (b)) taken at a delay of 50 ms (images: $(4 \mu m)^2$). The change in ellipticity can be clearly seen. **d,e)** 3D-trajectories of different QDs tracked during 500 image frames. **f,g)** 3D-MSD of different parts of the data in (d).

ual QDs were analyzed (fig. 2.2d,e). From the projections onto the 2D planes, the 3D trajectory clearly showed up. The QD in fig. 2.2e shows several types of movement which can be identified by analyzing the MSDs of parts of the trajectory (fig. 2.2f,g). In the first part (fig. 2.2f) the QD was showing random diffusion ($D = 0.015 \pm 0.001 \,\mu\text{m}^2/\text{s}$) in all dimensions. In the next part (fig. 2.2g) the QD shows directed motion, which was confirmed by a detailed analysis of the mobility of the QD motion in all directions. MSD analysis showed a supralinear lag-time dependence along the x- and z-dimension for the QD. Fitting the 3D-MSD [13] yielded a velocity of $v=1.41\pm0.14 \,\mu\text{m/s}$. Analysis of movement perpendicular to the transport did not reveal any confinement, probably because the trajectory was too short (24 frames). However analysis of QDs being transported with lower velocity (example shown in fig. 2.2e) showed that the MSD perpendicular to the transport approached a constant value for $t_{lag} > 3$ s. Analysis showed that the QD in fig. 2.2e was confined [13] to a lateral confinement of side length $L = 161 \pm 3$ nm. The size of the confinement found for this QD is consistent with the size of endocytic vesicles. From this we interpret that QDs were transported inside a vesicle along a cytoskeletal fiber. The velocity mentioned earlier falls within the range of speeds for a vesicle transported by molecular motors inside cells [14].

In order to verify the contribution of active intracellular transport to the observed movements, cells already containing QDs were depleted from ATP by an incubation with 20 mM $\rm NaN_3$ and $\rm 12mM$ 2-Deoxy-D-glucose for 1 hour. After incubation only directed movement (fig. 2.2d,e) was abolished while random diffusion was still observed (data not shown). Hence, the supralinear dependence of MSD with time can clearly be attributed to ATP dependent intracellular processes.

2.4 Conclusion

In conclusion, the introduction of a slight astigmatism into the optical system of a microscope allowed us to extend the positional detection of individual QDs in life-cell imaging to the full 3D-volume. For QDs the positional accu-

racy achieved approached the theoretical limit set by the Cramer-Rao bound and was 43 nm in lateral and 130 nm in axial direction inside cells at a frame rate of 167 Hz. The power of the methodology was demonstrated by detailed analysis of the motion of individual QDs endocytosed by cells. The additional abilities of the 3D-approach was most obviously demonstrated in fig. 2.2. While a conventional 2D-approach would only have shown free diffusion and transport in a plane, the 3D-trajectory shows that the QD was transported along a tubular structure that extended into the third dimension. Hence, a 2D-approach would have resulted in an incomplete interpretation of the observations.

In extrapolation of the results the fast 3D-tracking of individual fluorescent fusion proteins like the green fluorescent protein, however seems exceedingly difficult. Typically in those experiments 150 photons/frame are detected from a single molecule which would lead to an axial accuracy of $\sigma_z = 120$ nm at optimal background conditions. Better results will be achieved for multiple-labeled (5-10x) objects. This will yield longer trajectories and signals of 4000 photons/frame and higher, in particular when additionally the excitation intensity is increased. In this way dynamic localization of e.g. vesicles inside cells at a resolution of 6 nm in lateral and 30 nm in axial direction can be easily obtained. Hence, the application of this fast life-cell imaging methodology to the study of e.g. vesicle trafficking or virus entry [15, 16] will prove highly valuable and might help to lift ambiguities in present models of cellular transport.

2.5 Acknowledgements

We thank W. van der Meer for preparing the HEK293 cell line. This work was supported by funds from the Human Frontiers Science Program grant RGP66/2004, and the Dutch CYTTRON consortium sponsored by the ministry of economic affairs.

2.A Appendix

2.A.1 Derivations

In this appendix we will show how eqs. (2.4a) and (2.4b) were derived.

The Cramer-Rao bound states that the inverse of the Fisher information matrix is the lower limit to the variance of an unbiased estimator for a statistical process. For a statistical process described by

$$f(x,y) = \frac{4\ln 2}{\pi\sigma^2} e^{\frac{-4\ln 2((x-\mu_x)^2 + (y-\mu_y)^2)}{\sigma^2}}$$
(2.5)

the estimators for μ_x and μ_y are the mean values of the distribution in either the x or y-direction and are therefore unbiased. To calculate z the FWHM σ is needed and to calculate the accuracy in σ we use the unbiased estimator for the variance s^2 :

$$E(s^2) = E\left[\frac{\sum (x_i - \overline{x})^2}{n - 1}\right] = \sigma^2$$
 (2.6)

For large samples $n \approx n-1$ and therefore we assume that σ^2 is also an unbiased estimator. The Fisher information matrix is defined as

$$I = -E\left(\frac{\partial U}{\partial \theta}\right) \tag{2.7}$$

in which U is the score function defined as the gradient of the log-likelihood function:

$$U(\theta) = \nabla \ln f(x, y) = \nabla \ln \frac{4 \ln 2}{\pi \sigma^2} - \frac{4 \ln 2((x - \mu_x)^2 + (y - \mu_y)^2)}{\sigma^2}$$
 (2.8)

Taking the derivative of the log-likelihood function with respect to each unbiased parameter of interest yields

$$U_{\mu_x} = \frac{8\ln 2}{\sigma^2} (x - \mu_x) \tag{2.9a}$$

$$U_{\mu_y} = \frac{8\ln 2}{\sigma^2} (y - \mu_y) \tag{2.9b}$$

2.A Appendix 43

$$U_{\sigma^2} = -\frac{1}{\sigma^2} + \frac{4\ln 2((x - \mu_x)^2 + (y - \mu_y)^2)}{\sigma^4}$$
 (2.9c)

The Fisher information matrix is then calculated using eq. (2.7) in which

$$\frac{\partial U}{\partial \theta} = \begin{pmatrix} -\frac{8 \ln 2}{\sigma^2} & 0 & -\frac{8 \ln 2}{\sigma^4} (x - \mu_x) \\ 0 & -\frac{8 \ln 2}{\sigma^2} & -\frac{8 \ln 2}{\sigma^4} (y - \mu_y) \\ -\frac{8 \ln 2}{\sigma^4} (x - \mu_x) & -\frac{8 \ln 2}{\sigma^4} (y - \mu_y) & \frac{1}{\sigma^4} - \frac{8 \ln 2((x - \mu_x)^2 + (y - \mu_y)^2)}{\sigma^6} \end{pmatrix}$$

Since $E(x - \mu_x) = 0$ this results in

$$-E\left(\frac{\partial U}{\partial \theta}\right) = \begin{pmatrix} \frac{8\ln 2}{\sigma^2} & 0 & 0\\ 0 & \frac{8\ln 2}{\sigma^2} & 0\\ 0 & 0 & -\frac{1}{\sigma^4} \end{pmatrix}$$

According to the Cramer-Rao bound the theoretical lower bound for the error (and therefore also the maximum attainable positional accuracy) in the parameters μ_x , μ_y and σ^2 is calculated by taking the square root of the inverse matrix:

$$s_{\mu_x} = \frac{\sigma}{\sqrt{8\ln 2}} \tag{2.10a}$$

$$s_{\mu_y} = \frac{\sigma}{\sqrt{8 \ln 2}} \tag{2.10b}$$

$$s_{\sigma^2} = \sigma^2 \tag{2.10c}$$

Using error propagation s_{FWHM} is calculated:

$$s_{\text{FWHM}} = \frac{\sigma}{2} \tag{2.11}$$

For a process in which N photons are detected eqs. (2.10) and (2.11) should be divided by a factor \sqrt{N} . Previously we showed how to calculate z from eq. (2.1) and hence error propagation is used to estimate the theoretical limit to the accuracy in z:

$$s_z^2 = \left(\frac{\partial z}{\partial \sigma}\right)^2 s_\sigma^2 + \left(\frac{\partial z}{\partial z_r}\right)^2 s_{z_r}^2 + \left(\frac{\partial z}{\partial \sigma_0}\right)^2 s_{\sigma_0}^2$$
 (2.12)

If we assume that z_r and σ_0 can be determined with high accuracy they can be neglected in eq. (2.12) leading to

$$s_z = \sqrt{\left(\frac{z_r^2}{2z} + \frac{z}{2}\right)^2} \tag{2.13}$$

In section 2.2 it was shown that the introduction of a cylindrical lens adds the parameters γ and ϵ to eqs. (2.1) and (2.5) and substitutes σ with σ_r . For our method to work we need a small value for γ (< 300 nm). We have defined γ as half the distance between the original position of an in-focus molecule without cylindrical lens (i.e. the focal length f_o of the microscope objective, since our microscope uses infinity-corrected optics) and the position of an infocus molecule with cylindrical lens in the perturbed axis ($s_{o,\gamma}$):

$$\gamma = s_{\rm clc} = \frac{f_o - s_{o,y}}{2}$$
 (2.14)

in which s_{clc} is the so-called circle of least confusion where the image is circular (z = 0). With paraxial optics the position of the image ($s_{i,y}$) of a molecule at $s_{o,y}$ is approximated:

$$s_{i,y} = \frac{1}{\frac{1}{f_t} + \frac{1}{f_c} - \frac{1}{d - \frac{1}{\frac{1}{f_c} - \frac{1}{s_0,y}}}}$$
(2.15)

with f_t the focal length of the tube lens, f_c the focal length of the cylindrical lens, f_o the focal length of the objective and d the distance between objective and cylindrical lens. Rewriting it for an in-focus molecule:

$$s_{o,y} = -\frac{f_o(25f_tf_cd - 4f_cd - 4f_td + 4f_tf_c)}{-25f_tf_cd + 25f_tf_cf_o + 4f_cd - 4f_cf_o + 4f_td - 4f_tf_o - 4f_tf_c}$$
(2.16)

Combining eqs. (2.14) and (2.16) allows to estimate the focal length of the cylindrical lens needed.

Using the same methodology as in the case without cylindrical lens the maximum achievable positional accuracy in x, y and z is calculated using eqs. (2.2) and (2.3) resulting in eqs. (2.4a) and (2.4b).

2.A Appendix 45

2.A.2 Extension to image stacks

The methodology as outlined in this chapter is mainly focused on experiments in which all the particles are confined to a layer of $1.5-2~\mu m$. When needed, for example in the experiments presented in chapters 3 and 4, the method is easily extended to a larger volume.

Recently several solutions have been proposed to image larger volumes in which for example multiple CCD cameras are used to image different planes simultaneously [17], or in which a beam splitter cube and an extra lens were used to generate a second image on the CCD camera focusing on a different plane [18].

In our experiments however we have used a different method. We placed the objective onto a piezo positioner (Physik Instrumente, Karlsruhe, Germany) which enabled us to move the objective in steps of 0.7-1.0 µm and hence image different focal planes in a consecutive manner, hereby generating image stacks. The advantage of this method over the two other methods is that the volume which can be imaged is in principal only limited by the working distance of the objective. In the other methods the volume is limited by either the number of CCD cameras or the amount of simultaneous images that fit on the CCD chip. A clear disadvantage of our method is the imaging speed. Moving the objective from one position to the next takes around 15-20 ms and therefore imaging of larger volumes (e.g. 7 planes) can take up to 200 ms, which includes the exposure time necessary to image each plane. In our experiments the movement of the objects of interest was low enough (see chapter 4) to assume that the movement of an object in a timespan of 50 ms (needed to image two planes) is smaller than the positional accuracy of our system.

As a result of using image stacks objects will appear in multiple planes in one image stack. In principle the 2D fitting method as presented in this chapter could be used to determine the 3D position of the object relative to each plane in which it appears. A better approach however is to globally fit each image stack. For this purpose the 2D Gaussian profile were extended to 3D volumes, taking into account that the width of the Gaussian varies with axial position z, see eq. (2.3). In the fitting procedure it was taken into account that the total

signal of the Gaussian is constant in each plane. The global fit approach was superior to other approaches in terms of stability and reliability of the results.

Bibliography

- [1] Harms, G. S., Cognet, L., Lommerse, P. H., Blab, G. A., Kahr, H., Gamsjäger, R., Spaink, H. P., Soldatov, N. M., Romanin, C., and Schmidt, T. *Biophys J* **81**(5):2639–46 (2001).
- [2] Vrljic, M., Nishimura, S. Y., Brasselet, S., Moerner, W. E., and McConnell, H. M. *Biophys J* **83**(5):2681–92 (2002).
- [3] Dahan, M., Lévi, S., Luccardini, C., Rostaing, P., Riveau, B., and Triller, A. *Science* **302**(5644):442–5 (2003).
- [4] Tardin, C., Cognet, L., Bats, C., Lounis, B., and Choquet, D. *EMBO J* **22**(18):4656–65 (2003).
- [5] Gelles, J., Schnapp, B. J., and Sheetz, M. Nature 331(6155):450-3 (1988).
- [6] Schütz, G., Pastushenko, V., Gruber, H., Knaus, H., Pragl, B., and Schindler, H. Single Mol 1(1):25–31 (2000).
- [7] van Oijen, A., Kohler, J., Schmidt, J., Muller, M., and Brakenhoff, G. *Chemical Physics Letters* **292**(1-2):183–187 (1998).
- [8] Speidel, M., Jonás, A., and Florin, E.-L. Opt.Lett. 28(2):69-71 (2003).
- [9] Levi, V., Ruan, Q., and Gratton, E. Biophys J 88(4):2919-2928 (2005).
- [10] Schmidt, T., Schütz, G., Baumgartner, W., Gruber, H., and Schindler, H. *Proc.Natl.Acad.Sci.U.S.A.* **93**(7):2926–2929 (1996).
- [11] Kao, H. and Verkman, A. *Biophys J* **67**(3):1291–1300 (1994).
- [12] Ober, R. J., Ram, S., and Ward, E. *Biophys J* **86**(2):1185–1200 (2004).

48 BIBLIOGRAPHY

[13] Saxton, M. and Jacobson, K. *Annu.Rev.Biophys.Biomol.Struct.* **26**:373–399 (1997).

- [14] Nan, X., Sims, P. A., Chen, P., and Xie, X. *J.Phys.Chem.B* **109**(51):24220–24224 (2005).
- [15] Seisenberger, G., Ried, M. U., Endress, T., Büning, H., Hallek, M., and Bräuchle, C. *Science* **294**(5548):1929–32 (2001).
- [16] Babcock, H. P., Chen, C., and Zhuang, X. Biophys J 87(4):2749–58 (2004).
- [17] Prabhat, P., Ram, S., Ward, E., and Ober, R. J. *IEEE Trans.Nanobioscience* **3**(4):237–242 (2004).
- [18] Toprak, E., Balci, H., Blehm, B. H., and Selvin, P. R. *Nano Letters* 7(7):2043–2045 (2007).

Chapter 3

Intracellular Dpp morphogen transport studied with Particle Image Cross Correlation Spectroscopy (PICCS)¹

Morphogens control pattern formation by forming concentration gradients. Gradients are formed by a combination of diffusion and degradation. Recently the effective diffusion and degradation rates of Dpp have been measured. Diffusion and degradation are determined by intracellular trafficking of morphogens: i.e. endocytosis, recycling, and degradation in the lysosomal pathway. However, these trafficking rates have not yet been measured. We followed the transport of the morphogen Decapentaplegic (Dpp) in wing imaginal discs of fruit fly larvae. These experiments required the development of a new analysis method for two-color, single-object data: Particle Image Cross Correlation Spectroscopy (PICCS). With this method we were able to quantify the fraction of Dpp that is correlated with early endosomes. We found that early endosomes contain almost twice as much Dpp as compared to other endosomes. Further we determined the rates underlying Dpp transport among different endosomal compartments. These rates are essential for a complete description of the intracellular transport of Dpp. This novel method is generally applicable to a multitude of biological processes that involve multiple interaction partners and makes use of the superior positional accuracy that is obtained in single-object microscopy.

¹This chapter is based on: L. Holtzer*, S. Semrau*, M. González-Gaitán, T. Schmidt, Intracellular Dpp morphogen transport studied with Particle Image Cross Correlation Spectroscopy (PICCS), *in preparation* (*equal contribution).

3.1 Introduction

The morphogen Decapentaplegic (Dpp) forms a gradient in the developing wing imaginal disc of the fruit fly Drosophila melanogaster, ultimately controlling patterning and growth of the tissue. Dpp originates from a stripe of Dpp-producing cells at the anterior-posterior compartment boundary [1] and is secreted to neighboring cells. A recent study [2] showed that a steady state monoexponential gradient in Dpp is formed. While the latter study successfully and quantitatively describes the gradient on the level of the whole tissue, it provides insufficient insight into the (sub)cellular mechanisms that underlies Dpp transport. Other experiments further suggest that Dpp is spread by three different mechanisms: diffusion in the extracellular matrix [3], receptormediated diffusion [4] and by intracellular transport [5], i.e. multiple endocytosis and subsequent recycling events into the extracellular matrix [6]. The extracellular diffusion and receptor-mediated transport are governing shortrange spreading, while intracellular transport is essential for long-range spreading of Dpp in tissue [7]. In the study described here we further elucidate the subcellular mechanisms of intracellular Dpp transport. Three types of endosomes are involved in Dpp gradient formation by intracellular transport: early, late and recycling endosomes. By using fluorescent endosomal markers and a fluorescent Dpp fusion protein we measured the fraction of Dpp in early endosomes and thereby determined the intracellular trafficking rates of Dpp.

To accomplish this we developed a new analysis technique which quantifies the amount of correlation between two fluorescent species. In the past several techniques have been applied to this problem. In particular single-molecule fluorescence assays have been used successfully to quantify colocalization of interaction partners [8–10]. Single-molecule fluorescence techniques require only small amounts of fluorescent labels and contain information about positional correlations on sub-diffraction length scales [11]. However, the direct mapping between single-molecule signals from two different channels is prone to a systematic error: colocalization is typically defined by a distance threshold below which two signals are considered colocalized. Therefore *a priori* knowledge about the distribution of distances, about the positional error, and about

3.1 Introduction 51

the experimentally unavoidable alignment mismatch between two channels is needed to find a proper threshold. Even without any real correlation this method will always yield a colocalization event due to accidental proximity of signals. This problem aggravates with increasing signal density. Hence, even with the highest spatial resolution, proximity is not the optimal readout for correlation.

Fluorescence Cross-Correlation Spectroscopy (FCCS) and Image Cross-Correlation Spectroscopy (ICCS) directly determine the cross-correlation between the two different color channels [12, 13] without the need for a threshold. However, both have restrictions in accessible time scales, and proper treatment of sometimes heterogeneous background signals is not straightforward.

Here we show how the advantages of ICCS and single-particle tracking can be combined in one analysis technique: Particle Image Cross-Correlation Spectroscopy (PICCS). This technique is largely based on Particle Image Correlation Spectroscopy (PICS) developed by us before [11]. PICCS uses high accuracy single-molecule / single-object position data, but instead of correlating the positions of the same molecular species at several points in time (as is done in PICS), PICCS correlates the positions of two molecular species at the same point in time in two separate channels. Those channels can be two colors, as discussed below, or any other molecular parameter that allows distinction of two species like fluorescence signal level, fluorescence lifetime or polarization. By PICCS a correlation fraction and a correlation length are retrieved on time scales down to 1 ms. Since the input data consists of the positions of individual molecules / particles the autofluorescent background or additional noise sources do not influence the measurement. For the same reason the method is not limited to the diffraction of light and the correlation length can therefore be determined with nanometer accuracy. Finally, PICCS permits for the analysis of subpopulations. As demonstrated below, it is possible, for instance, to determine the correlation fractions for subpopulations which differ in intensity and obtain additional information in this way.

In the following we will present a detailed analysis of intracellular Dpp transport, based on 1) a mathematical description of intracellular Dpp trafficking and 2) the analysis of experimental data with PICCS. This combination

allows us to determine the intracellular trafficking rates of Dpp.

3.2 Intracellular transport of Dpp

Figure 3.1 illustrates intracellular Dpp transport. After endocytosis, a Dpp-containing vesicle fuses with an early endosome. From the early endosome, Dpp is either transferred to a late endosome for degradation, or to a recycling endosome, where it will be exocytosed into the extracellular matrix. While we regularly observed more than one endosome of each type per cell, in the following we treat each type of endosome as a single entity without loss of generality in modeling the intracellular trafficking of Dpp. This simplification is reasonable since we assume that the in- and outflow of Dpp only depends on the Dpp concentration (i.e. it is a first order reaction). This assumption is later confirmed by the data. The wing imaginal disc consists of a 2D-array of cells. Since the gradient is one-dimensional, perpendicular to the line of Dpp-producing cells, we model the disc as a 1D-array of cells. Inflow and outflow of Dpp is described by first order rate equations for each type of endosome. This approach details the theoretical description of Dpp spreading as described before [14], focusing solely on the intracellular trafficking.

Early endosomes receive an inflow of Dpp by endocytosis, depending only on the extracellular Dpp concentration $C_{\rm ex}$ with an inflow rate $k_{\rm ex}$. If the outflow of Dpp from early endosomes occurs with the rate $k_{\rm ea}$, the change in Dpp concentration in the early endosomes of cell n ($C_{\rm ea}^n$) is given by

$$\frac{dC_{\text{ea}}^n}{dt} = \frac{1}{2}k_{\text{ex}}C_{\text{ex}}^n + \frac{1}{2}k_{\text{ex}}C_{\text{ex}}^{n+1} - k_{\text{ea}}C_{\text{ea}}^n$$
(3.1)

assuming that the transport of Dpp is non-directional [5]. Since in fig. 3.1 we have defined $C_{\rm ex}^n$ to be on the left of cell n, the endocytosis term consists of a contribution from both $C_{\rm ex}^n$ and $C_{\rm ex}^{n+1}$, taking into account non-directionality. For the recycling endosome a similar equation is derived, in which a parameter ε is introduced to describe the fraction of Dpp in early endosomes that is

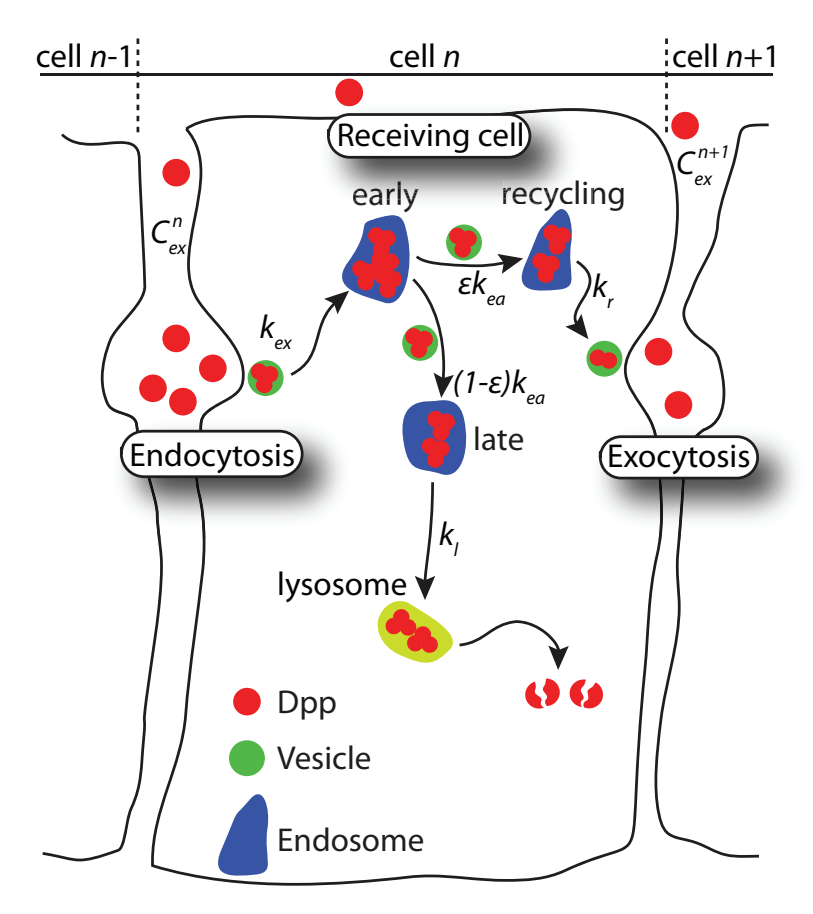


Figure 3.1: Intracellular transport of Dpp. After endocytosis Dpp is transported – via early endosomes – to either late or recycling endosomes. While Dpp in late endosomes is destined to be degraded, Dpp in recycling endosomes is eventually exocytosed into the extracellular matrix.

transferred to recycling endosomes.

$$\frac{\mathrm{d}C_{\mathrm{r}}^{n}}{\mathrm{d}t} = \varepsilon k_{\mathrm{ea}} C_{\mathrm{ea}}^{n} - k_{\mathrm{r}} C_{\mathrm{r}}^{n} \tag{3.2}$$

where C_r is the concentration of Dpp in recycling endosomes and k_r is the rate of Dpp outflow from recycling endosomes. For late endosomes we obtain:

$$\frac{\mathrm{d}C_{\mathrm{l}}^{n}}{\mathrm{d}t} = (1 - \varepsilon)k_{\mathrm{ea}}C_{\mathrm{ea}}^{n} - k_{\mathrm{l}}C_{\mathrm{l}}^{n} \tag{3.3}$$

where C_l is the concentration of Dpp in late endosomes and k_l is the degradation rate. Finally the concentration of Dpp in the extracellular matrix $C_{\rm ex}$ depends only on the recycling rate $k_{\rm r}$ and the endocytosis rate $k_{\rm ex}$, taking into account the non-directionality of intracellular Dpp transport.

$$\frac{dC_{\rm ex}^n}{dt} = \frac{1}{2}k_{\rm r}C_{\rm r}^{n-1} + \frac{1}{2}k_{\rm r}C_{\rm r}^n - k_{\rm ex}C_{\rm ex}^n \tag{3.4}$$

Solving eqs. (3.1) to (3.4) in a steady state [5, 15] gives the average Dpp concentration in each type of endosome in each cell. From the solution we derive the fraction f of endosomal Dpp that is contained in early endosomes:

$$f = \frac{C_{\text{ea}}}{C_{\text{tot,endo}}} = \frac{1}{1 + \frac{\varepsilon k_{\text{ea}}}{k_{\text{r}}} + (1 - \varepsilon) \frac{k_{\text{ea}}}{k_{\text{l}}}}$$
(3.5)

From the known decay length of the Dpp-gradient ($\lambda = 7.7 \pm 2.1$ cells) $\varepsilon = 0.996 \pm 0.002$, is derived [2]. A more detailed theoretical derivation of eq. (3.5) and the determination of ε is found in section 3.A.1. For the recycling endosome outflow rate $k_{\rm r}$ we further derive:

$$k_{\rm r} = \frac{\varepsilon f k_{\rm ea} k_{\rm l}}{(1 - f) k_{\rm l} - f (1 - \varepsilon) k_{\rm ea}}$$
(3.6)

In previous experiments the degradation rate k_d for Dpp has been determined [2]. Before a Dpp molecule is being degraded in a lysosome [5] it has been

endocytosed, transported to an early endosome and consecutively to a late endosome, after which it final goes to the lysosome. Hence the degradation rate k_d can be expressed in terms of the other rates:

$$\frac{1}{k_{\rm d}} = \frac{1}{k_{\rm ex}} + \frac{1}{(1 - \varepsilon)k_{\rm ea}} + \frac{1}{k_{\rm l}}$$
 (3.7)

Combining eqs. (3.6) and (3.7) gives for k_r :

$$k_r = \frac{\varepsilon f k_{\text{ea}} k_{\text{ex}} k_{\text{d}}}{k_{\text{ex}} k_{\text{d}} - f k_{\text{ea}} (1 - \varepsilon) (k_{\text{ex}} - k_{\text{d}})}$$
(3.8)

which also gives an upper limit to the outflow rate for the early endosome k_{ea} :

$$k_{\rm ea} < \frac{k_{\rm ex}k_{\rm d}}{f(1-\varepsilon)\left(k_{\rm ex}-k_{\rm d}\right)} \tag{3.9}$$

3.3 Particle image cross-correlation spectroscopy

Particle image cross-correlation spectroscopy (PICCS) is a method to quantitatively determine the correlation between arbitrary, fluorescently labeled molecules. Here we present the basic idea behind the PICCS methodology and algorithm. The theoretical background is detailed in section 3.A.2 and the scaling of the errors of the method is discussed in section 3.A.4. We assume that two interaction partners are labeled with two spectrally distinguishable fluorophores. The interaction partners can be single molecules or extended objects. We further assume that their density is so low that they can be resolved individually and their position determined with a high positional accuracy [16–18]. For simplicity we will denote the signals coming from the two fluorophores by 'YFP' and 'CFP' without loss of generality. The task is to determine the correlation fraction of the interaction partners, i.e. to determine the fraction of CFP that colocalizes with YFP (or vice-versa). In what follow we will calculate the fraction of YFP signals which are correlated to a CFP signal.

The first step in the PICCS analysis is identical to existing single-molecule tracking methods [9, 10]: the position of YFP and CFP signals is determined

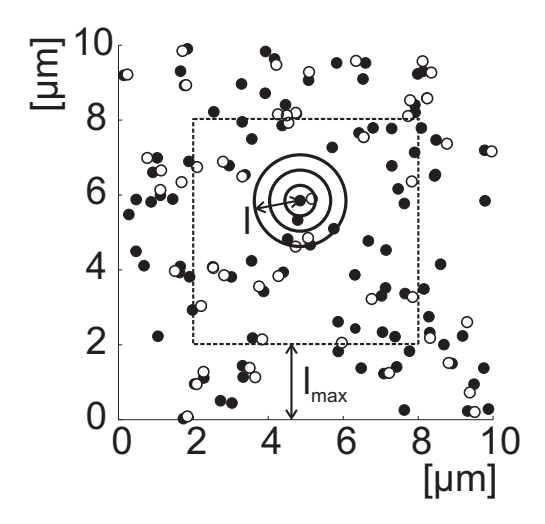


Figure 3.2: PICCS algorithm. For all YFP signals (solid circles) the number of CFP signals (open circles) are counted which fall into a circle of radius l from a YFP signal. The total number is subsequently divided by the number of YFP signals. By increasing l from 0 to $l_{\rm max}$ the correlation function $C_{\rm cum}(l)$ is constructed. The dashed line encloses the area in which the YFP signals are used for analysis. This area is separated from the edges of the image by $l_{\rm max}$ ($l_{\rm max}=2~\mu{\rm m}$ is taken). The signal positions were simulated with the following parameters: density of YFP signals $c_{\rm YFP}=1~\mu{\rm m}^{-2}$, correlation fraction $\alpha=0.5$ (results in a density of CFP signals of $c_{\rm CFP}=0.5~\mu{\rm m}^{-2}$), correlation length $\sigma=150~{\rm nm}$.

with sub-diffraction positional accuracy by fitting two-dimensional Gaussians to the fluorescence signals. Subsequently a cross correlation function $C_{\text{cum}}(l)$ between the two channels is calculated with an ensemble approach. $C_{\text{cum}}(l)$ is equal to the average number of CFP signals at time $t + \Delta t$ which have a distance smaller than l to a certain YFP signal at time t (fig. 3.2). When both fluorophores are imaged at the same time $\Delta t = 0$ s.

To avoid edge effects, only those YFP signals are used which lie farther away from the edges of the image than a predefined maximal distance $l_{\rm max}$ (0 < l < $l_{\rm max}$, dashed line in fig. 3.2).

As detailed in [11] and Sec. 3.A.2, this procedure results in a correlation function of the form

$$C_{\text{cum}}(l) = \alpha P_{\text{cum}}(l) + c_{\text{CFP}} \cdot \pi l^2$$
(3.10)

if the uncorrelated CFP signals are distributed randomly with a uniform density c_{CFP} . $P_{\text{cum}}(l)$ is the cumulative probability to find a distance smaller than l between a YFP and a CFP signal which are correlated. α is the correlation fraction, i.e. the fraction of YFP signals which are correlated to a CFP signal. $\alpha=1$ if there is a corresponding CFP signal for any YFP signal and $\alpha=0$ if CFP and YFP signals are completely uncorrelated. In the form presented so far, the algorithm requires a random, homogeneous distribution of CFP signals, which results in the term $c_{\text{CFP}} \cdot \pi l^2$ in eq. (3.10). To correct for a non-random distribution of CFP signals we can calculate the spatial correlation among CFP signals by regular Particle Image Correlation Spectroscopy (PICS), see [11] and section 3.A.2.

Figure 3.3 shows an example for an experimentally determined correlation function. A wing imaginal disc of a fruit fly larva expressing Dpp-YFP and Rab5-CFP was imaged. Rab5 is a marker for early endosomes [19]. In total 28 z-stacks in both channels were taken. The endosome positions for each image in a z-stack were projected into one plane resulting in 28 YFP-CFP image pairs. Figure 3.3a,b show the first image stack for the YFP and CFP channel. The correlation function is shown in fig. 3.3c and the cumulative probability function $P_{\text{cum}}(l)$ (eq. (3.12)) is shown in fig. 3.3d.

The density of CFP signals c_{CFP} and the correlation fraction α were determined by fitting a straight line to the linear part of C_{cum} (l) plotted against l^2 (fig. 3.3c). The slope of this line gives $\pi \cdot c_{\text{CFP}}$ while the offset is equal to α . After subtraction of the linear contribution and division by α , P_{cum} (l) remains.

If correlated signals were perfectly colocalized (both fluorescent molecules are at the same position in space), $P_{\text{cum}}(l)$ would be given by

$$P_{\text{cum}}(l) = 1 - \exp\left(-\frac{l^2}{2\sigma^2}\right) \tag{3.11}$$

with the correlation length σ . In any real experiment however, the positions of

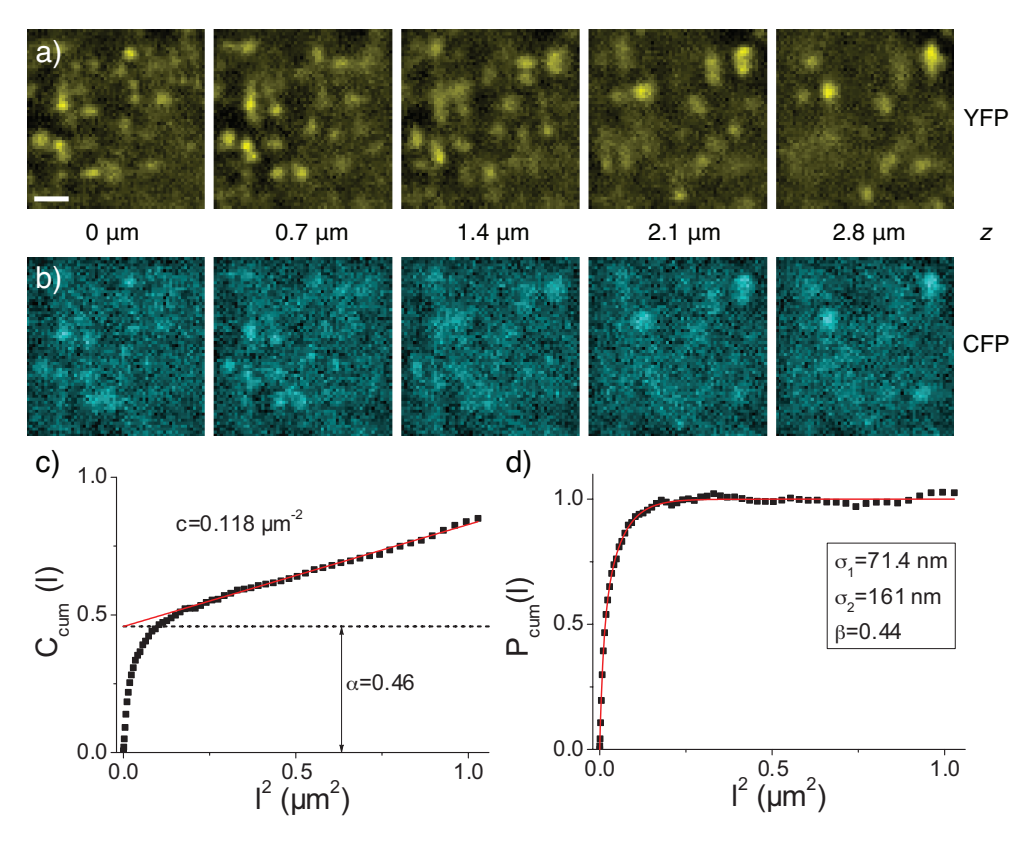


Figure 3.3: Correlation fraction, signal density and correlation length from experimental data. A wing imaginal disc was imaged for 300 s using an alternating excitation method (described in section 3.4). Each image stack consists of 5 image planes $(10 \times 10 \mu \text{m})$ separated by 0.7 μ m in axial direction. Low frequency background was eliminated by applying a high-pass filter. **a)** Raw image stack from the Dpp-YFP channel (scale bar = 2 μ m). **b)** Raw image stack from the Rab5-CFP channel. **c)** Correlation function $C_{\text{cum}}(l)$ obtained by PICCS. Fitting to the linear part yielded a Dpp-YFP density of $c=0.12\pm0.02$ endosomes μ m⁻² (solid line) and a correlation fraction of $\alpha_{\text{e,Dpp}}=0.46\pm0.04$ (offset of the fitted line). **d)** $P_{\text{cum}}(l)$ which resulted from subtraction of the linear contribution from $C_{\text{cum}}(l)$ and division by $\alpha_{\text{e,Dpp}}$. The correlation lengths σ_1 , σ_2 and the fraction β were determined by fitting eq. (3.12) which gave $\sigma_1=71\pm17$ nm, $\sigma_2=161\pm34$ nm and $\beta=0.44\pm0.17$, respectively. All errors were determined from simulations, see section 3.A.4.

particles cannot be exactly determined. This introduces an (apparent) correlation length, given by the finite positional accuracy $\sigma = \sqrt{2}\delta$, where δ is the one-dimensional positional accuracy for a fluorescent signal, see section 3.A.2. Any real correlation originating from the interaction between the studied objects adds to the correlation length given above.

In the experiments presented here, the signal intensity varies between signals and since the positional accuracy depends on the signal intensity, there is no well-defined overall positional accuracy. Therefore a modified version of eq. (3.11) including two effective correlation lengths (σ_1 and σ_2) is needed to describe the observed data.

$$P_{\text{cum}}(l) = \beta \left(1 - \exp\left(-\frac{l^2}{2\sigma_1^2}\right) \right) + (1 - \beta) \left(1 - \exp\left(-\frac{l^2}{2\sigma_2^2}\right) \right)$$

$$(3.12)$$

where β is the fraction of data that has a correlation length σ_1 . Adding more effective correlation lengths does not significantly improve the fit.

The method developed so far disregards signal intensities. We can therefore only determine the fractional amount of Dpp-containing early endosomes and not the fraction of Dpp molecules contained in early endosomes. Since there is no reason to assume that Dpp is homogenously distributed among the different types of endosomes, it is essential to include the intensity (which is a direct measure for the amount of Dpp molecules in an endosome) into the PICCS algorithm. We did this by weighting the occurrence of a YFP signal (Dpp-containing endosome) by its intensity. The average intensity of the correlated fraction was subsequently calculated by the offset of the correlation function and dividing the obtained value by that from the original unmodified correlation data (fig. 3.4).

3.4 Materials and Methods

The *UAS-YFP-Dpp* line was generated by using the existing *UAS-GFP-Dpp* vector [5] where GFP was replaced by YFP (Venus) [20]. dpp^{d8}/dpp^{d12} ; dpp-Gal4/UAS-YFP-Dpp flies have an identical wing phenotype to the dpp^{d8}/dpp^{d12} ; dpp-Gal4/UAS-GFP-Dpp flies [5]: they survive to adulthood and have normally patterned wings, although smaller in size (data not shown). For determination of early, recycling and late endosome distributions in wing imaginal discs we used the following genotypes: tub-CFP-Rab5, tub-YFP-Rab7 and tub-YFP-Rab11 [21].

To obtain wing imaginal discs, third instar larvae (*tubulin-CFP-Rab*; *dpp-Gal4/UAS-YFP-Dpp*) were dissected in Clone8 medium (Shields & Sang M3 Medium containing 2% Fetal Calf Serum, 2.5 % Fly Extract, 12.5 IU Insulin/100 ml medium and 1X Penicillin/Streptomycin), after which the wing imaginal discs were mounted in a custom-made sample holder. Nail polish was used for sealing of the sample holder. The wing imaginal discs were imaged approximately 10 min after dissection. Samples were discarded 1 hour after dissection.

Imaging was done on a 3D wide-field fluorescence microscope as described previously [22]. To image a z-range of $\sim 4 \mu m$, image stacks were generated using a piezo-driven objective holder (Physik Instrumente, Karlsruhe, Germany) to move the objective in axial direction. Each image stack contained 5 image planes with $\Delta z = 0.7 \, \mu \text{m}$ between each image plane. The time between image planes was 40 ms, during which the movement of the endosomes was negligable. Therefore each image stack was assumed to be acquired at one time point. Wing imaginal disc samples were excited by an Argon-ion laser (Coherent, Santa Clara CA, USA) at either 458 nm to excite Rab5-CFP or 514 nm to excite Dpp-YFP. An alternating excitation pattern was used to distinguish between the two fluorophores. The pattern consisted of 1 image stack which was excited at 458 nm and consecutively 10 image stacks were excited at 514 nm with a stack rate of 1 Hz. The fast switching between laser lines was done using an Acousto-Optic Tunable Filter (AA Opto-Electronic, Orsay, France). This pattern was chosen to minimize photobleaching of the CFP, since the amount of Rab5-CFP per endosome was lower than the amount of Dpp-YFP. Imaging

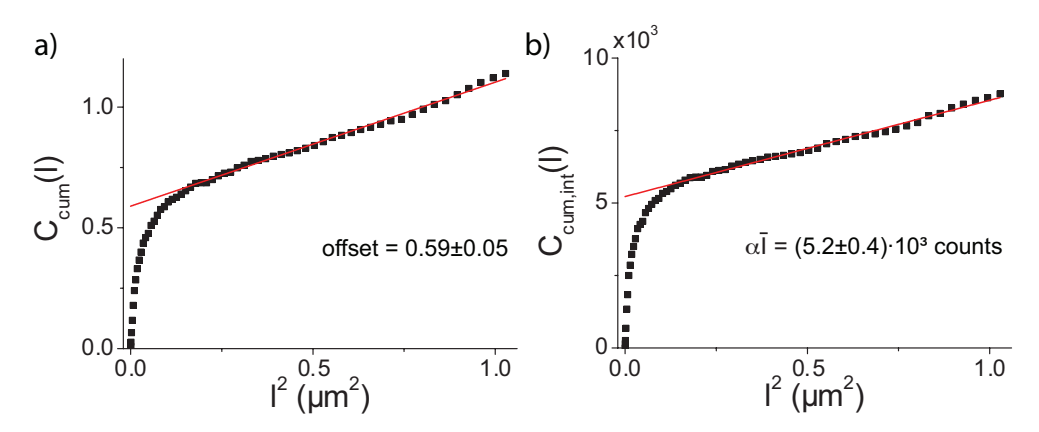


Figure 3.4: a) Correlation function for the correlation between Rab5-CFP and Dpp-YFP. Fitting a line to the linear part resulted in an offset at $l^2 = 0$ of $59 \pm 5\%$. Correction of the data using spatial correlations gives $\alpha_{\rm Dpp,e} = 66 \pm 5\%$. b) Correlation function for the same data after weighting of the Dpp-YFP endosomes with their respective intensities. Fitting the linear part resulted in $\alpha_{\rm Dpp,e}\bar{I} = (5.2 \pm 0.4) \cdot 10^3$ counts, which gives an average Dpp-YFP signal of $\bar{I} = (8.9 \pm 1.0) \cdot 10^3$ counts for early endosomes that contain Dpp-YFP.

was done in the apical region of the cells since most of the endosomes are located there [2]. Dpp-producing cells (the source) were located by eye using a Mercury lamp (Zeiss, Oberkochen, Germany) for excitation. Using a motorized stage the center of the image was typically 20 μ m displaced from the source, with an image area of 100 μ m² showing approximately 17 cells in each experiment.

3.5 Results and discussion

In fig. 3.3 we showed for one wing imaginal disc that the correlated fraction of early Rab5-CFP labeled endosomes in the pool of all endosomes that contain Dpp-YFP in a wing imaginal disc is $\alpha_{e,Dpp} = 46 \pm 4\%$. Correction for a non-random distribution of CFP signals, see section 3.A.2, did not change

this result. Conversely the correlated fraction of Dpp-YFP containing endosomes in the pool of all Rab5-CFP labeled early endosomes was 59 \pm 5% (see fig. 3.4a). After correction for the non-random distribution of CFP signals (see section 3.A.2) the latter value was finally increased to $\alpha_{\rm Dpp,e}$ = 66 \pm 5%. Hence, two-thirds of the early endosomes contained Dpp, and about half of the Dpp-YFP containing endosomes were early endosomes.

To determine further whether Dpp molecules were homogeneously distributed over the different types of endosomes we used the 'weighted' PICCS method. Figure 3.4b shows the cross-correlation between Rab5-CFP labeled early endosomes and Dpp-YFP-containing endosomes weighted by the Dpp-YFP intensity. Fitting a straight line to the linear part gave a coefficient of $\alpha_{\text{Dpp,e}}\bar{I} = (5.2 \pm 0.4) \cdot 10^3$ counts. From the latter and our earlier result on $\alpha_{\text{Dpp,e}}$ (fig. 3.4a) we obtained the average intensity of Dpp in early endosomes to be $I = (8.9 \pm 1.0) \cdot 10^3$ counts per endosome. The latter value, together with the knowledge of the total number of measured intensities of Dpp-YFP containing endosomes in the wing disc (N = 735 endosomes in 28 image stacks, data not shown) and the total fluorescence signal of Dpp-YFP in the wing disc $(I_{\text{tot}} = (4.9 \pm 0.8) \cdot 10^6 \text{ counts in all image stacks, data not shown), the frac$ tion of all Dpp-YFP molecules that was contained in early endosomes was $f = \frac{\alpha_{\text{Dpp,e}} N \bar{I}}{I_{\text{tot}}} = 60 \pm 2\%$. Hence, we found that early endosomes contained on average $n_{\text{Dpp,e}} = 1.8$ times as much Dpp-YFP as compared to late and/or recycling endosomes.

Segmentation with respect to the Dpp concentration in each endosome, as determined by the detected fluorescence signal, confirmed the latter finding. Analysis performed on the more intense half of the Dpp-YFP containing endosomes resulted in $\alpha_{e,Dpp}=55\pm7\%$, and $\alpha_{e,Dpp}=35\pm6\%$ for the less intense half of the endosomes (fig. 3.5a). Together our results showed that Dpp was not homogenously distributed among the different types of endosomes. All results were independent on spatial data segmentation with respect to the cell's distance to the Dpp-source.

As reported previously [23] the amount of Rab5 associated to endosomes fluctuates on the time scales of our experiments. To study the effect of Rab5

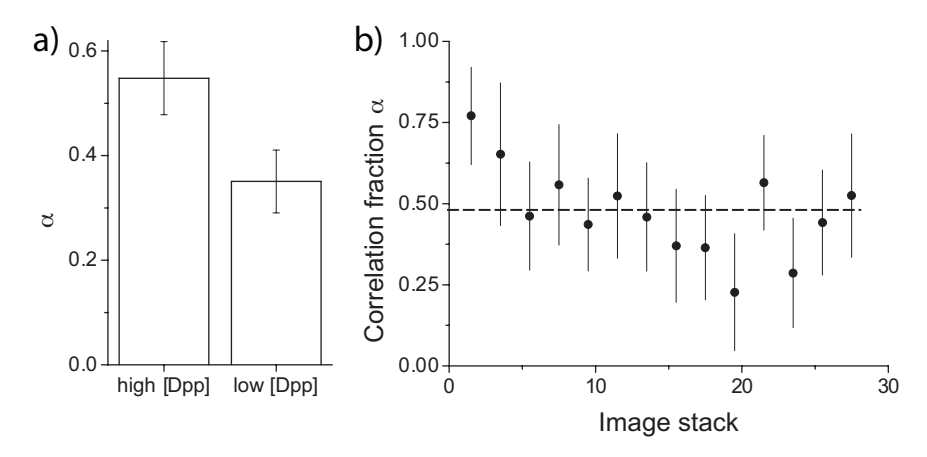


Figure 3.5: Correlation fraction calculation α of early endosomes for segmented data sets. **a)** Correlation fraction for Dpp-YFP-containing endosomes segmented according to Dpp concentration. For each image stack the Dpp-containing endosomes were divided in two halfs, high intensity and low intensity. Applying PICCS on each subset shows that $\alpha_{\rm e,Dpp}=55\pm7\%$ of the high-intensity Dpp-containing endosomes were early endosomes, in comparison to $\alpha_{\rm e,Dpp}=35\pm6\%$ of the low-intensity Dpp-containing endosomes. **b)** $\alpha_{\rm e,Dpp}$ calculated at different time points, using only 2 YFP-CFP image stacks for each data point. $\alpha_{\rm e,Dpp}$ fluctuates around $47\pm14\%$, indicated by the dashed line. The large error bars are caused by the low amount of data in each point (i.e. only 2 CFP-YFP image stack pairs).

fluctuation on our measurements we analyzed the changes in correlation fraction over time. Instead of using the whole data set (28 YFP-CFP image stack pairs), we calculated the correlation fraction for data subsets containing 2 adjacent YFP-CFP image stacks (i.e. stack 1-2, stack 3-4, stack 5-6, etc.). In fig. 3.5b $\alpha_{e,Dpp}$ is plotted versus the time. $\alpha_{e,Dpp}$ fluctuates around 47% with $\sigma=14\%$, however no systematic trend on longer timescales was observed as has been reported for Rab5 fluctuations in early endosomes [23].

The results presented so far were obtained from one wing imaginal disc (17 cells in the field of view). We repeated the described experiments for two other wing imaginal discs (total number of cells=51, image centered at 20 μ m

from the source), and found that $\alpha_{\rm e,Dpp} = 38 \pm 2\%$ of Dpp-containing endosomes were early endosomes, and that early endosomes contain $f = 52 \pm 1\%$ of the endosomal Dpp with on average $n_{\rm Dpp,e} = 1.9$ times as much Dpp in early endosomes compared to late and recycling endosomes.

All experiments were done in the apical 4.5 μ m region of the cells. In order to draw conclusions about the kinetic parameters of intracellular Dpp traficking, the complete apicobasal distribution of the different types of endosomes has to be considered. Both early and recycling endosomes are known to be located mainly in the apical region of epithelial cells [24, 25]. We confirmed this distribution for wing imaginal discs by measuring the apicobasal distribution of early, recycling and late endosomes over an axial range of 20 μ m with Rab5-CFP, Rab11-YFP or Rab7-YFP, respectively. We found that 65% of the early endosomes, 41% of the recycling endosomes, and 62% of late endosomes are located in the most apical 4.5 μ m of the disc, i.e. 51% of non-early endosomes were in the volume measured in our experiments, compared to 65% of the early endosomes. We corrected our results for this difference by calculating the real Dpp fraction f using

$$f = \frac{\alpha_{\text{e,Dpp}} n_{\text{Dpp,e}} M_{\text{non-early}}}{\alpha_{\text{e,Dpp}} n_{\text{Dpp,e}} M_{\text{non-early}} + (1 - \alpha_{\text{e,Dpp}}) M_{\text{early}}}$$
(3.13)

in which $M_{\rm early}$ and $M_{\rm non-early}$ are the fractions of the total pool of early and non-early endosomes, respectively, which were in the measured volume. Taking into account that early endosomes contained 1.9 times as much Dpp as other endosomes we found a Dpp fraction of $f=48\pm5\%$ contained in early endosomes.

From previous FRAP experiments the Dpp degradation rate was determined [2] to be $k_d = (2.52 \pm 1.29) \cdot 10^{-4} \text{ s}^{-1}$ [2]. The contribution of k_{ex} was estimated from the Dpp production rate, which was found to be 2.69 ± 1.58 molecules per cell per second [2]. Since the system is in a steady state, the produced Dpp needs to be endocytosed at the same rate as it is produced and we set $k_{\text{ex}} = 2.69 \pm 1.58 \text{ s}^{-1}$. This value is much faster than the typical endocytosis time, which typically is on the order of tens of seconds to a few minutes [26, 27]. The value reported here however is the average rate per Dpp molecule

if they would be endocytosed one by one. It therefore does not say anything about the amount of Dpp molecules that are endocytosed at the same time.

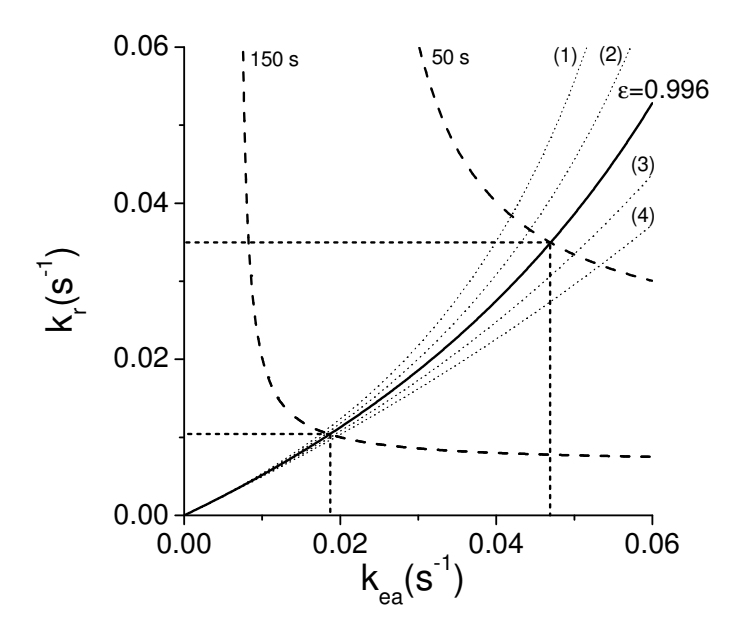


Figure 3.6: Possible values for the recycling endosome outflow rate k_r for different values of the early endosome outflow rate $k_{\rm ea}$, using f=0.48 and $\varepsilon=0.996$ (solid line). The dotted lines show $k_{\rm r}$ and $k_{\rm ea}$ for values of $\varepsilon=0.994$ (1), $\varepsilon=0.995$ (2), $\varepsilon=0.997$ (3) and $\varepsilon=0.998$ (4). The dashed lines indicate the allowed values for $k_{\rm r}$ and $k_{\rm ea}$ if transport across a single cell takes 150 s as lower limit and 50 s as upper limit as estimated and measured before [2, 6, 28, 29]. The intersection of the solid and the dashed lines indicate range of solutions for the values of $1.0 \cdot 10^{-2} < k_{\rm r} < 3.5 \cdot 10^{-2} \, {\rm s}^{-1}$ and $1.9 \cdot 10^{-2} < k_{\rm ea} < 4.7 \cdot 10^{-2} \, {\rm s}^{-1}$.

Using eq. (3.9) we further determined an upper limit value for the early endosomes outflow rate to be $k_{\text{ea,max}} = 0.13 \text{ s}^{-1}$, which translates to a minimum Dpp residence time in early endosomes of $t_r = \frac{1}{k_{\text{ea}}} > 7.6 \text{ s}$. Values for the early endosome outflow rate k_{ea} and the recycling endosome outflow rate k_{r}

are further limited by eq. (3.6). By realizing that both rates must be ultimately limited by the total rate estimated for Dpp transport across a single cell [6, 28, 29] which was 1/(50 s) and 1/(150 s), repectively, we find the constraint

$$50 < \frac{1}{k_{\rm ex}} + \frac{1}{\varepsilon k_{\rm ea}} + \frac{1}{k_{\rm r}} < 150$$
 (3.14)

as indicated as dashed lines in fig. 3.6. We already determined that $k_{\rm ex}$ is much faster compared to $k_{\rm ea}$ and $k_{\rm r}$. Hence, the contribution of $k_{\rm ex}$ in eq. (3.14) is negligable. From the graph in fig. 3.6 we find that $1.9 \cdot 10^{-2} < k_{\rm ea} < 4.7 \cdot 10^{-2} \, {\rm s}^{-1}$ and $1.0 \cdot 10^{-2} < k_{\rm r} < 3.5 \cdot 10^{-2} \, {\rm s}^{-1}$. For the average residence times $t_{\rm r}$ of Dpp in the early and recycling endosomes we found $21 < t_{\rm r,ea} < 53 \, {\rm s}$ and $29 < t_{\rm r,r} < 100 \, {\rm s}$, respectively. Uncertainty in ε , estimated to be 0.002, did not significantly influence this result (see dotted lines in fig. 3.6 for ε =0.994 (1), 0.995 (2), 0.997 (3), and 0.998 (4)).

3.6 Conclusion

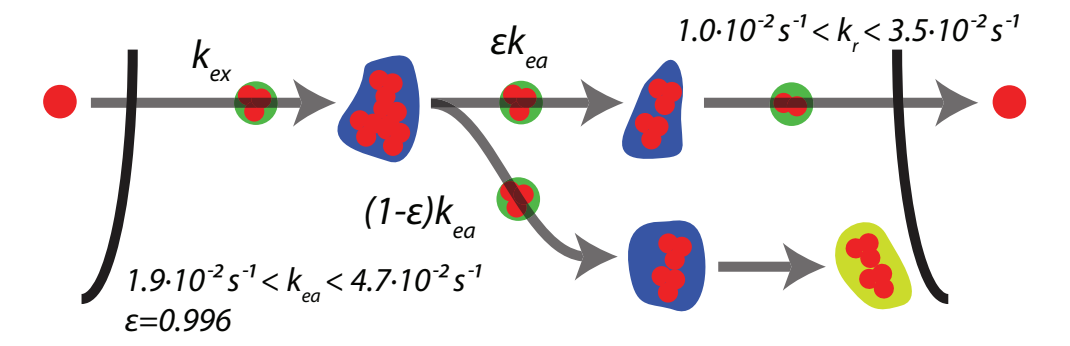


Figure 3.7: Summary of the obtained results.

Our data show that PICCS is a quantitative tool for addressing spatial and temporal correlations between interacting particles or proteins. The method alleviates restrictions which hampered previously developed methods. PICCS

reliably allowed us to measure the cross-correlation between two populations by which we arrived at quantitative insights into the subcellular mechanisms underlying intracellular Dpp transport. The results are summarized in fig. 3.7, where the estimations for the different rates are shown for the slow limit of intracellular transport. From the rates we found that the average residence time of Dpp in early endosomes is slightly shorter compared to recycling endosomes. Compared to the total life time of a Dpp molecule of 46 min [2] the average residence time in early and recycling endosomes is about 1 min for the slow limit and about 25 s for the fast limit. Furthermore we found that early endosomes contain on average almost twice as much Dpp compared to other endosomes. The results obtained are the first steps in a quantitative description of the transcytosis pathway in morphogen gradient formation.

Acknowledgements

The authors thank Ani Kicheva and Ortrud Wartlick for discussions and maintaining fly stocks. This work was supported by funds from the Human Frontiers Science Program Grant No. RGP66/2004, and the Dutch CYTTRON consortium sponsored by the Ministry of Economic Affairs.

3.A Appendix

3.A.1 Theory - Intracellular trafficking

The steady-state concentration of Dpp in each type of endosome in given cell n is calculated from eqs. (3.1) to (3.4)

$$C_{\text{ea}}^{n} = \frac{k_{\text{ex}} \left(C_{\text{ex}}^{n} + C_{\text{ex}}^{n+1} \right)}{2k_{\text{ea}}}$$
 (3.15a)

$$C_{\rm r}^n = \frac{\varepsilon k_{\rm ea} C_{\rm ea}^n}{k_{\rm r}} \tag{3.15b}$$

$$C_{\rm l}^n = \frac{(1-\varepsilon)k_{\rm ea}C_{\rm ea}^n}{k_l} \tag{3.15c}$$

$$C_{\text{ex}}^{n} = \frac{k_{\text{r}} \left(C_{\text{r}}^{n-1} + C_{\text{r}}^{n} \right)}{2k_{\text{ex}}}$$
 (3.15d)

Combining eqs. (3.15a), (3.15b) and (3.15d) gives

$$C_{\text{ex}}^{n} = \frac{1}{4} \frac{\varepsilon}{1 - \varepsilon} \left(C_{\text{ex}}^{n-1} - 2C_{\text{ex}}^{n} + C_{\text{ex}}^{n+1} \right)$$
 (3.16)

If the Dpp gradient varies on length scales which are large compared to the size of a cell, we can approximately write the right side of the above equation as a second derivative, which results in

$$C_{\rm ex} = \frac{1}{4} \frac{\varepsilon}{1 - \varepsilon} \frac{\rm d^2 C_{\rm ex}}{\rm dn^2}$$
 (3.17)

with solution

$$C_{\rm ex}(n) = C_{\rm ex}(0)e^{-\frac{n}{\lambda}}$$
 (3.18)

with the decay length λ in number of cells. Equation (3.16) and eq. (3.18) relate ε to λ , with

$$\varepsilon = \frac{2}{1 + \cosh(\lambda^{-1})} = 0.996$$
 (3.19)

using the experimentally determined value for λ (λ = 7.7 cells, [2]).

The total concentration of Dpp in endosomes $C_{\text{tot,endo}}^n$ in cell n is given by the sum of eqs. (3.15a) to (3.15c)

$$C_{\text{tot,endo}}^{n} = \frac{k_{\text{ex}}k_{\text{r}}k_{\text{l}} + \varepsilon k_{\text{ea}}k_{\text{l}}k_{\text{ex}} + (1 - \varepsilon)k_{\text{ea}}k_{\text{ex}}k_{\text{r}}}{2k_{\text{ea}}k_{\text{r}}k_{\text{l}}} \times \left(1 + e^{-\left(\frac{1}{\lambda}\right)}\right)C_{\text{ex}}^{n} \equiv \text{const.} \times C_{\text{ex}}^{n}$$
(3.20)

Thus the gradient of the intracellular Dpp concentration follows the extracellular gradient linearly.

3.A.2 Theory-Particle image cross-correlation spectroscopy

We consider 2 interaction partners whose fluorescence signals are labeled 'YFP' and 'CFP' without loss of generality. The goal is to find the correlation fraction and length from the spatial positions of the signals.

If P(x, y) is the probability to find two correlated signals separated by a vector (x, y), then the cumulative probability $P_{\text{cum}}(l)$ is found by integration of P(x, y) in polar coordinates

$$P_{\text{cum}}(l) = 2\pi \int_0^l dr P(r)$$
 (3.21)

with $r = \sqrt{x^2 + y^2}$.

The shape of the function $P_{\text{cum}}(l)$ depends on the nature of the interaction between the interaction partners and the positional accuracy for determination of the YFP and CFP signals. The experimentally observed P(x, y) is found from the convolution of the real correlation $P_{\text{corr}}(x, y)$, which is characteristic for a specific interaction, and the probability density $P_{\text{pos. acc.}}(x, y)$ describing the (apparent) correlation due to the finite positional accuracy [30].

$$P(x,y) = \int \int dx' \, dy' P_{\text{corr}}(x-x',y-y')$$

$$\times P_{\text{pos. acc.}}(x',y')$$

$$P_{\text{pos. acc.}}(x,y) = \frac{1}{2\pi\sigma^2} \exp\left(-\frac{x^2+y^2}{2\sigma^2}\right)$$
(3.22)

where $\sigma = \sqrt{2}\delta$ and $\sigma\delta$ is the one-dimensional positional accuracy.

In the simplest case, if the YFP and CFP signal are at the same position, $P_{\text{cum}}(l)$ is determined by the positional accuracy alone:

$$P_{\text{cum}}(l) = 1 - \exp\left(-\frac{l^2}{2\sigma^2}\right) \tag{3.23}$$

A fit of Eq. 3.23 to $P_{\text{cum}}(l)$ with σ as the free fit parameter results in a value for the one-dimensional positional accuracy $\sigma_{\text{pos. acc.}} = \sigma/\sqrt{2}$. More generally σ can be regarded as a typical correlation length.

To accurately describe the experimentally determined $P_{\text{cum}}(l)$ we found that we had to assume two correlation lengths (σ_1 and σ_2)

$$P_{\text{cum}}(l) = \beta \left(1 - \exp\left(-\frac{l^2}{2\sigma_1^2}\right) \right) + (1 - \beta) \left(1 - \exp\left(-\frac{l^2}{2\sigma_2^2}\right) \right)$$

$$(3.24)$$

where β is the fraction of data that has a correlation length σ_1 . We suppose that a broad distribution of positional accuracies explains this functional form of $P_{\text{cum}}(l)$.

Now we derive step-by-step the form of the correlation function $C_{\text{cum}}(l)$ given above in Eq. 3.10. If, per image, there is only one pair of correlated signals (for clarity they will be called 'YFP signal' and 'CFP signal') the correlation function $C_{\text{cum}}(l)$ equals $P_{\text{cum}}(l)$: $C_{\text{cum}}(l) = P_{\text{cum}}(l)$. If only for a fraction α of all YFP signals there is a correlated CFP signal, we observe $C_{\text{cum}}(l) = \alpha P_{\text{cum}}(l)$. Typically there is more than one YFP signal per image and therefore also more than one CFP signal. If l gets bigger, neighboring CFP signals in close proximity are counted by the PICCS algorithm although they are not correlated with the YFP signal. Additionally there might be CFP signals which are not correlated with any YFP signal. These CFP signals, in close proximity or not correlated with any YFP signal, lead to an additional contribution $c_{\text{CFP}} \cdot \pi l^2$ to $C_{\text{cum}}(l)$. Here we assume that the positions of the CFP signals follow a uniform random distribution with density c_{CFP} . In total $C_{\text{cum}}(l) = \alpha P_{\text{cum}}(l) + c_{\text{CFP}} \cdot \pi l^2$.

If there are no CFP signals in addition to the ones correlated with a YFP one, c_{CFP} can be calculated from the density of YFP signals c_{YFP} , the correlation fraction α and the image area A by

$$c_{\text{CFP}} = \alpha (c_{\text{YFP}} A - 1) / A = \alpha (c_{\text{YFP}} - 1 / A) \equiv c_{\text{CFP}}^*$$
 (3.25)

If $\alpha/A \ll c_{\rm YFP}$, $c_{\rm CFP} \approx \alpha c_{\rm YFP}$. In general $c_{\rm CFP} = c_{\rm YFP}^* + c_{\rm CFP, uncorr.}$, where $c_{\rm CFP, uncorr.}$ is the density of CFP signals which are not correlated with any YFP signal.

Non-random distribution of signals In any real life situation, the assumption that all CFP signals are distributed randomly with a uniform density is often violated. One reason is the diffraction limit: if two molecules are too close to each other (< 200 nm) their fluorescence signals will merge and only one signal is observed. Consequently, close to a given CFP signal the probability to find another signal is decreased. Additionally, there might be biological reasons for correlations between the CFP signals. For example, receptors might be distributed evenly (and non-randomly) to achieve a very homogeneous surface coverage. Any correlation between the positions of CFP signals will cause a deviation from the simple quadratic contribution $c_{CFP} \cdot \pi l^2$ we assumed. The influence of this correlation on the cumulative correlation $C_{\text{cum}}(l)$ between the two color channels depends on the distribution of distances between YFP and CFP signals $P_{\text{cum}}(l)$. We define the function s(r, l) as the number of CFP signals in a circle with radius l if the distance between the YFP signal and a correlated CFP signal is r. For YFP signals which have a correlated CFP signal, the contribution of uncorrelated signals can be written as

$$\alpha \int_0^\infty dr \, s(r, l) \frac{\partial P_{\text{cum}}}{\partial r}(r) \tag{3.26}$$

where $\partial P_{\text{sum}}(r)/\partial r$ gives the probability for a distance r between a pair of correlated signals. For YFP signals without correlated CFP signals, and assuming the simple quadratic dependence, we derive

$$C_{\text{cum}}(l) = \alpha P_{\text{cum}}(l) + (1 - \alpha)c \cdot \pi l^{2}$$

$$+ \alpha \int_{0}^{\infty} dr \, s(r, l) \frac{\partial P_{\text{cum}}}{\partial r}(r)$$
(3.27)

s(r,l) is determined empirically from the experimental data by correlation of a 'virtual' YFP channel image with the measured images from the CFP channel. The virtual YFP image is constructed from the CFP image by placing YFP signals at a distance r from a CFP signal. The $C_{\rm cum}(l)$ determined for a given r with the standard algorithm is equal to s(r,l). Typically the results from 20 virtual images (where the YFP signals are moved around on circles with radius r around the CFP signals) are averaged to obtain s(r,l).

Subsequent to the calculation of s(r, l) the correction is determined numerically by the following self-consistent algorithm:

- 1. as an initial guess for the correction term determine the slope of the linear part of C_{cum} and use the original correction term from eq. (3.10).
- 2. subtract the correction.
- 3. determine α as the average over the flat part of the resulting curve
- 4. normalize to 1 and fit the model eq. (3.11).
- 5. calculate the new correction according to eq. (3.27), go to step 2.

Steps 2 to 5 are repeated until the fit parameters change less than a predefined threshold.

3.A.3 Bleaching

Bleaching of the fluorescent label can influence the results. If one of the two fluorescent labels bleaches more quickly than the other, signals are lost and the correlation fraction will decrease over acquisition time. To confirm that the number of early endosomes (CFP signal) and Dpp-containing endosomes (YFP signal) stayed constant we measured the total number of detected endosomes per image stack (fig. 3.8). On average we detected 17 early endosomes in a field of view (1 early endosome per cell on average) and the number of observed endosomes was constant around this value. The average number of Dpp-containing endosomes found was 1.5 per cell. Since Dpp is also in the other endosomes we expected to find more Dpp-containing endosomes on average. Fluctuations in the number of detected endosomes were caused by movement of endosomes in and out of the image volume or by endosomes that were moving too close together to be detected individually. The latter effect is corrected for in the PICCS-algorithm.

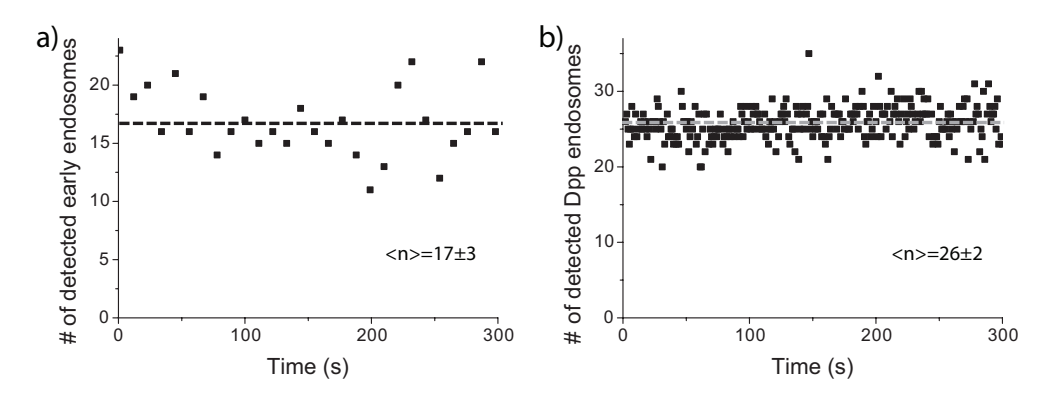


Figure 3.8: Number of detected endosomes per image stack for **a**) early endosomes and **b**) Dpp-containing endosomes. The number of endosomes (signals) in both channels stayed approximately constant. The average number of endosomes and the standard deviation are indicated for both cases.

3.A.4 Error scaling in PICCS

To design a successful experiment it is crucial to know how the error of the measured observables $(\alpha, c_{\text{CFP}}, \sigma)$ scales with the experimental and fitting parameters (fig. 3.9). We determined the error by application of the PICCS algorithm described above to simulated data, assuming that the signals are distributed randomly and uniformly in space and the correlations are governed by eq. (3.11). First, we assume that all CFP signals are correlated with a YFP signal, so $c_{\text{CFP}} = \alpha(c_{\text{YFP}} - 1/A)$, where A is the area of the image. Then we add additional CFP signals, which are not correlated with any YFP signal. For every set of parameters the simulations are repeated 100 times and the errors $\Delta \alpha$, δc_{CFP} , $\Delta \sigma$ are determined as the standard deviation.

Experimental parameters The experimental parameters are the correlation fraction α , the density of YFP and CFP signals c_{YFP} and c_{CFP} , the correlation length σ and the number of images M. As evident from fig. 3.10a all errors scale approximately like $1/\sqrt{M}$ where M is the number of acquired images. This behavior assures that any error can be made small just by acquisition of

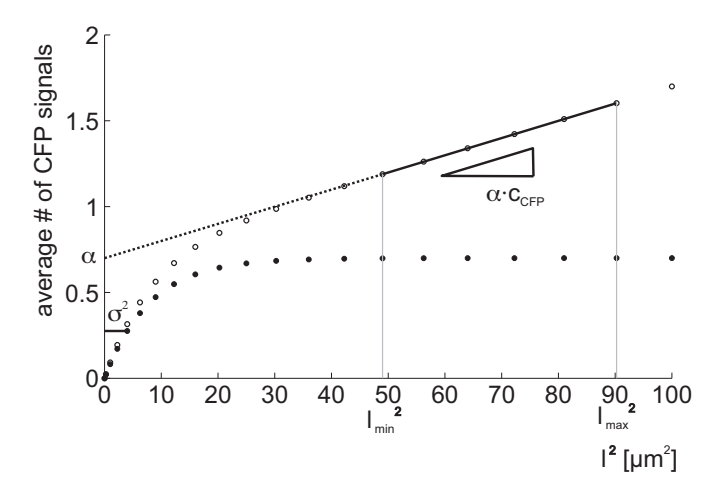


Figure 3.9: Experimental and fit parameters. The open circles correspond to $C_{\text{cum}}(l)$ calculated from simulated data. The closed circles give $C_{\text{cum}}(l)$ after subtraction of the linear contribution given by the dotted line. To determine the slope $\pi \cdot c_{\text{CFP}}$ of the linear contribution the $C_{\text{cum}}(l)$ is fitted to a straight line between l_{\min} and l_{\max} . The offset of this straight line is equal to the correlation fraction α . σ is equal to the distance l where the function $C_{\text{cum}}(l) - \pi \cdot c_{\text{CFP}} l^2$ has the value $\alpha \left(1 - \sqrt{e}\right)$

more images. The same scaling behavior is found for α , see fig. 3.10b. As to be expected, the relative errors become large if the correlation fraction is small or, equivalently, more images have to be acquired to achieve a certain accuracy. The dependence of the error on the density of YFP signals c_{YFP} is different for the various observables (fig. 3.10c). While the error for c_{CFP} scales like the inverse square root $(1/\sqrt{c_{\text{YFP}}})$, the errors of α and σ are fitted with the empirical model $A \cdot (c_{\text{YFP}}/\mu\text{m}^{-2})^{-0.5} + B \cdot (c_{\text{YFP}}/\mu\text{m}^{-2})^{0.25}$. This model has a minimum at $(2A/B)^{4/3}$, which implies that there is an optimal density c_{YFP} , where the errors are minimal. As will become clear below, the value of this optimal density depends on the fitting parameters. The errors of α and σ initially decrease with increasing c_{YFP} because of the higher number of YFP signals, which increases statistical significance. At the same time, c_{CFP} increases and therefore the con-

tribution $c_{\text{CFP}} \cdot \pi l^2$ increases relative to α . Consequently, the errors of α and σ increase for big densities c_{YFP} .

So far, all CFP signals had a corresponding (i.e. correlated) YFP signal. Now we add additional, non-correlated CFP signals. If the density of YFP signals c_{YFP} and the interaction fraction α are kept constant, α and σ scale approximately like $\sqrt{c_{\text{CFP}}}$ while the error of c_{CFP} scales like $1/\sqrt{c_{\text{CFP}}}$ (fig. 3.10d). As to be expected, the presence of extra CFP signals makes the determination of α and σ increasingly difficult. A change in the correlation length σ has significant influence only on the error for σ which scales like $1/\sqrt{\sigma}$. For increasing σ there are more data points in a region which is important for the determination of σ , namely where $P_{\text{cum}}(l)$ is significantly smaller than 1. The errors of α and c_{CFP} are approximately constant (fig. 3.10e).

Fitting parameters The fitting parameters are the length of the interval for the linear fit $l_{\rm max} - l_{\rm min}$, its center $l_{\rm center} = (l_{\rm max} - l_{\rm min})/2$ and the distance between two data points Δl (fig. 3.9). Figures 3.11a-c show that the general scaling behavior is independent on the position of the fit interval $l_{\rm center}$. However, the position of the minimum error of α and σ depends on $l_{\rm center}$: The bigger $l_{\rm center}$, the smaller the optimal density $c_{\rm YFP}$. Therefore, $l_{\rm center}$ should be as small as the data allows - of course, the fit interval must be in the region where $C_{\rm cum}(l)$ is linear when plotted versus l^2 . Figures 3.11d,e show the dependence on the errors on the length of the fit interval and the distance between data points respectively. The errors asymptotically become constant for big fit intervals and small distances between data points. Note that increasing $l_{\rm max}$ at constant $l_{\rm min}$ enlarges the fit interval but also moves its center $l_{\rm center}$, which is disadvantageous, see above.

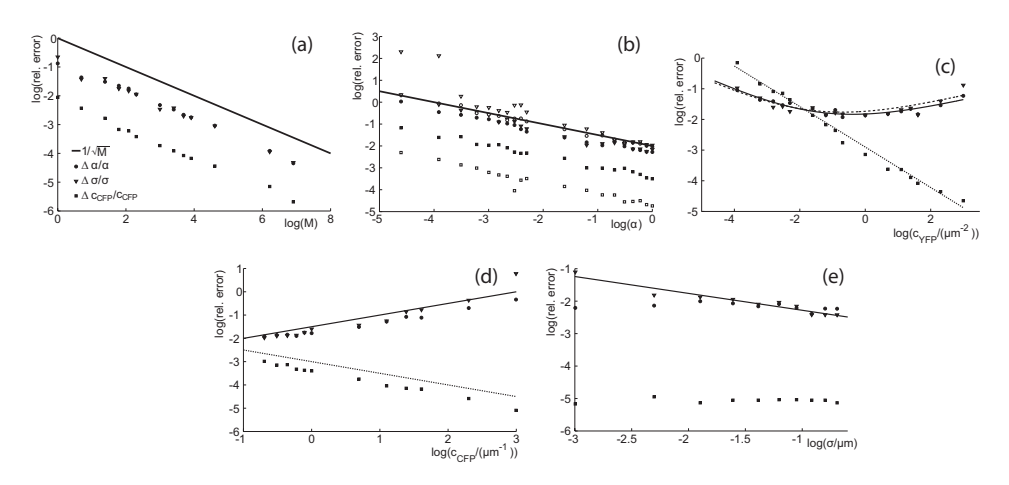


Figure 3.10: a) Dependence of the relative errors on the number of images M. The relative errors of α (circles), σ (triangles) and c_{CFP} (squares) all scale approximately like $1/\sqrt{M}$ (solid line). M = 10, $\alpha = 0.5$, $c_{YFP} = 0.5 \,\mu\text{m}^{-2}$, $\sigma = 0.15 \,\mu\text{m}$ b) Dependence of the relative errors on the interaction fraction α . The legend is the same as in fig. 3.10a, where $c_{YFP} = 1 \, \mu \text{m}^{-2}$ (closed symbols), $c_{YFP} = 10 \, \mu \text{m}^{-2}$ (open symbols), M = 10, $\sigma = 0.15$ um in both cases. The errors of all determined parameters approximately scale like $1/\sqrt{\alpha}$ (solid line), independent of the density c_{YFP} . c) Dependence of the relative errors on the density c_{YFP} . The legend is the same as in fig. 3.10a. The relative error of α (circles) and σ (triangles) are fitted with the model $A \cdot (c_{YFP}/\mu m^{-2})^{-0.5} + B \cdot (c_{YFP}/\mu m^{-2})^{0.25}$ (black solid and dashed line respectively). For $\alpha A = 0.04$, B = 0.12, which results in a minimum at 0.6 μ m⁻² and for $\sigma A = 0.07$, B = 0.14, which gives a minimum at 0.5 μ m⁻². The relative error of c_{CFP} (squares) scales approximately like $c_{\rm YFP}^{-2/3}$ (The gray solid line is a linear fit in the logarithmic plot given by $y = -0.66(c_{\rm YFP}/\mu {\rm m}^{-2}) - 2.9$). M = 10, $\alpha = 0.5$, $\sigma = 0.15 \ \mu {\rm m}$. **d**) Dependence of the relative errors on the density c_{CFP} . The legend is the same as in fig. 3.10a. The relative error of α and σ scale approximately like $\sqrt{c_{CFP}}$ (solid line), the relative error of c_{CFP} scales like $1/\sqrt{c_{\text{CFP}}}$ (dashed line). M = 10, $c_{\text{YFP}} = 1 \, \mu\text{m}^{-2}$, $\alpha = 0.5$, $\sigma = 0.15 \, \mu\text{m}$. e) Dependence of the relative errors on σ . The legend is the same as in fig. 3.10a. The relative error of α and c_{CFP} do not change significantly with σ . The relative error of σ scales approximately like $1/\sqrt{\sigma}$ (The solid line is a linear fit in the logarithmic plot given by $y = -0.52(c_{YFP}/\mu m^{-2}) - 2.8$) $M = 50, c_{YFP} = 1 \mu m^{-2}, \alpha = 0.5$.

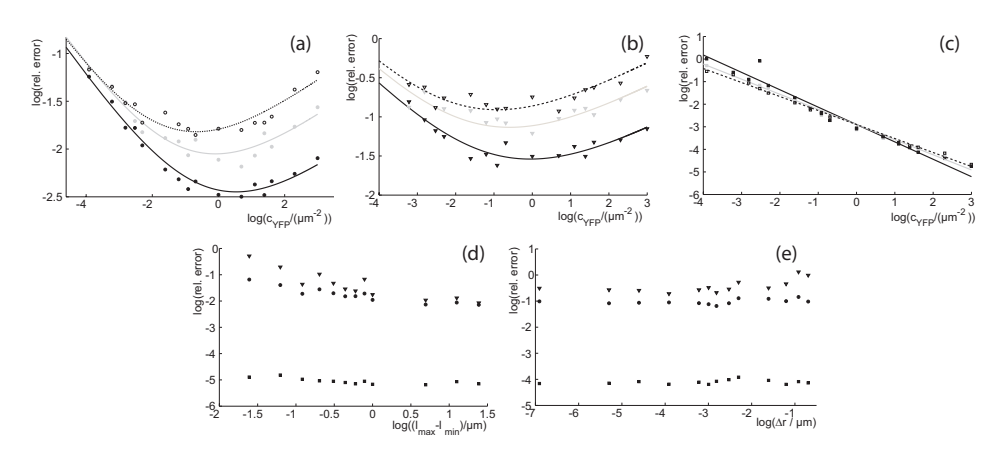


Figure 3.11: a) Dependence of the relative error of α on the center of the fit interval $l_{\text{center}} = (l_{\text{max}} - l_{\text{min}})/2$. The legend is the same as in fig. 3.10a, where $l_{\text{center}} = 0.925$ (solid symbols), $l_{\text{center}} = 1.175$ (gray symbols) and $l_{\text{center}} = 1.375$ (open symbols). The relative error of α is fitted with the model $A \cdot (c_{YFP}/\mu m^{-2})^{-0.5} + B \cdot (c_{YFP}/\mu m^{-2})^{0.25}$. A = 0.04, B = 0.05 (black solid line), A = 0.04, B = 0.09 (gray solid line) and A = 0.04, B = 0.13 (dashed line). That results in minima at 1.9 μ m⁻²,0.9 μ m⁻² and 0.5 μ m⁻² respectively. $M=10, \alpha=0.5, \sigma=0.05 \mu \text{m}$. **b)** Dependence of the relative error of σ on the center of the fit interval $l_{\text{center}} = (l_{\text{max}} - l_{\text{min}})/2$. The legend is the same as in fig. 3.10a, where $l_{center} = 0.925$ (solid symbols), $l_{center} = 1.175$ (gray symbols) and l_{center} = 1.375 (open symbols). The relative error of σ is fitted with the model $A \cdot (c_{YFP}/\mu m^{-2})^{-0.5} + B \cdot (c_{YFP}/\mu m^{-2})^{0.25}$. A = 0.07, B = 0.15 (black solid line), A = 0.08, B = 0.25 (gray solid line) and A = 0.09, B = 0.34 (dashed line). That results in minima at 0.9 μ m⁻², 0.6 μ m⁻² and 0.4 μ m⁻² respectively. M = 10, $\alpha = 0.5$, $\sigma = 0.05 \,\mu\text{m}$. c) Dependence of the relative error of c_{CFP} on the center of the fit interval $l_{\text{center}} = (l_{\text{max}} - l_{\text{min}})/2$. The legend is the same as in fig. 3.10a, where $l_{\text{center}} = 0.925$ (solid symbols), $l_{\text{center}} = 1.175$ (gray symbols) and $l_{\text{center}} = 1.375$ (open symbols). The relative error of σ is fitted with the straight line (in the logarithmic plot). The slope is -0.77 (black solid line) -0.67 (gray solid line) and -0.62 (dashed line). M = 10, $\alpha = 0.5$, $\sigma = 0.05$ µm. d) Dependence of the relative errors on the length of the fit interval $(l_{\text{max}} - l_{\text{min}})$. The legend is the same as in fig. 3.10a. M = 50, $\alpha = 0.5$, $\sigma = 0.15$ μm , $c_{YFP} = 1 \mu m^{-2}$. e) Dependence of the relative errors on the step size Δl (fig. 3.9). The legend is the same as in fig. 3.10a. M = 50, $\alpha = 0.5$, $\sigma = 0.15 \,\mu\text{m}$, $c = 1 \,\mu\text{m}^{-2}$.

Bibliography

- [1] Basler, K. and Struhl, G. Nature 368(6468):208-14 (1994).
- [2] Kicheva, A., Pantazis, P., Bollenbach, T., Kalaidzidis, Y., Bittig, T., Jülicher, F., and González-Gaitán, M. *Science* **315**(5811):521–5 (2007).
- [3] Crick, F. Nature **225**(5231):420–2 (1970).
- [4] Kerszberg, M. and Wolpert, L. *J Theor Biol* **191**(1):103–14 (1998).
- [5] Entchev, E. V., Schwabedissen, A., and González-Gaitán, M. *Cell* **103**(6):981–91 (2000).
- [6] González-Gaitán, M. Nat Rev Mol Cell Biol 4(3):213-24 (2003).
- [7] Kruse, K., Pantazis, P., Bollenbach, T., Jülicher, F., and Gonzalez-Gaitan, M. *Development* **131**(19):4843–4856 (2004).
- [8] Enderle, T., Ha, T., Ogletree, D. F., Chemla, D. S., Magowan, C., and Weiss, S. *Proc.Natl.Acad.Sci.U.S.A.* **94**(2):520–5 (1997).
- [9] Schütz, G., Trabesinger, W., and Schmidt, T. *Biophys. J.* **74**:2223 2226 (1998).
- [10] Trabesinger, W., Hecht, B., Wild, U., Schütz, G., Schindler, H., and Schmidt, T. *Analytical Chemistry* **73**:1100–1105 (2001).
- [11] Semrau, S. and Schmidt, T. Biophys. J. 92(2):613-621 (2007).
- [12] Schwille, P., Meyer-Almes, F., and Rigler, R. *Biophys. J.* **72**:1878 1886 (1997).
- [13] Comeau, J., Costantino, S., and Wiseman, P. *Biophys. J.* **91**:4611 4622 (2006).

80 BIBLIOGRAPHY

[14] Bollenbach, T., Kruse, K., Pantazis, P., Gonzalez-Gaitan, M., and Jülicher, F. *Physical Review e* **75**(1):011901 (2007).

- [15] Teleman, A. A. and Cohen, S. M. Cell 103(6):971–80 (2000).
- [16] Bobroff, N. Rev. Sci. Instrum. 57:1152–1157 (1986).
- [17] Schmidt, T., G.J.Schütz, Baumgartner, W., H.J.Gruber, and H.Schindler. *Proc. Nat. Acad. Sci. U.S.A.* **93**:2926–2929 (1996).
- [18] Ober, R. J., Ram, S., and Ward, E. S. *Biophys. J.* **86**:1185–1200 (2004).
- [19] Sönnichsen, B., Renzis, S. D., Nielsen, E., Rietdorf, J., and Zerial, M. *J Cell Biol* **149**(4):901–14 (2000).
- [20] Nagai, T., Ibata, K., Park, E. S., Kubota, M., Mikoshiba, K., and Miyawaki, A. *Nat Biotechnol* **20**(1):87–90 (2002).
- [21] Marois, E., Mahmoud, A., and Eaton, S. Development 133(2):307–17 (2006).
- [22] Holtzer, L., Meckel, T., and Schmidt, T. Applied Physics Letters **90**(5):053902 (2007).
- [23] Rink, J., Ghigo, E., Kalaidzidis, Y., and Zerial, M. *Cell* **122**(5):735–749 (2005).
- [24] Goldenring, J. R., Smith, J., Vaughan, H. D., Cameron, P., Hawkins, W., and Navarre, J. *Am J Physiol* **270**(3):G515–25 (1996).
- [25] Bökel, C., Schwabedissen, A., Entchev, E., Renaud, O., and González-Gaitán, M. *Science* **314**(5802):1135–9 (2006).
- [26] Ehrlich, M., Boll, W., Oijen, A. V., Hariharan, R., Chandran, K., Nibert, M. L., and Kirchhausen, T. *Cell* 118(5):591–605 (2004).

BIBLIOGRAPHY 81

[27] Saffarian, S., Cocucci, E., and Kirchhausen, T. *PLoS Biol* 7(9):e1000191 (2009).

- [28] Lander, A., Nie, Q., and Wan, F. Developmental Cell 2(6):785–796 (2002).
- [29] González-Gaitán, M. Mech Dev 120(11):1265-82 (2003).
- [30] Martin, D., Forstner, M., and Käs, J. Biophys. J. 83:2109-2117 (2002).

Chapter 4

Endosome motility and endosomal cargo dynamics mediate morphogen gradient formation

In the wing imaginal disc of *Drosophila melanogaster* positional information is provided by a concentration gradient of the morphogens Decapentaplegic (Dpp) and Wingless. Three transport mechanism govern formation and maintenance of the gradient. Here we focus on intracellular transport of Dpp. Using a 3D wide-field fluorescence microscope and particle tracking algorithms we were able to quantify the role of endosome mobility and endosomal cargo dynamics in intracellular Dpp transport.

We found that the lateral motility of endosomes by itself cannot account for effective intracellular transport. In the apicobasal direction however directed transport was observed during 6% of the time, with velocities that agreed with previously found values for molecular motors. The function of this endosomal transport remained unclear, but we speculate that it might play a role in Dpp degradation. We characterized the spatio-temporal endosomal Dpp distribution in the wing disc in all three dimensions *in vivo* and found it to be single-exponential, identical to the distribution of the complete Dpp population. The number of endosomes however remained constant throughout the disc. Endosomes contained up to 250 Dpp molecules allowing us to follow endosomes for hundreds of frames with high accuracy. Sudden changes in Dpp content of up to 25 Dpp molecules were observed, indicating that vesicles traveling between endosomes contain multiple Dpp molecules both before fusion with an endosome, and after fission from an endosome. The time between Dpp in- and outflow events was found to be about one minute. Dpp outflow was found to be a passive, probabilistic process. Combining these results suggested the presence of an immobile Dpp fraction, similar to what was observed with FRAP experiments before.

Our study is the first study to quantify intracellular Dpp transport on the level of individual endosomes. The results on the role of endosomal motility and endosomal cargo dynamics will have to be integrated in the future into a more detailed model describing intracellular Dpp transport.

4.1 Introduction

Almost 60 years ago Turing proposed that morphogens are providing the positional information in morphogenesis [1]. Wolpert in turn further developed a model in which morphogens are produced only by spatially localized cells. This then leads to the formation of a morphogen gradient in the surrounding 'receiving' tissue [2]. The position of a cell is hence coded into its position in a morphogen gradient. In the receiving tissue, the morphogen is detected by receptors on the cell surface. Depending on the morphogen concentration, cells will change their gene expression pattern accordingly. While the concept of morphogen gradients is now accepted for decades, the mechanism underlying the formation of these gradients on the cellular, sub-cellular and molecular level has only started to become understood in recent years. The formation of a stable gradient requires three mechanisms: production of the morphogen, spreading to neighboring cells and finally degradation of the morphogen.

In what follows we focus on morphogen spreading in tissue. For this process three mechanisms have been proposed: (i) diffusion in the extracellular matrix [3], (ii) receptor-mediated transport along the cell membrane [4] and (iii) intracellular transport [5], a sequential sequence of endocytosis of the morphogen-receptor complex followed by recycling and release of the morphogen into the extracellular matrix [6].

We studied the spreading of the morphogen Decapentaplegic (Dpp), a member of the TGF- β superfamily, which plays a major role in the development of the fruit fly *Drosophila melanogaster*. Dpp is expressed in a stripe of cells (the 'source') at the anterior-posterior compartment boundary (fig. 4.1a) of the wing imaginal disc [8]. The wing imaginal disc is a precursor of the later wing (fig. 4.1b). Figure 4.1c shows a schematic xz projection (a cross-section perpendicular to the dorso-ventral axis) of the wing imaginal disc consisting of two layers of distinct cells. The peripodial layer on top and the columnar cells beneath in which the Dpp gradient is present. The producing cells are indicated with a green bar in fig. 4.1c. From these producing cells Dpp is secreted to neighboring cells where it forms an exponential gradient in the wing epithelium [5, 9, 10]. In a recent experimental study of the Dpp gradient it was

4.1 Introduction 85

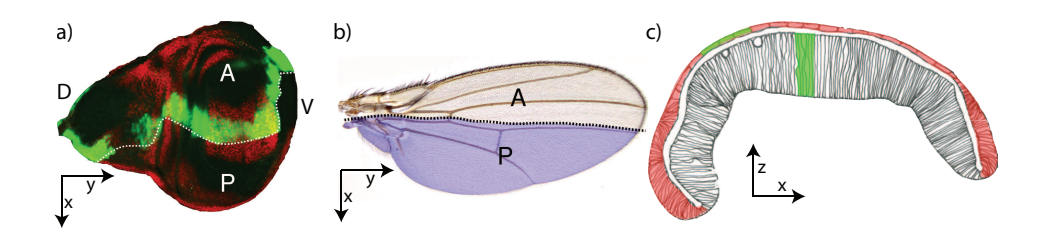


Figure 4.1: The wing imaginal disc. The x, y and/or z-axes are indicated in each subfigure. **a)** Top view of the wing imaginal disc showing the anterior (A) and posterior (P) compartment. The Dpp source (green) is located at the A-P compartment boundary. The dorsal (D) and ventral (V) sides are also indicated. **b)** Wing of a mature fly with the anterior and posterior compartment indicated. **c)** Schematic cross-section of a wing imaginal disc perpendicular to the D/V-axis. The Dpp source is indicated by the green color. (images from [5, 7])

shown that the formation of the gradient is a combination of Dpp production, Dpp spreading throughout the tissue and Dpp degradation within the cells as described by

$$\partial_t C(x,t) = D_{\text{eff}} \nabla^2 C - kC + 2j_0 \delta(x)$$
 (4.1)

in which C(x,t) is the Dpp concentration at time t and distance to the source x. With confocal fluorescence microscopy quantitative values for the effective diffusion coefficient $D_{\rm eff}$, the degradation rate k and the production rate j_0 have been obtained [10]. While in the latter study the actual Dpp transport mechanisms were modeled with one effective diffusion coefficient $D_{\rm eff}$, here we report on experimental findings that describe morphogen spreading by subcellular processes which finally lead to the effective coefficients and rates reported. Our experimental work is in line with ongoing theoretical efforts to describe Dpp spreading on the cellular and subcellular level [7, 11, 12].

4.1.1 Intracellular Dpp transport

Here we experimentally study the intracellular transport of Dpp in wing epithelia on the cellular and sub-cellular level by analyzing endosome motility

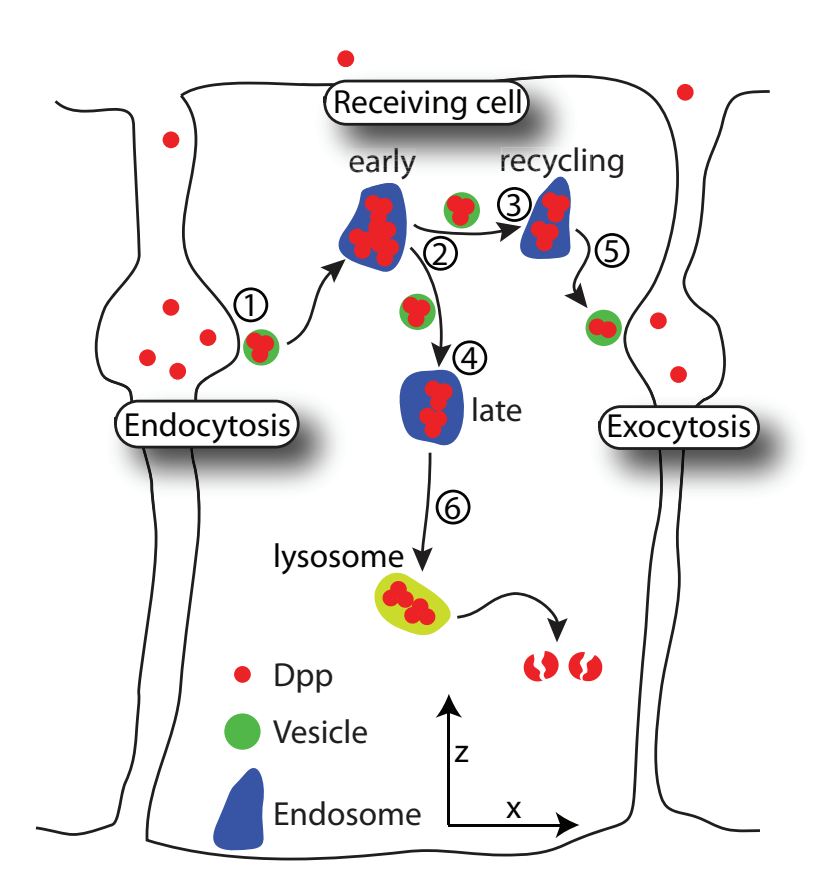


Figure 4.2: Schematic drawing of intracellular Dpp transport. Numbers indicate the different events that occur: 1) Dpp endocytosis into a vesicle and concurrent fusion with an early endosome. 2) Fission of a vesicle containing Dpp from an early endosome. 3) The vesicle from (2) going to a recycling endosome. 4) The vesicle from (2) going to a late endosome. 5) Fission of a vesicle from a recycling endosome and concurrent exocytosis. 6) Fission of a vesicle from a late endosome to a lysosome. Intracellular Dpp transport is non-directional. Any directionality of Dpp transport as suggested in this figure is for clarity purposes only.

4.1 Introduction 87

and monitoring the concentration of Dpp in endosomes. Intracellular Dpp transport plays a major role in gradient formation. This idea is supported by experiments in which intracellular Dpp transport was selectively blocked within part of the tissue by locally defined genetic shut down of endocytsosis [5]. The intracellular transport of Dpp is schematically shown in fig. 4.2. In this model we distinguish different events ¹:

- 1. Endocytosis of Dpp into a vesicle with concurrent fusion of this vesicle with an early endosome (+).
- 2. Fission of a vesicle containing Dpp from an early endosome (-)
- 3. after which it can go either to a recycling endosome (+)
- 4. or into a late endosome (+).
- 5. Fission of a vesicle containing Dpp from a recycling endosome and concurrent recycling of the Dpp into the extracellular matrix (-).
- 6. Fission of a Dpp-containing vesicle from a late endosome to a lysosome for degradation (-).

Such sequential processes are best described in terms of a system of rate equations in which a change in endosomal Dpp concentration dC is related to a rate k_i and the Dpp concentration c_i in the vesicle that is involved in process i. The change in concentration for each endosome is described by:

$$\partial_t C_{\text{early}} = c_1 k_1 - c_2 k_2 \tag{4.2a}$$

$$\partial_t C_{\text{recycle}} = c_3 k_3 - c_5 k_5 \tag{4.2b}$$

$$\partial_t C_{\text{late}} = c_4 k_4 - c_6 k_6 \tag{4.2c}$$

¹For each event it is indicated in parenthesis if the Dpp concentration in the specified type of endosome increases (+) or decreases (-). For each event the corresponding number is indicated in fig. 4.2.

Further we identify from fig. 4.2 that a vesicle that originates from an early endosome (event 2) will transfer either to a recycling endosome (event 3) or a late endosome (event 4). As the Dpp concentration in this vesicle will not change during these events $(2\rightarrow 3 \text{ or } 2\rightarrow 4)$ $c_2=c_3+c_4$. Knowledge of the parameters involved in the coupled differential equations will provide us with the full description of intracellular Dpp transport.

Theoretical calculations have estimated that one cycle of intracellular transport has a duration between 50 and 150 s [6, 13]. In a companion study to the current one we determined rates k_2 and k_5 of the events described above using Particle Image Cross-Correlation Spectroscopy (PICCS, chapter 3). By labeling both Dpp and early endosomes we estimated the off rates for the 'fission' events by determining the cross-correlation between both populations using the PICCS algorithm.

Much of the previous work on Dpp gradients has been done with conventional fluorescence microscopy. Here we build on our expertise in the field of single-molecule wide-field fluorescence microscopy [14, 15] which has distinct advantages over confocal microscopy in imaging speed and sensitivity and allows for straightforward determination of the Dpp concentration in endosomes. While in the companion study we focused on the kinetic parameters for Dpp transport, here we study how intracellular transport is actually facilitated. In particular we investigated:

- 1. Do endosomes or the vesicles travelling between endosomes control Dpp transport?
- 2. What are the other roles of endosomes we see?
- 3. Do Dpp molecules travel individually or in clusters during intracellular transport?
- 4. Is there evidence for directionality in intracellular transport?

By employing single particle tracking methods we studied all those questions and developed a quantitative description of intracellular Dpp transport on the level of individual endosomes.

4.2 Materials and methods

4.2.1 Sample preparation

The *UAS-Venus-Dpp* line was generated by using the existing *UAS-GFP-Dpp* vector [5] where GFP was replaced by Venus [16]. dpp^{d8}/dpp^{d12} ; dppGal4/UAS-Venus-Dpp flies have an identical wing phenotype to the dpp^{d8}/dpp^{d12} ; dppGal4/UAS-GFP-Dpp flies [5]: they survive to adulthood and have normally patterned wings, although smaller in size (data not shown). To obtain wing imaginal discs third instar larvae (dpp-Gal4/UAS-Venus-Dpp) were dissected in Clone8 medium (Schields & Sang M3 Medium containing 2% Fetal Calf Serum, 2.5 % Fly Extract, 12.5 IU Insulin/100 ml medium and 1X Penicillin/Streptomycin) after which the wing imaginal discs were mounted in a custom-made sample holder. Nail polish was used for sealing of the sample holder. The wing imaginal discs were imaged approximately 10 min after dissection. Samples were discarded 1 hour after dissection.

4.2.2 Data acquisition

A transmission image of a wing imaginal disc is shown in fig. 4.3a. When the sample is excited by a mercury lamp (excitation in the 500-520 nm range) the fluorescence from the DppVenus is clearly seen (fig. 4.3b). Magnification of the source area shows endosomes containing Dpp (fig. 4.3c). After addition of low concentrations of the membrane marker FM4-64 (Invitrogen, Leiden, The Netherlands) to wing disc during preparation, both the Dpp-Venus fluorescence (fig. 4.3c, λ < 600 nm) and the cell membranes (fig. 4.3d, λ > 600 nm) become visible. Overlaying both images (fig. 4.3e) allows us to assign each endosome to a specific cell.

Experiments were carried out on a wide-field fluorescence microscope capable of three dimensional particle-tracking through astigmatism [17]. The setup was additionally combined with a piezo-driven objective holder (Physik Instrumente, Karlsruhe, Germany) to move the objective in axial direction at 10 nm-precision. A motorized sample stage (Märzhäuser, Wetzlar, Germany)

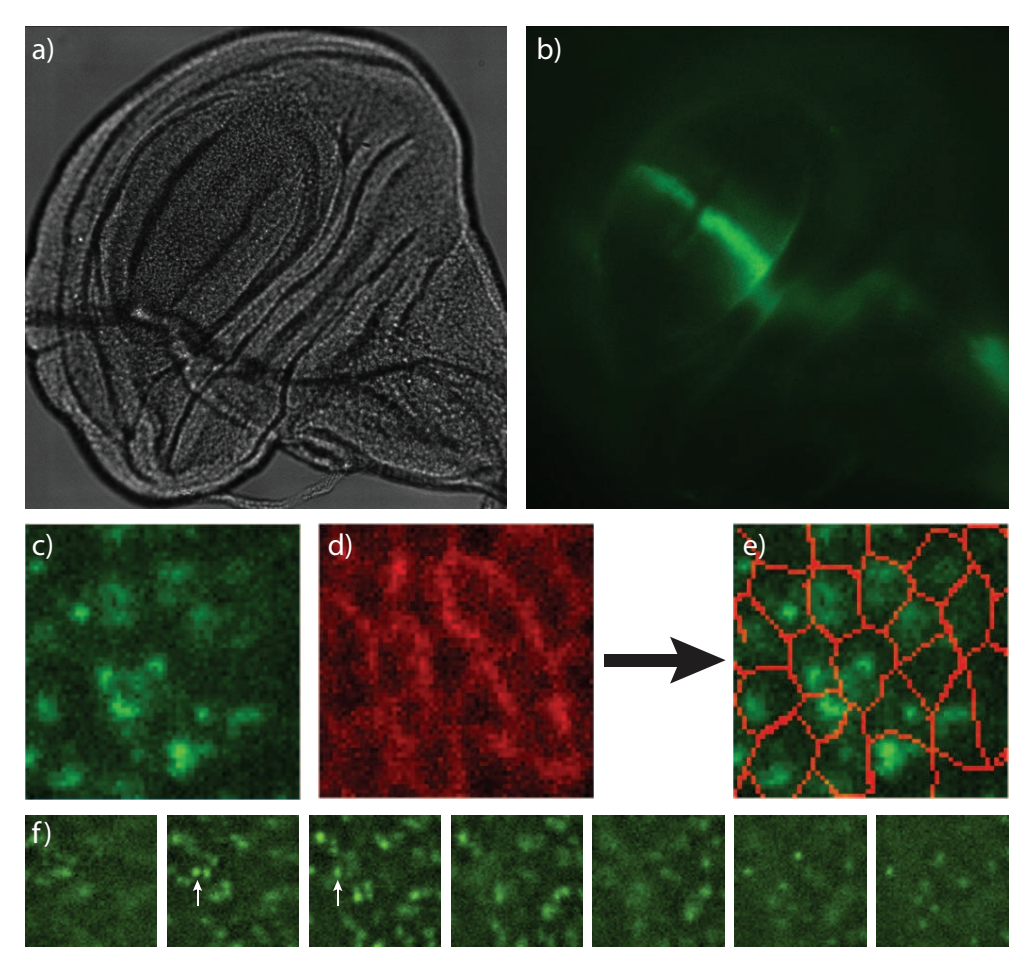


Figure 4.3: a) Transmission image of a wing imaginal disc directly after dissection. b) The same wing imaginal disc, now excited by a fluorescent lamp (500-520 nm). Dpp-Venus can be clearly seen, especially in the Dpp producing cells. The location of the Dpp source is indicated, together with the anterior-posterior compartment boundary which marks the border between producing and receiving cells. In the receiving cells a gradient is observed. c) A close-up of the receiving cells, individual Dpp-containing endosomes can be clearly seen. d) The same area as in (c), but now imaged in the red channel, showing the fluorescence of membrane-marker FM4-64, clearly outlining the columnar cells. e) Merge of images (c) and (d). f) Typical data obtained during an experiment in one image stack. Each image corresponds to a different z-position going from very apical (left image) to more basal (right image) with a distance of 0.7 µm between the planes. Out-of-focus fluorescence is removed in these images for clarity.

was used to move the sample in lateral direction with sub-micrometer accuracy. Image stacks with 5 to 8 image planes were generated in order to image large volumes. The distance between planes was set between 0.7 and 1.0 μ m such that endosomes appeared in at least two planes. The time between planes was kept as short as possible (typically 40 ms) to prevent large movements of endosomes between planes, while allowing enough time for the piezo to move the objective. Imaging was done in the apical region of the wing imaginal disc. A typical image stack is shown in fig. 4.3f, where 7 planes with $\Delta z = 0.7~\mu$ m were imaged. Endosomes containing Dpp-Venus were clearly identified in at least two images at the same time. The movement of endosomes between two consecutive planes was negligable. The astigmatism introduced for 3D position determination is visible in the images (see the endosome indicated by the white arrows in fig. 4.3f).

4.2.3 Data analysis

Positional information of endosomes was obtained as described before [17]. The method of fitting elliptical 2D-Gaussian profiles to the image of a single particle was extended here to incorporate image stacks. A stack of elliptical 2D-Gaussians was simultaneously fitted to the data, effectively producing a 3D-Gaussian profile. From this fitting procedure we obtained a static characterization for each experiment. A typical analysis output is shown in fig. 4.4. Each graph summarizes data from all endosomes detected during one experiment at all time points. Figure 4.4a shows the distribution of the local background for each endosome in the first image stack. This is a measure for the out-of-focus fluorescence. The background has a mean value of 625 ± 20 cnts, with a standard deviation of 117 cnts. This value is much smaller than the average signal observed from an individual endosome of $\overline{I} = 8.6 \pm 0.8 \cdot 10^3$ cnts, with a standard deviation of $4.4 \cdot 10^3$ cnts, as shown in fig. 4.4b. A wide range of intensities was observed in this experiment, reflecting the differences and changes in the Dpp concentration in endosomes and photobleaching of the Dpp-Venus.

The black curve in fig. 4.4b shows the intensity distribution for single YFPs attached via a membrane anchor to human embryonic kidney cells [18]. The

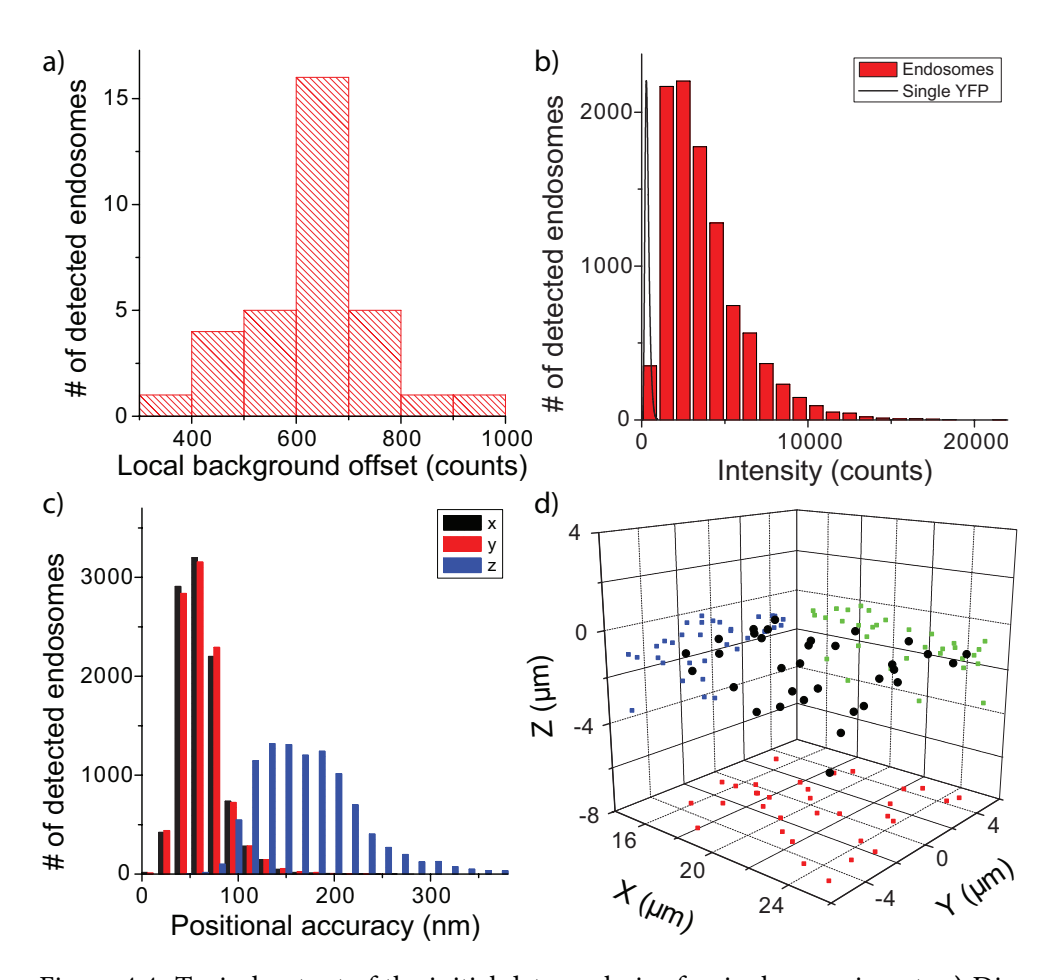


Figure 4.4: Typical output of the initial data analysis of a single experiment. **a**) Distribution of background values (CCD counts) associated to each detected endosome in the first image stack of the experiment. **b**) Distribution of all intensities for every endosome detected during the whole experiment (bar plot). For this plot each image stack is treated individually and therefore one endosome appearing in multiple image stacks will contribute multiple data points to this plot. The intensity distribution of single YFP proteins is plotted (black line) and the intensity is scaled for better comparison with endosome intensities. **c**) Distribution of the positional error for localizing an endosome for each dimension (x in black, y in red and z in blue), again for the whole experiment. **d**) Location in x (distance to the source), y and z for each detected Dpp endosome in the first image stack.

distribution peaked at 281 cnts. This distribution was already corrected for the different exposure time and excitation intensity used in the Dpp experiments. In doing so we assumed that the fluorescence intensity of YFP scales linearly with both parameters, since both experiments were performed in the non-saturating regime for YFP (excitation intensity $I_{\rm ex}=0.1\,{\rm kW/cm^2}$ was far below the saturation intensity [19]). Furthermore we assumed that quenching of fluorescence does not play a significant role inside the endosome given that the average distance between Dpp molecules in a 400 nm diameter endosome containing 100 Dpp molecules is approximately 80 nm.

To be able to calculate the number of Dpp molecules in an endosome it was necessary to correct the measured endosome signal for photobleaching. This was done by calculating a photobleaching curve for each experiment from the average signal per detected endosome and image stack for an entire movie. The fact that there were a large number of endosomes (> 15) in each image stack rendered this strategy reliable. We found that DppVenus bleached following a bi-exponential decay with offset as reported earlier by others [20]. The bleaching curve was subsequently fitted to a bi-exponential decay, the parameters obtained in this way (typical values τ_1 = 7 images, τ_2 = 244 images, offset = 2000 counts) were further used to correct the intensity of each individual endosome in retrospect.

To determine Dpp concentration changes in endosomes we used a step-fitting algorithm developed by Kerssemakers et al. [21]. We decided for the latter algorithm as it directly accounts for noise and no pre-filtering of the data is needed (for a review of other algorithms see [22]). Small steps of a few Dpp, however, were difficult to observe due to the unavoidable background fluorescence present in tissue. Furthermore, since photon shot noise has a bandwidth of a few Dpp, small changes on short time scales were not detected.

The positional accuracy by which the x, y and z coordinates of each endosome were determined is shown in fig. 4.4c. Since the positional accuracy is inversely proportional to the square root of the number of detected photons, endosomes with more Dpp were detected more accurately. Photobleaching slightly reduced positional accuracy. As shown before the positional accuracy in axial direction $\Delta z = 172$ nm is approximately 2.5 times that in lateral di-

rection $\Delta x = \Delta y = 64\,$ nm [17]. Finally fig. 4.4d shows the positions of the detected endosomes during the experiment showing that most of the endosomes where located in an apical slice of 4 μ m at about 1 μ m inside the tissue. After locating the endosomes in each image stack, endosome trajectories were reconstructed by using a particle tracking algorithm that has previously been described [14, 17]. With this approach the 3D position of each endosome as well as its Dpp content was followed for a long period (up to 600 time points).

Trajectories were further analyzed [23] in order to detect different types of motional behavior for each endosome. Free diffusion was classified against confined diffusion and against directed transport. For parts of trajectories were free diffusion was detected, a mean squared displacement (MSD) versus time plot was generated from which the diffusion coefficient *D* was calculated

$$MSD = 2nDt + \sum 2\sigma_n^2 \tag{4.3}$$

in which n is the dimensionality of the data and σ_n the positional accuracy in the nth dimension. To locate parts of a trajectory where directed motion is occurring an 'asymmetry' parameter was calculated following the methodoogy described by [23]. The trajectory of a transported object will be highly asymmetric, showing up as an asymmetry parameter larger than 1. As argued by [23] this value is indicative of a probability > 99% that the object undergoes directed motion. After analysis of the asymmetry parameter, in the case of directed transport, the MSD versus time plot was calculated on the part of the trajectory where asymmetry > 1 and fitted to

MSD =
$$2nDt + (vt)^2 + \sum 2\sigma_n^2$$
 (4.4)

from which the average velocity v of the endosome during the transport period was obtained [24].

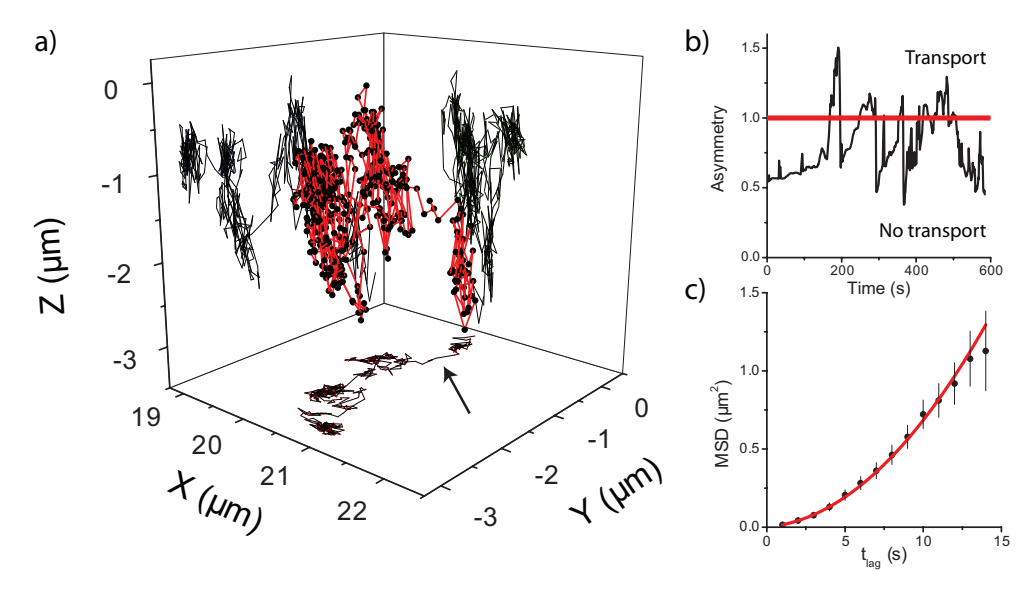


Figure 4.5: **a)** Trajectory (total length = 600 s) of an endosome undergoing transport in the lateral direction during a short period (15 s). The distance to the Dpp source is indicated on the *x*-axis. **b)** Three-dimensional asymmetry parameter of the trajectory versus time. Values above 1 indicate a high probability that directed motion is occurring. **c)** Mean squared displacement versus time lag for the part of the trajectory indicated with the arrow. From a fit to eq. (4.4) we found that the endosome was transported with an average velocity $v = 78 \pm 20 \text{ nm/s}$.

4.3 Results-Endosome mobility

4.3.1 Intracellular transport by endosomes

The simplest form of intracellular transport would be endocytosis of Dpp, followed by a short period of transport or diffusion through the cytosol and subsequent exocytosis. During a typical experiment with a duration of 600 s we expected these events to be frequently observable given that the estimated time of intracellular transport lies between 50 s and 150 s [6, 13, 25]. In particular, our experiments were intended to unravel whether intracellular transport was mainly diffusion-driven or whether it was directional.

Previous experiments suggested that on macroscopic length scales intracellular transport was non-directional [5]. Indeed, on the (sub)cellular level we did not observe any significant long-range endosome transport over the whole width of a single cell (typical cell diameter 2.6 µm). In total 48 wing-disc preparations were analyzed, of which 15 preparations contained trajectories of a satisfactory quality (no significant sample drift and endosomes were visible during the whole experiment). Each experiment provided between $5 \cdot 10^3$ and 10^4 endosome positions of which typically around 200 endosome trajectories were obtained with average length of 25 steps (exponentially distributed). Of those, trajectories of lengths > 30 steps (Δt > 30 s) were further analyzed (typically 10 < N < 60 for one experiment). One wing imaginal disc (on average 17 cells were visible in our experiments) was analyzed more thoroughly for endosome motility and we found that only 14% of long trajectories covered the whole diameter of a cell, and that this movement took significantly longer than 150 s.

As an example of this movement, fig. 4.5a shows an endosome trajectory of length 600 s showing clear directed transport in the xy-plane on a length scale that matched the typical cell size. From the three-dimensional asymmetry parameter (fig. 4.5b) it became clear that the endosome underwent directed transport in parts of its trajectory. For one of those stretches lasting for $\Delta t = 15$ s the two-dimensional (xy) MSD was calculated (fig. 4.5c.) From a fit to eq. (4.4) the average lateral velocity by which this endosome was trans-

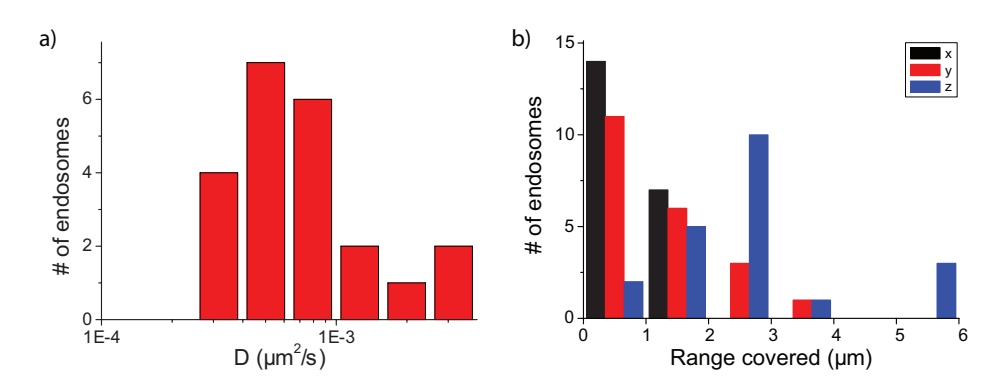


Figure 4.6: **a)** Distribution of two-dimensional (xy) diffusion coefficients D for Dpp-containing endosomes. **b)** Distribution of the range in which each endosome moves. For each dimension (x (along the gradient), y (perpendicular to the gradient), z (api-cobasal)) the range is plotted. Endosomes clearly were more mobile in axial as compared to lateral direction.

ported was $v = 78 \pm 20$ nm/s. This value is lower than what is typically found in comparable systems [26, 27]. Hence, although we found trajectories which could account for directed transport, the fact that we observed only few of these events and that the observed velocities were low, rules out that they are the main mediators of intracellular Dpp transport. In general we therefore rule out that the motion of endosomes is facilitating intracellular transport or is causing directionality herein.

For non-directional intracellular transport, endosomes do not need to cover the whole diameter of a cell. They could travel from one position, close to the cell membrane, to a random other one, either by diffusion or directed transport and carry Dpp along with them. Here we analyzed whether diffusion of endosomes was sufficient to play a role in intracellular Dpp transport. Therefore we calculated the two-dimensional MSD versus time lag for each endosome. We estimated the two-dimensional (xy) diffusion coefficient D by fitting eq. (4.3) to the data for $1 \text{ s} \leq t_{\text{lag}} \leq 25 \text{ s}$ for each individual endosome. The measured distribution of diffusion coefficients is shown in fig. 4.6a. The mean diffusion constant which characterizes endosome transport was $\langle D \rangle =$

 $8.9\pm1.5\cdot10^{-4}~\mu m^2/s$. If we however do not take into account the endosome population which covered the range of a whole cell during the experiment (14%) we obtain $\langle D \rangle = 6.9\pm1.0\cdot10^{-4}~\mu m^2/s$. For the upper limit (150 s) for intracellular Dpp transport an endosome would cover on average an area of 0.4 μm^2 or a typical distance of 0.6 μm . For effective intracellular transport this value is on the low side when compared to the cell diameter, also since most of the endosomes were usually not close to the cell membrane. Therefore we rule out here that mobility of whole endosomes will govern or facilitate intracellular Dpp transport.

4.3.2 Axial endosomal movement

So far we addressed lateral (xy) motion of endosomes. In what follows the axial (z, along the apicobasal axis) movement will be further evaluated. Since the observed lateral diffusion coefficients were small and lateral movement was small compared to the cell diameter, we did not expect to see a difference between lateral and axial movement. Lateral movement was even so small that during the timeframe of our experiments (t=600 s) we did not observe any influence of the cell membrane and we did not find lateral confinement with the size of the cell diameter. In fig. 4.6b a histogram is plotted showing the distribution of ranges each endosome covered during the experiment. The average covered range in x and y is $0.76\pm0.09~\mu m$ and $1.1\pm0.2~\mu m$, respectively. In z the average range covered by an endosome equals $2.5\pm0.3~\mu m$, more than twice the range for lateral movement. Hence we found a clear difference between lateral movement and movement along the apicobasal axis.

In fig. 4.7a a trajectory from an endosome showing preliminar apicobasal directed motion is plotted. From the yz and xz projections it was clear that the range of movement of the endosome in z was larger than in lateral directions. From the asymmetry parameter (fig. 4.7b) several periods of directed transport were detected. For one of these periods, indicated with an arrow in fig. 4.7a the MSD versus time plot is shown in fig. 4.7c. During that period the endosome was transported at an average velocity $v = 283 \pm 32$ nm/s. This value is well in the range of velocities observed for intracellular transport by molecular motors

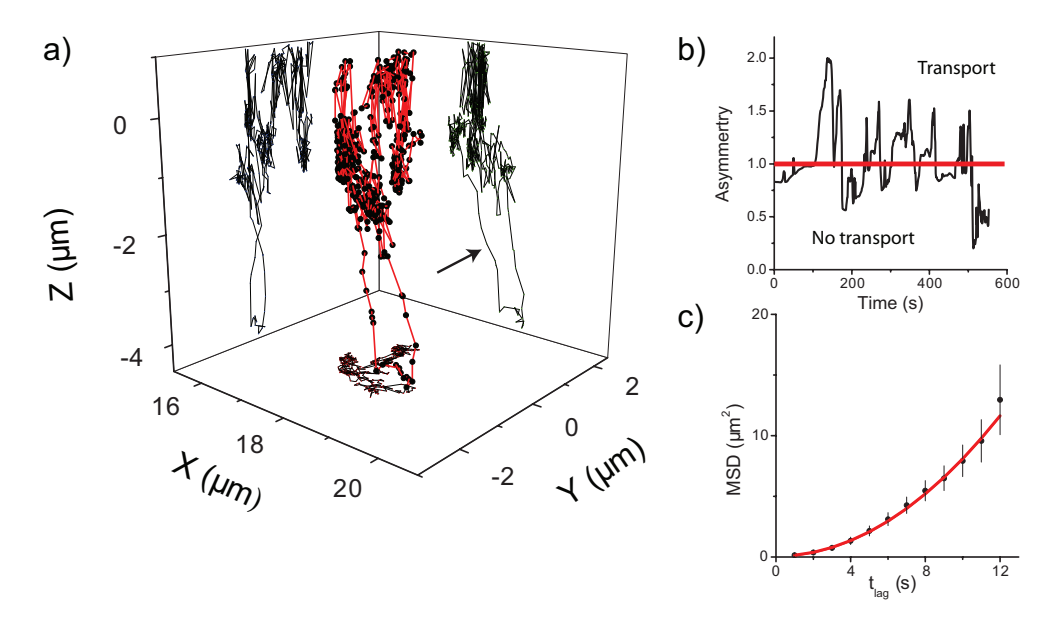


Figure 4.7: **a)** 3D trajectory of a Dpp-containing endosome showing movement in x, y and z. **b)** Asymmetry parameter of the trajectory shown in a). **c)** MSD versus time plot of the part of the trajectory indicated with the arrow. Directed transport was observed for 12 s and the endosome had an average velocity $v = 283 \pm 32$ nm/s.

[26, 27]. Therefore we assume that this particular endosome was transported by molecular motors during a period of 12 s thereby traveling a distance of 3.4 μ m. We excluded the possibility that the tissue as a whole was moving in axial direction, since the axial movement of the other observed endosomes was not correlated to the axial movement of the endosome shown in fig. 4.7.

We analyzed all long trajectories in this wing imaginal disc (N=27 trajectories) according to the methodology delineated in fig. 4.7. Figure 4.8a shows the distribution of axial velocities for directed transport events, characterized by an average of $\overline{v_z}$ = 212±13 nm/s. Thereby axial transport lasted between 3 s and 15 s with average duration of 7.6±0.4 s (fig. 4.8b). It should be noted that short (< 3 s) periods of transport were not detected due to the temporal threshold that had to be introduced into the trajectory analysis algorithm. Likewise slow movements (< 50 nm/s) were not reliably detected if they occurred over short periods of time. Averaged over periods of transport, during single transport events endosomes travelled in axial direction by 1.4±0.1 µm (fig. 4.8c). When we summed the duration of all the periods of directed transport, we found that in 6% of the time endosomes were clearly transported in the *z*-direction.

If all directed transport events were independent of each other, the distribution of the time between events is expected to peak around 124 s (i.e. equal to the total time without directed motion divided by the number of detected directed motion events). Our data however showed a completely different distribution, as shown in fig. 4.8d. In 56% of the cases transport in the z direction (either apical or basal) was followed by transport in the opposite direction within 17 s. In 32% of the cases reversal of transport is almost instantaneous. Such a large fraction of trajectories showing fast reversal of the direction of transport cannot be a result of random events. These events were most likely actively driven and therefore correlated.

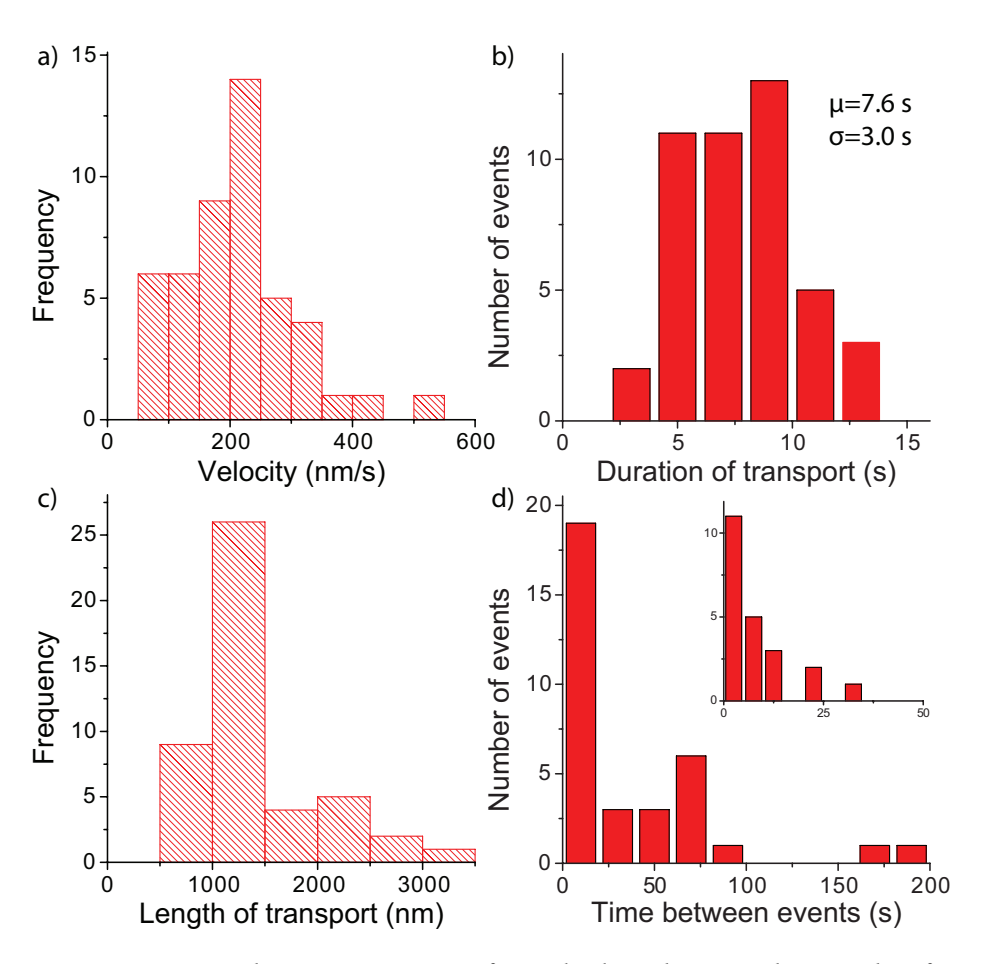


Figure 4.8: Directed transport statistics for multiple endosomes showing data from all the parts of the endosome trajectories where directed transport in the axial direction (along the apicobasal axis) was observed. a) Distribution of velocities. b) Distribution of duration of the detected directed motion, with an average $\mu=7.6$ s and standard deviation $\sigma=3.0$ s. c) Distribution of total distance covered by each transport event. d) Distribution of the time between transport events. The inset shows a zoom of the histogram for the data where time between events < 50 s.

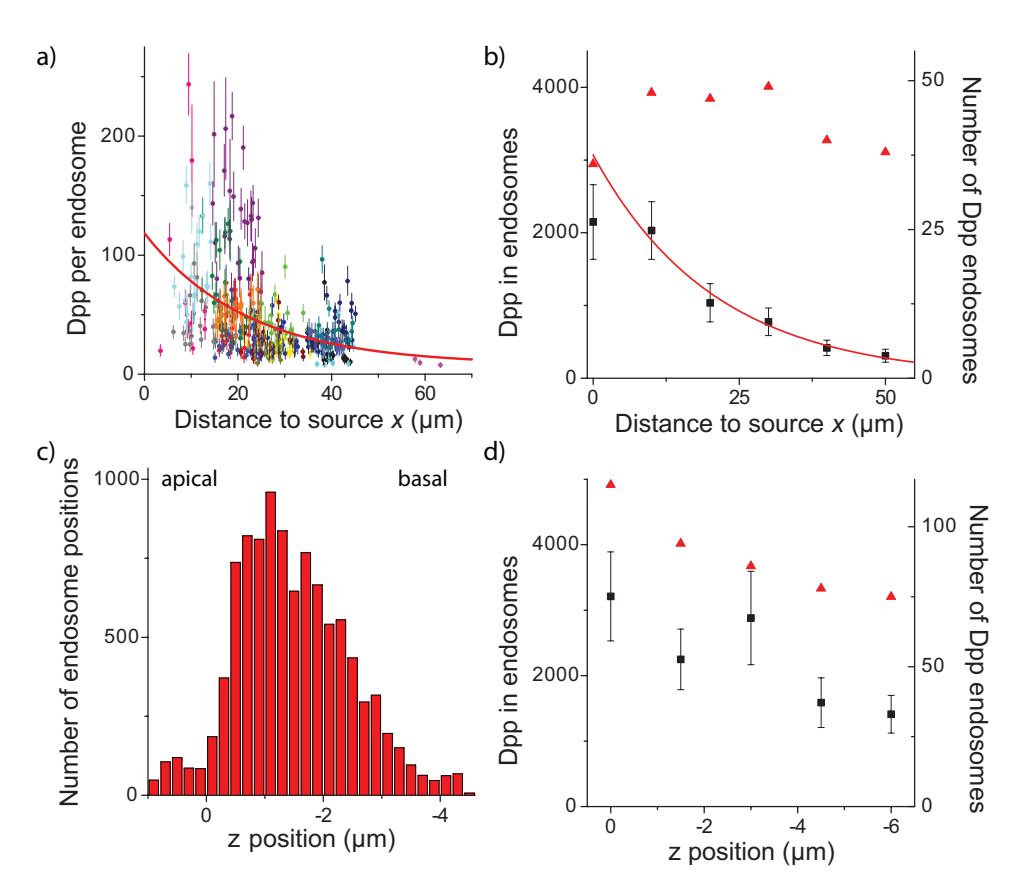


Figure 4.9: **a)** Amount of Dpp molecules per endosome plotted versus the distance to the source. Different colors indicate different wing imaginal discs. Fit of a single exponential to the data gives a decay length $\lambda = 22 \pm 9 \,\mu\text{m}$. **b)** Total number of Dpp molecules (black squares) and number of Dpp endosomes (red triangles) in a volume of $10x10x5 \,\mu\text{m}^3$ versus source distance for one wing imaginal disc ($\lambda = 20.8 \pm 3.4 \,\mu\text{m}$). **c)** Apicobasal distribution of Dpp endosomes in the wing imaginal disc. All positions of the detected endosomes in each image stack from an experiment are binned together. The apical edge of the columnar cells is defined as $z = 0 \,\mu\text{m}$. **d)** Apicobasal distribution of Dpp molecules (black squares) and number of Dpp endosomes (red triangles) for the same disc as in **b)**.

4.4 Results-Dpp content of endosomes

4.4.1 Static characterization

The Dpp gradient was measured in wing imaginal discs (N=28) by locating Dpp-containing endosomes relative to the source and determining their Dpp content (fig. 4.9a). Each sample is indicated with a different color, showing the large heterogeneity between different discs. On top of large inter-sample heterogeneity, the number of Dpp molecules per endosome varied enormously within one disc. In one imaginal disc Dpp content was found to be ranging from 21 to 244 Dpp per endosome, a variation of one order of magnitude. Despite this heterogeneity the single-exponential nature of the gradient was visible.

Fitting a single exponential decay to all data in fig. 4.9a (number of endosomes > 500) gave a gradient of decay length $\lambda = 22 \pm 9$ µm, agreeing well with previous experiments where $\lambda = 20.2 \pm 5.7$ µm was found [10]. The average amount of Dpp per endosome at the source (C_0) was determined to be 110 ± 10 Dpp molecules.

To remove the effect of inter-sample heterogeneity the amount of Dpp in only one imaginal disc was measured as a function of the distance to the source (fig. 4.9b, black squares). Images were taken at intervals of 10 μ m and all detected Dpp was summed. The data was fitted to a single-exponential (omitting the data point at x=0 μ m, since the image at that point contained both the Dpp-producing cells as well as the Dpp-receiving cells). The gradient has a decay length $\lambda=20.8\pm3.4$ μ m, which again agrees nicely with previously obtained results.

In the following we analyzed the data in more detail to unravel which underlying property was the source of the Dpp gradient. The observed singleexponential gradient can arise in three different ways:

- 1. The concentration of Dpp per endosome is constant and the number of endosomes per cell decreases further away from the source;
- 2. The opposite, i.e. a constant number of endosomes per cell and a de-

creasing amount of Dpp per endosome versus distance to the source;

3. A combination of 1 and 2.

From a biological point of view (1) seems to be unlikely, since the function of endosomes is not limited to collecting and transporting Dpp. A decrease of number of endosomes further away from the Dpp source would therefore also affect other cellular processes which involve endosomes. The same reasoning qualifies option (3) also as less likely. Furthermore a combination of changing the Dpp concentration and the number of endosomes seems to be a complex way to establish a single-exponential gradient. We therefore predicted that mechanism 2 will be the most likely mecahnism of gradient formation.

We confirmed this experimentally by measuring the average number of detected Dpp-containing endosomes versus distance to the source for the same wing disc as was used before (fig. 4.9b, black squares). The result is plotted in fig. 4.9b (red triangles). Our data show that over a large range (Δx = 19 cells) the number of detected Dpp endosomes stays constant (44 ± 2 Dpp endosomes per 500 μ m³). While previous experiments have shown the presence of a gradient for the whole Dpp population, our results demonstrated that also the endosomal Dpp subpopulation (85% of total Dpp population [10]) faithfully reflects the morphogen gradient, while the number of endosomes that contain Dpp does not change with distance to the source.

Besides the lateral distribution of Dpp we further studied the apicobasal distribution of Dpp endosomes and of Dpp itself. Previously it has been found that most of Dpp is located in the most apical 5 μ m of the wing epithelium [5, 10]. We confirmed this by imaging the most apical 25 μ m of the wing epithelium (data not shown). For one experiment (600 image stacks, lateral size = $10x10~\mu\text{m}^2$, axial size = 5 μ m.) the distribution of the *z*-positions of all detected endosomes during the movie were plotted in fig. 4.9c. In this experiment the majority of the endosomes were clearly confined to a layer of 3 μ m within the tissue. In fig. 4.9d the apicobasl distribution of Dpp (black squares) and the apicobasal distribution of Dpp endosomes (red triangles) is shown for the most apical layer of 5 μ m of the wing disc (distance to the source ranges from 0 μ m till 50 μ m). We again observed that the amount of Dpp is largest

at the most apical side of the cell and decreases basally. Interestingly, also the amount of Dpp endosomes was largest in the most apical part of the cell. The relative decrease of the number of Dpp endosomes however is smaller than the relative decrease of the amount of Dpp. Therefore the average amount of Dpp per endosome is also the highest close to the apical membrane and decreases basally.

4.4.2 Dynamic characterization

As was shown before (fig. 4.5a & fig. 4.7a) Dpp-containing endosomes were followed for up to 600 frames for endosomes with high (>100 Dpp molecules) Dpp content. Such trajetories allowed us to study the fluctuations in the fluorescence signal of individual endosomes. The signal is taken as direct measure for changes in the Dpp concentration in the endosome. However, due to photobleaching, the fluorescence intensity of each endosome will decrease over time which in turn would translate into an apparent reduction of Dpp molecules in the endosome. Hence, to correct for photobleaching we measured for each experiment the average intensity per endosome for every time point, as shown in fig. 4.10a. A bi-exponential decay was subsequently fitted to the data and the curve obtained was in turn used to correct the intensity profile for each individual endosome in retrospect.

Figure 4.10b shows the Dpp content of the endosome versus time in a living wing disc (blue curve) and in a fixed wing disc (red curve) in which supposedly no dynamics took place. For the fixed sample the 2σ confidence interval level for the noise is shown (dashed area) which arises from both photon shot noise (50 % of total noise) as from sources in the sample itself (out-of-focus fluorescence). For the experiment in the live wing disc, data were treated accordingly. In contrast to the data on the fixed wing disc the observed fluctuations clearly fall outside of the 2σ interval and cannot be purely explained by noise. Figure 4.10c and fig. 4.10d show the distribution of the measured intensities for the fixed and the living wing disc endosome, respectively. As predicted, the intensity distribution for the fixed wing disc endosome was fully described by

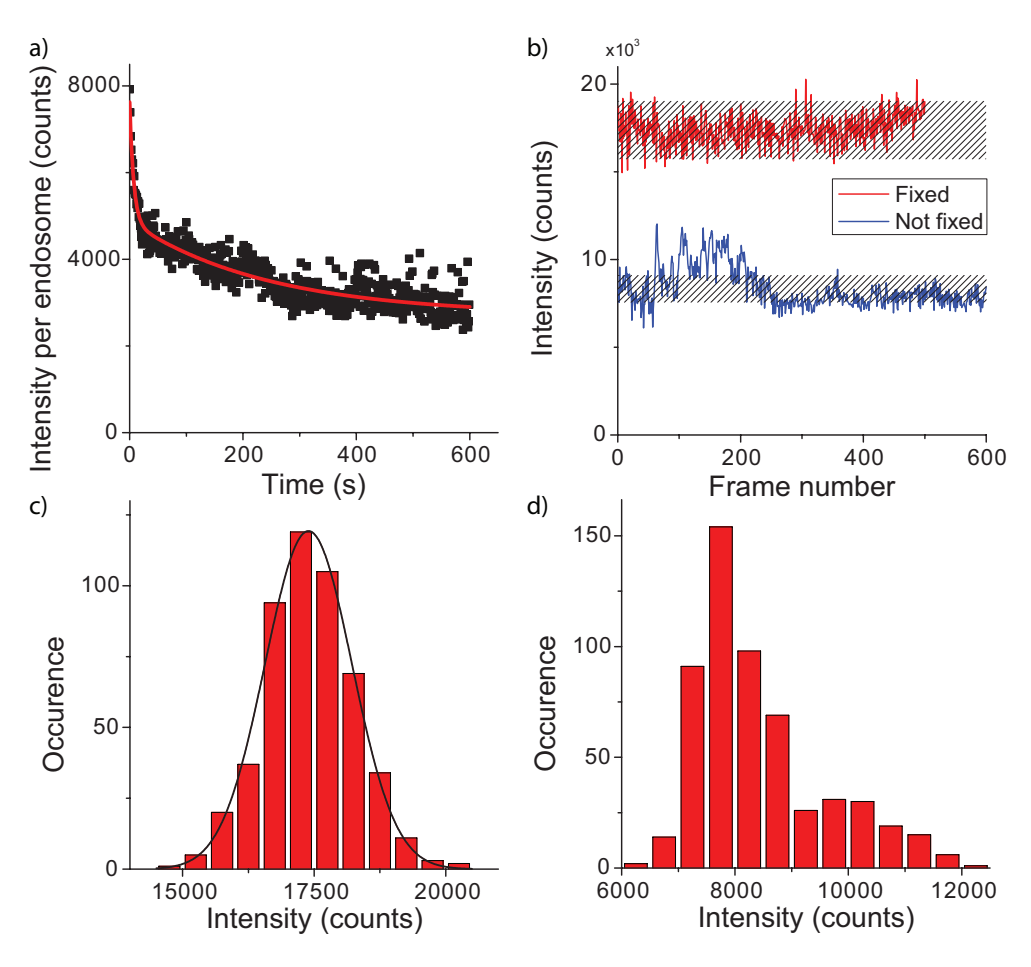


Figure 4.10: a) Average intensity per endosome for each image stack. A bi-exponential is fitted to the data and this curve is used to correct the intensity profile of individual endosomes in this experiment. b) The intensity of two endosomes plotted versus time and corrected for photobleaching. The red curve shows data from an endosome from a wing disc in which all material was fixed. The blue curve shows the intensity of an endosome from a live wing disc (not fixed). The expected noise in the intensity is indicated by the dashed area. c) Histogram of the intensity values of the data from the fixed endosome in (b). As expected the shape of the histogram is Gaussian, and thus the intensity fluctuations are fully explained by noise. d) Histogram of the intensity values of the data from the not-fixed endosome in (b). The shape of the histogram is clearly non-Gaussian, indicating that the intensity fluctuations cannot only be explained by noise.

a Gaussian with $\mu = 17392 \pm 25$ counts and $\sigma = 827 \pm 25$ counts.² The intensity distribution for the non-fixed endosome however, could not be described by a simple Gaussian distribution, supporting the conclusion that the fluctuations are not purely caused by noise, but by Dpp dynamics. Since the noise level in all experiments was on the order of a few Dpp molecules (depending on the total intensity) we conclude that our experimental setup was sensitive enough to directly observe in- and outflow of Dpp from endosomes in small packages of Dpp.

As explained before (section 4.1.1) changes in Dpp concentration in an endosome occur when a vesicle containing Dpp fuses with an endosome (up steps) or when Dpp is removed from an endosome (down steps), see fig. 4.2. By collecting many trajectories of endosomes and their Dpp-concentration profiles we obtained distributions of $C_{\rm endo}$, k_i and c_i . These distributions were subsequently used to make a detailed quantitative description of events in intracellular Dpp transport. It should be noted that in this analysis we could not segment the endosomes according to their type (i.e. early, recycling or late) and the obtained distributions will therefore represent multiple underlying events.

To determine if the events in intracellular transport as described in section 4.1.1 are involving individual Dpp molecules or clusters of Dpp we studied the size of the changes in Dpp concentration for each endosome. For this purpose we obtained Dpp concentration profiles for each individual endosome (an example is shown in fig. 4.11a) and subsequently used a step-fitting algorithm [21] to determine the step size of each event. This has been done for many different endosomes, resulting in 179 'step'-events, the distribution of step sizes is shown in fig. 4.11b. From the result it became clear that both in- and outflow events usually involve clusters of Dpp, with 97% of the events having a Dpp cluster size of 25 or less.

To determine if there was a difference between the Dpp cluster size for Dpp in- or outflow we calculated the average cluster size for both groups. For upsteps we found $\langle \Delta c_{\rm in} \rangle = 8.5 \pm 1.1$ Dpp and for down-steps $\langle \Delta c_{\rm out} \rangle = 6.6 \pm 0.6$

²Although shot noise is Poissonian distributed, it can be approximated by a Gaussian distribution for large values

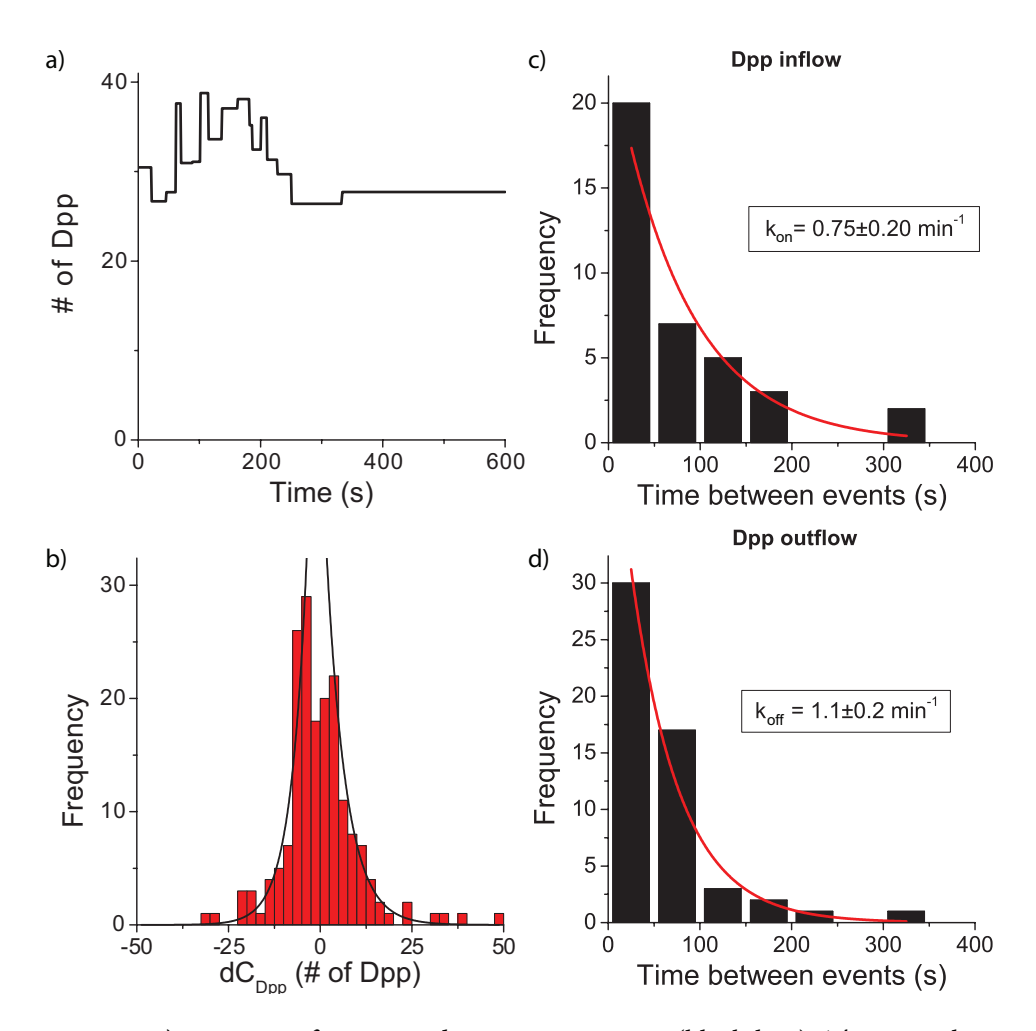


Figure 4.11: **a)** Intensity of a Dpp endosome versus time (black line). The green line shows the result of the applied step-fitting algorithm [21]. **b)** Distribution of step sizes independent of distance to the Dpp source. The size of Dpp steps seems to be exponentially distributed with an average of $\langle \Delta c_{\rm in} \rangle = 8.5 \pm 1.1$ Dpp for Dpp inflow and $\langle \Delta c_{\rm out} \rangle = 6.6 \pm 0.6$ Dpp for Dpp outflow. Small steps (< 2 Dpp) are within the noise and explain the dip in the data at $\Delta c_{\rm endo} = 0$. **c)** Time between fusion events (Dpp inflow). Fitting with a single exponential gives $k_{\rm on} = 0.75 \pm 0.20 \, {\rm min}^{-1}$. **d)** Time between off-events (Dpp outflow). Fitting with a single exponential (first order rate reaction) gives $k_{\rm off} = 1.1 \pm 0.2 \, {\rm min}^{-1}$.

Dpp. Hence, inflow is characterized by smaller clusters as compared to Dpp outflow. It should be noted that further conclusions based on the shape of the step-size distribution should be drawn with care. The data was taken at different distances to the Dpp source and therefore the distance distribution of the experiments influences the distribution of observed step sizes (more experiments close to the Dpp source will contain more endosomes with high Dpp content and could result in larger step sizes and vice versa). Furthermore, the distribution is slightly biased to larger step sizes. First, small steps (up to a few Dpp) could not be observed because of noise. Secondly, small steps will be more difficult to detect when the endosome fluorescence has significantly bleached. At that moment only a certain fraction of the Dpp in a 'step-event' will be still fluorescent and therefore become more difficult to detect. The bleach-correction algorithm cannot correct for this since it not only increases the fluorescence to original levels, it also increases the noise associated to it.

The difference between the cluster size for Dpp in- and outflow should be reflected in the frequency of these events, provided that both processes are in equilibrium. Therefore, we measured the time between events of the same type (i.e. inflow-inflow and outflow-outflow) using the output of the step-fitting algorithm. The result is plotted for Dpp inflow (fig. 4.11c) and Dpp outflow (fig. 4.11d). Fitting a single exponential yielded $k_{\rm on}=0.75\pm0.20~{\rm min^{-1}}$ and $k_{\rm off}=1.1\pm0.2~{\rm min^{-1}}$. The average outflow rate $\langle\Delta c_{\rm out}\rangle k_{\rm off}=7.3~{\rm Dpp/min}$ hence equals (within the margin of error) the average inflow rate $\langle\Delta c_{\rm in}\rangle k_{\rm on}=6.4~{\rm Dpp/min}$, showing that the system is in a steady state indeed. It should be noted that the distributions in figs. 4.11c,d are probably biased towards longer times, since rapid events involving small changes in Dpp content could not be observed during our experiments.

The obtained values for the in- and outflow rates for individual Dpp are larger than those obtained previously in chapter 3. For the slow limit of intracellular transport (150 s for the whole process) there we found $t_{\rm r,ea}$ = 53 s and $t_{\rm r,r}$ = 100 s for early and recycling endosomes, respectively (with an average $t_{\rm r}$ = 77 s), while here we find $t_{\rm r}$ = 8.2 s. These numbers however do not represent the same parameter of the model. Here we analyzed the time between events, which in itself does not allow us to conclude on the residence time

of Dpp in endosomes, which was calculated in chapter 3. The time between events also depends on the number of Dpp in the endosome. The more Dpp in an endosome, the shorter the time between events for the same residence time. Hence, from the difference between the values we can predict that there should be 77/8.2 = 9 Dpp molecules on average per endosome in our experiments.

We found however that the endosomes in which we observed Dpp-concentration changes, had an average Dpp content of 77 ± 7 Dpp molecules. From this we concluded that 88% of the Dpp in endosomes appeared to be immobile on the timescale of our experiments. This immobile fraction of Dpp has been detected before by FRAP experiments, where it was determined to be $62\pm8\%$ [10]. We suggest that the rest of the difference between the FRAP experiments and our experiments is explained by experimental limitations, which prevented us from seeing small changes in Dpp concentration.

The model presented before (fig. 4.2) contains six events which all could result in the Dpp concentration changes observed. At the same time the model reveals three redundant parameters ($-c_2 = c_3 + c_4$) which involve vesicle transport between endosomes. Therefore they will appear both as up-steps and as down-steps in fig. 4.11b, assuming there is no change in vesicle composition during the transport between endosomes. As a result we rule out events 2, 3 & 4 (i.e. fission of a vesicle containing Dpp from an early endosome which is transported either to a recyling endosome or a late endosome) as possible contributors to the difference between up- and down-steps. The observed difference can therefore only arise from a difference in the number of Dpp molecules that are endocytosed in one step on one hand, and that are recycled and/or degraded on the other hand.

In fig. 4.11d we analyzed the time between fission events. As predicted for a first-order reaction the distribution followed a single-exponential decay. Such first-order reaction (i.e. fission from an early, recycling or late endosome) is summarized in:

Endosome
$$\rightarrow$$
 Endosome + Dpp-vesicle (4.5)

As was shown in chapter 3 the fraction ε of Dpp transferred from an early endosome to a recycling endosome determines the decay length λ of the gra-

dient. Hence, for a well defined gradient it is necessary to keep ε stable. This could be achieved by an active process in the early endosome in which vesicles are predestined to be transferred to a recycling endosome or a late endosome. Since 99.6% of Dpp is transferred to a recycling endosome, in this hypothetical active process, a controlled threshold in Dpp concentration needs to be reached before a vesicle with Dpp leaves the endosome. In a passive process on the other hand the amount of Dpp in the vesicle would be proportional to the Dpp content of the endosome and ε (and hence the gradient) would be statistical.

To distinguish between the two possible processes we calculated the relative step size of all the down-steps. Figure 4.12a shows the distribution of the Dpp concentration in endosomes ($C_{\rm endo}$) just before an outflow-event took place. The distribution is clearly peaked around 30 Dpp molecules. The distribution of step sizes of the down-steps ($dC_{\rm endo}$) is shown in fig. 4.12b which shows a resemblance to fig. 4.12a. The latter observation can be best seen in the relative step size $\frac{dC_{\rm endo}}{C_{\rm endo}}$ distribution (fig. 4.12c). The distribution is sharply peaked at 0.11, hence in each event 11% of the Dpp content is exchanged. At first sight we concluded from this that the off-events are passive events. However, since the data was slightly biased towards larger step sizes, a fraction of the small relative changes will automatically not appear in fig. 4.12c. Hence, from this data alone we could not rule out that there is still an active process that decides how many Dpp is transferred to a vesicle during a fission event.

Therefore we also analyzed the step sizes versus distance to the Dpp-source. As a consequence of the single exponential distribution of $C_{\rm endo}$ (fig. 4.9a) and a constant relative step size, the absolute step size $dC_{\rm endo}$ should become smaller further away from the source in a passive model. Figure 4.12d shows $dC_{\rm endo}$ as a function of the distance to the source. Fitting a straight line to the data indeed confirmed that $dC_{\rm endo}$ became smaller further away from the source. Fitting a single exponential decay did not significantly improve the fit. Averaging the data (fig. 4.12e) showed that both off-steps and on-steps are smaller further away from the source.

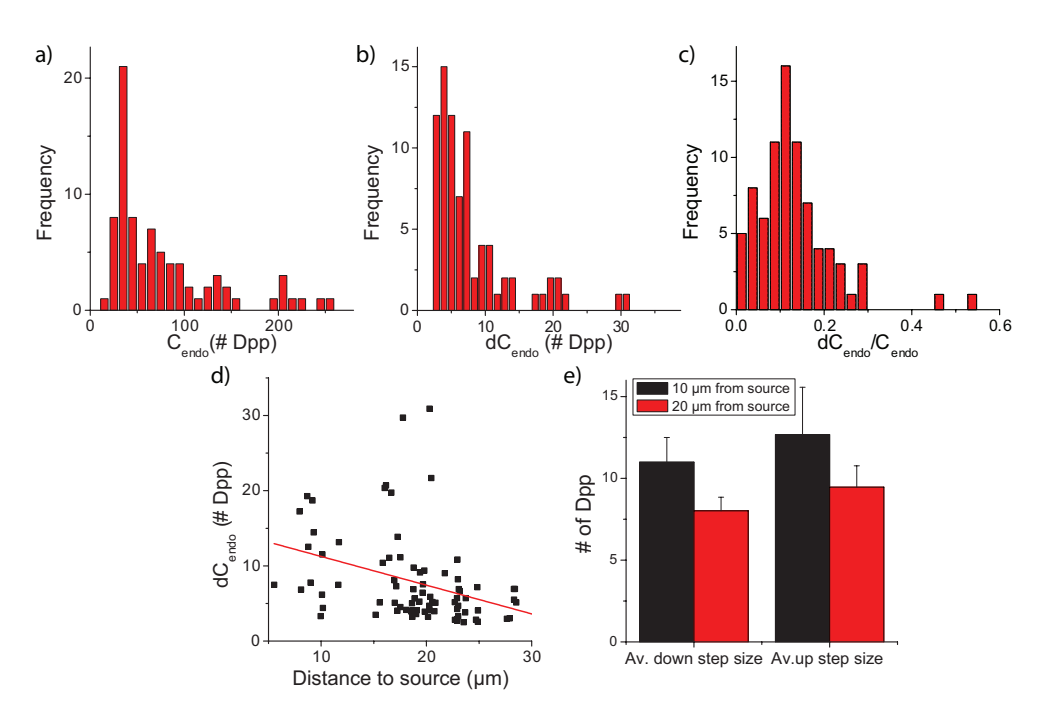


Figure 4.12: **a)** Distribution of Dpp concentration ($C_{\rm endo}$) in endosomes that undergo an off event. **b)** Distribution of step sizes ($dC_{\rm endo}$) in off events. **c)** Histogram showing the distribution of relative step sizes ($\frac{dC_{\rm endo}}{C_{\rm endo}}$) The distribution is peaked around 0.11. **d)** Step size plotted as a function of distance to the source. The red line shows a fit to the data. **e)** Average step size plotted versus distance to the source for both up and down steps.

4.5 Conclusion 113

4.5 Conclusion

In conclusion we found that the motility of endosomes by itself cannot account for intracellular transport, the observed diffusion constants are too low and almost no lateral active transport occurs. Our observation of regular active transport along the apicobasal axis seems to suggest that endosomal transport takes part in Dpp breakdown.

Static characterization of endosomal Dpp content showed that the number of Dpp-containing endosomes does not vary along the Dpp gradient. The Dpp concentration in those endosomes however becomes smaller further away from the source. From the apicobasal distribution of Dpp endosomes we found that both the number of endosomes and the Dpp content in endosomes is smaller more basally in the tissue.

Intracellular transport of Dpp is governed by small vesicles, which travel between endosomes. Those vesicles contained up to 25 Dpp molecules. Dpp inflow happened in larger cluster sizes than Dpp outflow. From this we concluded that the number of Dpp molecules endocytosed in one step is larger compared to the number of Dpp molecules that is recycled or degraded in one step.

The time between fusion of vesicles with an endosome was about 1 minute on average. A similar value was found for time between fission of vesicles from an endosome. In combination with the results from chapter 3 we found that 88% of Dpp appears to be immobile on the timescale of our experiments, hereby supporting previous FRAP experiments. Control of the vesicle concentration is a result of a passive, probabilistic process.

The quantitative information we obtained on vesicular transport here will have to be integrated in the future into more detailed models to describe the intracellular transport that controls morphogen spreading in tissue and animal development.

Bibliography

- [1] Turing, A. Philos T Roy Soc B **237**(641):37–72 (1952).
- [2] Wolpert, L. J Theor Biol 25(1):1–47 (1969).
- [3] Crick, F. Nature **225**(5231):420–2 (1970).
- [4] Kerszberg, M. and Wolpert, L. J Theor Biol 191(1):103–14 (1998).
- [5] Entchev, E., Schwabedissen, A., and González-Gaitán, M. *Cell* **103**(6):981–91 (2000).
- [6] González-Gaitán, M. Nat Rev Mol Cell Biol 4(3):213-24 (2003).
- [7] Kruse, K., Pantazis, P., Bollenbach, T., Jülicher, F., and González-Gaitán, M. *Development* **131**(19):4843–4856 (2004).
- [8] Basler, K. and Struhl, G. Nature 368(6468):208–14 (1994).
- [9] Teleman, A. A. and Cohen, S. M. Cell 103(6):971-80 (2000).
- [10] Kicheva, A., Pantazis, P., Bollenbach, T., Kalaidzidis, Y., Bittig, T., Jülicher, F., and González-Gaitán, M. *Science* **315**(5811):521–5 (2007).
- [11] Bollenbach, T., Kruse, K., Pantazis, P., González-Gaitán, M., and Jülicher, F. *Phys.Rev.Lett.* **94**(1):018103 (2005).
- [12] Bollenbach, T., Kruse, K., Pantazis, P., González-Gaitán, M., and Jülicher, F. *Physical Review e* **75**(1):011901 (2007).
- [13] Lander, A., Nie, Q., and Wan, F. Developmental Cell 2(6):785-796 (2002).
- [14] Lommerse, P. H. M., Vastenhoud, K., Pirinen, N. J., Magee, A. I., Spaink, H. P., and Schmidt, T. *Biophys J* 91(3):1090–7 (2006).

116 BIBLIOGRAPHY

[15] de Keijzer, S., Sergé, A., van Hemert, F., Lommerse, P. H. M., Lamers, G. E. M., Spaink, H. P., Schmidt, T., and Snaar-Jagaiska, B. E. *Journal of Cell Science* 121(10):1750-7 (2008).

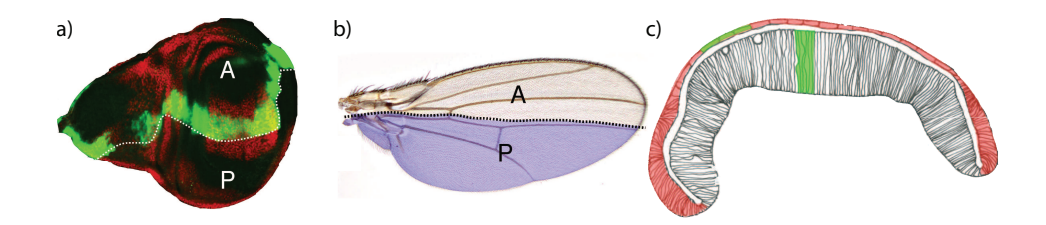
- [16] Nagai, T., Ibata, K., Park, E. S., Kubota, M., Mikoshiba, K., and Miyawaki, A. *Nat Biotechnol* 20(1):87–90 (2002).
- [17] Holtzer, L., Meckel, T., and Schmidt, T. Applied Physics Letters **90**(5):053902 (2007).
- [18] Harms, G. S., Cognet, L., Lommerse, P. H. M., Blab, G. A., and Schmidt, T. *Biophys J* **80**(5):2396–408 (2001).
- [19] Steinmeyer, R., Noskov, A., Krasel, C., Weber, I., Dees, C., and Harms, G. S. *Journal of Fluorescence* **15**(5):707–21 (2005).
- [20] Ajo-Franklin, C. M., Drubin, D. A., Eskin, J. A., Gee, E. P. S., Landgraf, D., Phillips, I., and Silver, P. A. *Genes Dev* 21(18):2271–6 (2007).
- [21] Kerssemakers, J. W. J., Munteanu, E. L., Laan, L., Noetzel, T. L., Janson, M. E., and Dogterom, M. *Nature* **442**(7103):709–12 (2006).
- [22] Carter, B. C., Vershinin, M., and Gross, S. P. *Biophys J* **94**(1):306–19 (2008).
- [23] Huet, S., Karatekin, E., Tran, V., Fanget, I., Cribier, S., and Henry, J. *Bio-phys J* **91**(9):3542–3559 (2006).
- [24] Saxton, M. and Jacobson, K. Annu.Rev.Biophys.Biomol.Struct. 26:373–399 (1997).
- [25] González-Gaitán, M. Mech Dev 120(11):1265-82 (2003).
- [26] Seisenberger, G., Ried, M. U., Endress, T., Büning, H., Hallek, M., and Bräuchle, C. *Science* **294**(5548):1929–32 (2001).
- [27] Kural, C., Kim, H., Syed, S., Goshima, G., Gelfand, V., and Selvin, P. R. *Science* **308**(5727):1469–1472 (2005).

Groei en ontwikkeling. Elk organisme, of het nu een mens, een plant of een bacterie is, heeft ermee te maken. Het is zelfs zo belangrijk dat leven simpelweg niet zou kunnen bestaan zonder groei en ontwikkeling. Ze zijn zo vanzelfsprekend dat niemand er raar van opkijkt wanneer een pasgeboren baby enkele weken later al centimeters is gegroeid en diezelfde baby na een paar jaar al behoorlijk kan praten. Als we echter wat verder kijken blijken de processen die groei en ontwikkeling mogelijk maken uiterst complex. Er zijn duizenden verschillende processen die er uiteindelijk voor zorgen dat een enkele bevruchte eicel uitgroeit tot een volwassen mens. Door deze grote hoeveelheid aan processen lijkt het een onbegonnen werk om groei en ontwikkeling te doorgronden.

De ontwikkelingsbiologie is de tak van wetenschap die de groei en ontwikkeling van organismen bestudeert en deze probeert te begrijpen. De ontwikkelingsbiologie is al erg oud; Leonardo da Vinci was in de 16e eeuw al geïnteresseerd in de groei van de menselijke foetus en maakte er tekeningen van. Tegenwoordig bestuderen we groei en ontwikkeling steeds vaker door naar processen te kijken die zich op cellulair en subcellulair niveau afspelen. De ontwikkelingsbiologie is hierbij in drie hoofdgebieden in te delen. Die houden zich bezig met:

- de groei van cellen;
- de differentiatie van cellen;
- de vorm en structuur van weefsel, organen en volledige organismen, ook wel morfogenese genoemd.

In dit proefschrift houden we ons met dit laatste gebied bezig. Eén van de belangrijke vragen in de morfogenese is hoe een cel weet waar hij zich bevindt. Een niercel heeft immers een andere functie dan een hersencel, terwijl alle cellen in een organisme toch hetzelfde genetische programma (DNA) hebben. En

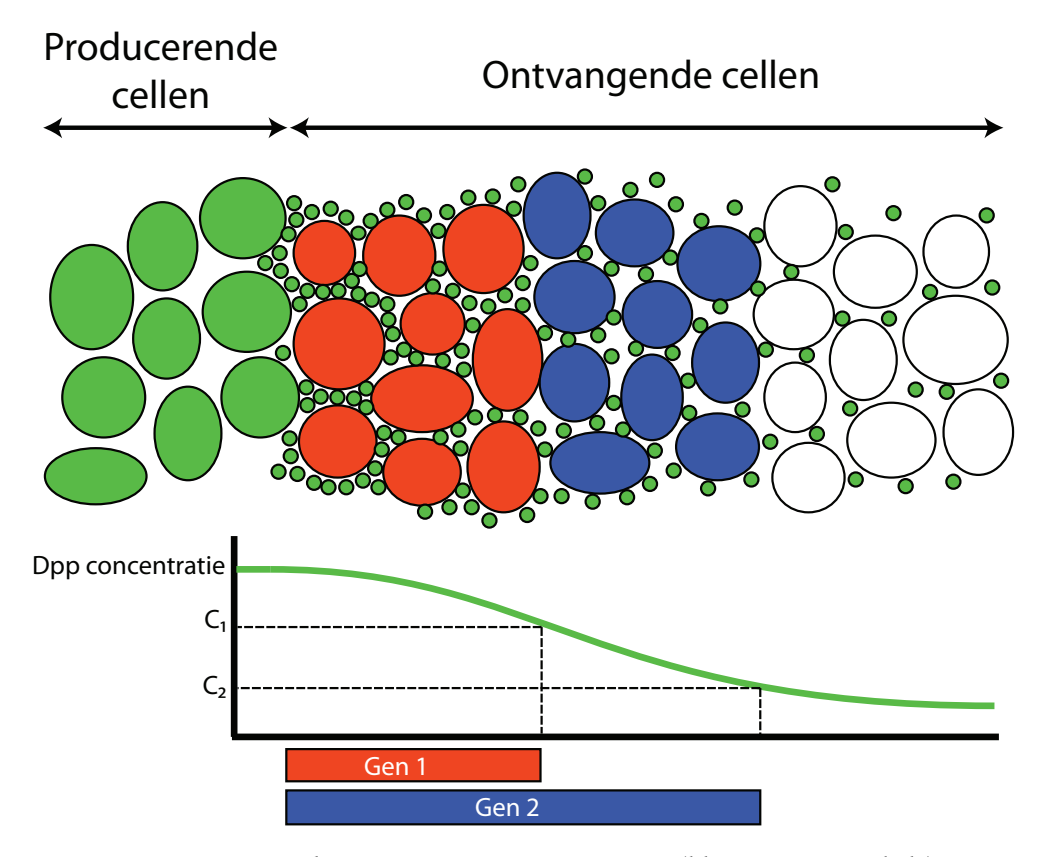


Figuur 5.1: De 'imaginal disc' van de vleugel van de fruitvlieg. **a**) Bovenaanzicht van de imaginal disc. De disc is ongeveer een halve millimeter lang. Dpp is met groen aangegeven, de producerende cellen zijn duidelijk zichtbaar. **b**) De vleugel van een volwassen fruitvlieg. **c**) Een dwarsdoorsnede van de imaginal disc over de lijn van A (anterior) naar P (posterior) in figuur (a). De twee lagen cellen zijn duidelijk zichtbaar. De Dpp-producerende cellen zijn met groen aangegeven.

wanneer zo'n cel eenmaal weet in welk orgaan hij zich bevindt, is het ook nog van belang of hij zich in het midden of aan de rand van het orgaan bevindt. Dit laatste is precies wat we in dit proefschrift hebben bestudeerd.

We hebben hiervoor een modelsysteem gebruikt: de 'imaginal disc' van de vleugel van de fruitvlieg (*Drosophila melanogaster*). Deze 'imaginal disc' is een schijf (fig. 5.1a) in de larve van de fruitvlieg en wordt na de verpopping een vleugel (fig. 5.1b) van de volwassen vlieg. De schijf bestaat uit twee lagen cellen. De bovenste laag bevat grote, platte cellen en de onderste laag bestaat uit langgerekte, kolomvormige cellen. Figuur 5.1c toont een dwarsdoorsnede van de 'imaginal disc', waarin de twee lagen cellen duidelijk te zien zijn.

Voor de kolomvormige cellen is het van belang om te weten waar ze zich in de 'imaginal disc' bevinden. De aderen die zich in de volwassen vleugel bevinden (zoals te zien in figuur 5.1b) moeten bijvoorbeeld op specifieke locaties worden aangelegd. Het eiwit Dpp (Decapentaplegic) speelt een belangrijke rol in de positiebepaling van de kolomvormige cellen in de 'imaginal disc'. Dpp is een *morfogeen*, een molecuul dat aan cellen informatie geeft over hun positie. In het midden van de schijf bevindt zich een band van kolomvormige cellen waarin productie van Dpp plaatsvindt. In figuur 5.1a en 5.1c zijn deze producerende cellen met groen aangegeven.



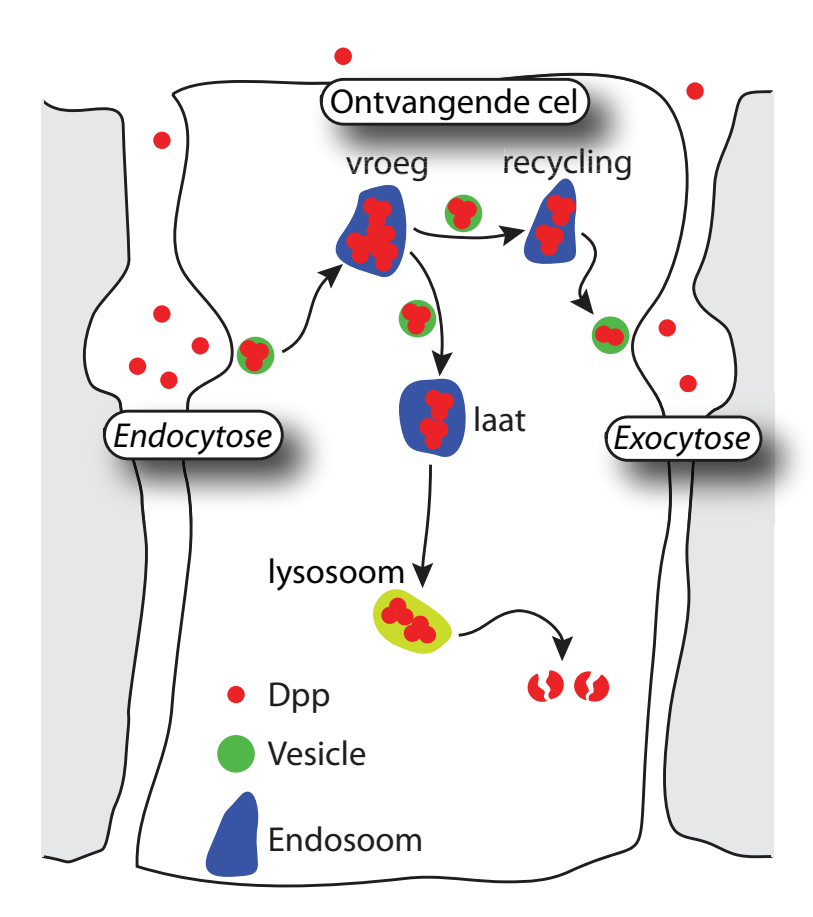
Figuur 5.2: De Dpp-gradient. De concentratie van Dpp (kleine groene cirkels) neemt af naarmate de afstand tot de producerende cellen (aangegeven met groen) groter wordt. Afhankelijk van de Dpp-concentratie worden bepaalde genen wel of niet tot expressie gebracht. Dit leidt vervolgens tot wel of geen productie van bepaalde eiwitten.

Alle kolomvormige cellen die geen Dpp produceren, noemen we de ontvangende cellen. Door de producerende cellen wordt Dpp uitgezonden naar de ontvangende cellen. Het Dpp verspreidt zich vervolgens over de hele schijf en vormt zo een concentratie-gradiënt, zoals te zien in figuur 5.2. Hoe verder cellen zich van de Dpp-bron bevinden, hoe lager de Dpp-concentratie op hun positie. De ontvangende cellen kunnen deze Dpp-concentratie meten en afhankelijk van de concentratie produceren ze bepaalde eiwitten wel of niet.

In dit proefschrift hebben we bestudeerd hoe Dpp van de producerende cellen naar de ontvangende cellen wordt getransporteerd. Er zijn drie verschillende transportmechanismen bekend, waarvan wij er één onderzochten: het intracellulaire Dpp-transport. Figuur 5.3 toont een schematische weergave van intracellulair Dpp-transport voor één cel. Via een proces dat we *endocytose* noemen, neemt de cel Dpp op. Vervolgens wordt het Dpp door verschillende *endosomen* geleid. Endosomen zijn de verdeelstations van de cel. Na opname van Dpp door de cel transporteren vesicles (een kleinere variant van endosomen) het Dpp naar een 'vroeg' endosoom. Vervolgens zijn er twee mogelijkheden: (i) Dpp gaat weer de cel uit via een 'recycling'-endosoom en aansluitend vindt *exocytose* plaats, waarna de hele cyclus weer opnieuw kan beginnen, óf (ii) Dpp gaat naar een 'laat' endosome, waarna het gedegradeerd wordt in een *lysosoom*.

Om te begrijpen hoe dit intracellulaire Dpp werkt volgden we individuele Dpp-moleculen met een fluorescentiemicroscoop. Daarvoor hebben we een geel fluorescent eiwit met het Dpp gefuseerd. Wanneer we er dan met een groene laser op schijnen, zendt het Dpp een gele kleur uit. Op die manier kunnen we, zonder het weefsel te beschadigen, elke seconde een foto maken van de Dpp-moleculen in de schijf. Uiteindelijk hebben we op deze manier filmpjes gemaakt van zo'n 10 minuten per stuk.

Tot nu toe was over de verschillende stappen van intracellulair Dpp-transport vooral kwalitatieve informatie beschikbaar. Met behulp van onze filmpjes hebben we vervolgens deze processen kwantitatief beschreven. Voorbeelden van deze processen zijn hoe lang een Dpp-molecuul zich in een bepaald endosoom bevindt, met welke snelheden de endosomen zich bewegen, hoe groot de groepjes zijn waarin Dpp in vesicles getransporteerd wordt en of dit afhangt



Figuur 5.3: Schematische weergave van intracellulair Dpp-transport in een ontvangende cel. Via endocytose wordt Dpp opgenomen door de cel. Kleine vesicles transporteren het vervolgens naar een 'vroeg' endosoom. Vanuit dit vroeg endosoom gaat het Dpp vervolgens naar een 'recycling'-endosoom of een 'laat' endosoom. In het eerste geval gaat Dpp uiteindelijk weer de cel uit via exocytose, waarna de hele cyclus weer opnieuw kan beginnen. In het tweede geval (het laat endosoom) betekent dit het einde van het Dpp-molecuul: degradatie vindt plaats in een lysosoom.

van de hoeveelheid Dpp in een endosoom.

Omdat fluorescentiemicroscopen nog niet erg geschikt waren om snel eiwitten in drie dimensies te volgen bedachten we eerst een methode om dit wel mogelijk te maken. **Hoofdstuk 2** beschrijft deze techniek. Ook bepaalden we op verschillende manieren wat de eigenschappen van deze nieuwe techniek zijn. De nauwkeurigheid van de positiebepaling van individuele moleculen hebben we zowel theoretisch, met simulaties als met experimenten vastgesteld. Met fluorescente deeltjes in levende cellen toonden we vervolgens aan dat de microscoop geschikt is om biologische vraagstukken aan te pakken. Deze 3D-microscoop was dus ook erg geschikt om op een kwantitatieve manier het intracellulaire transport van Dpp te bestuderen.

In **hoofdstuk** 3 bekeken we hoe lang Dpp zich in de 'vroege' en in de 'recycling'-endosomen bevindt. Daarvoor hebben we de vroege endosomen ook fluorescent gemaakt, maar met een andere kleur dan het Dpp. Met een nieuw experimenteel algoritme, Particle Image Cross-Correlation Spectroscopy, bepaalden we vervolgens nauwkeurig hoeveel procent van de Dpp-moleculen zich in de vroege endosomen bevond. Met behulp van een model vonden we dat een Dpp-molecul gemiddeld korter in een vroeg endosoom zit dan in een recycling-endosoom. Ook ontdekten we dat vroege endosomen gemiddeld twee keer zoveel Dpp bevatten als andere endosomen.

Hoofdstuk 4 behandelt twee andere aspecten van intracellulair Dpp-transport. Eerst keken we naar de mobiliteit van endosomen en welke rol deze speelt in Dpp-transport. Hiervoor volgden we de 3D-positie van endosomen met Dpp gedurende een lange tijd. Hieruit bleek dat endosomen veel te langzaam bewegen om een effectief transportmiddel te zijn voor Dpp. Blijkbaar is dus het transport dat tussen de verschillende endosomen plaatsvindt hiervoor belangrijker. Dit transport tussen de endosomen wordt gefaciliteerd door de eerdergenoemde 'vesicles'. In onze experimenten konden we deze vesicles helaas niet zien.

Om toch meer te weten te komen over dit aspect van Dpp-transport, keken we naar de hoeveelheid Dpp-moleculen in endosomen en hoe dit verandert in de tijd. Hieruit bleek dat de hoeveelheid Dpp in endosomen stapsgewijs verandert en dat deze stappen vaak meerdere Dpp-moleculen groot zijn. Dpp wordt

dus blijkbaar in clusters opgenomen door cellen en dus ook in clusters getransporteerd tussen de endosomen. Verder vonden we ook dat uitstroom van Dpp uit endosomen een passief proces is en lineair afhankelijk is van de hoeveelheid Dpp in het endosoom. Er is dus geen bepaalde drempelwaarde nodig voordat Dpp uitstroom plaatsvindt. Met de kennis uit hoofdstuk 3 bepaalden we vervolgens dat een deel van het Dpp niet mobiel is en dus niet getransporteerd wordt op korte tijdschalen.

Samenvattend heeft dit onderzoek geleid tot een nieuwe experimentele techniek waarmee biologische processen bestudeerd kunnen worden. Met behulp van deze techniek verkregen we meer inzicht in de subcellulaire processen die een rol spelen in het intracellulaire transport van Dpp. Hiermee is dit werk een van de eerste onderzoeken die deze processen kwantitatief beschrijft. Ook heeft het bijgedragen aan een verbeterd inzicht in de processen die een rol spelen bij de groei en ontwikkeling van organismen.

Curriculum Vitae

Laurent Holtzer werd geboren op 17 juni 1980 te Steenbergen (NB). Hij behaalde zijn gymnasium diploma in 1998 aan het 'R.K. Gymnasium Juvenaat H. Hart' te Bergen op Zoom. Daarna begon hij aan de studie technische natuurkunde aan de Technische Universiteit Delft. Tijdens deze opleiding liep hij tien weken stage bij Olympus Optical in Hachioji, Japan. Hij rondde zijn studie af in 2005 met een afstudeeronderzoek in de moleculaire biofysica groep van Prof. Dr. C. Dekker aan de Technische Universiteit Delft. In juni 2005 startte hij zijn promotie onderzoek in de groep 'Fysica van Levensprocessen' van Prof. Dr. T. Schmidt aan de Universiteit Leiden. De resultaten van dit promotie onderzoek zijn beschreven in dit proefschrift. In 2009 ontving hij de 'CSF award for best presentation by a junior researcher' tijdens de IPCAT (Information Processing in Cells And Tissue) conferentie in Ascona, Zwitserland. Na het behalen van de graad van doctor zal Laurent als postdoctoraal onderzoeker werken aan de afdeling Biochemie van de Université de Genève in Zwitserland. Hij gaat daar onderzoek doen naar de groei van de vin van de zebravis in de ontwikkelingsbiologie groep van Prof. Dr. M. González-Gaitán.

List of Publications

Articles

Anna Kicheva*, **Laurent Holtzer***, Ortrud Wartlick, Thomas Schmidt, Marcos González-Gaitán. Quantitative imaging of morphogen gradients in Drosophila imaginal discs. in 'Imaging in Developmental Biology: A Laboratory Manual', CSHL, *submitted* (*equal contribution).

Laurent Holtzer, Thomas Schmidt. Single-Molecule Tracking in Cells and Tissue. in 'Single Particle Tracking and Single Molecule Energy Transfer: Applications in the Bio and Nano Sciences', C. Brauchle, J. Michaelis & D.C. Lamb (eds.), Wiley, *in press* (2009).

Stefan Semrau*, Timon Idema*, **Laurent Holtzer**, Thomas Schmidt, Cornelis Storm. Accurate determination of elastic parameters for multicomponent membranes, Physical Review Letters **100** (8), 088101 (2008) (*equal contribution).

Laurent Holtzer, Tobias Meckel, Thomas Schmidt. Nanometric three-dimensional tracking of individual quantum dots in cells, Applied Physics Letters **90** (5), 053902 (2007).

Fernando Moreno-Herrero, **Laurent Holtzer**, Daniel Koster, Stewart Shuman, Cees Dekker, Nynke Dekker. Atomic force microscopy shows that vaccinia topoisomerase IB generates filaments on DNA in a cooperative fashion, Nucleic Acids Research **33** (18), 5945-5953 (2005).

Laurent Holtzer*, Stefan Semrau*, Marcos González Gaitán, Thomas Schmidt. Intracellular Dpp morphogen transport studied with Particle Image Cross Correlation Spectroscopy (PICCS), *in preparation* (*equal contribution).

Laurent Holtzer, Anna Kicheva, Marcos González-Gaitán, Thomas Schmidt. Endosome motility and endosomal cargo dynamics mediate morphogen gradient formation, *in preparation*.

Dankwoord

De afgelopen vier jaar heb ik met erg veel plezier gewerkt in de groep 'Fysica van Levensprocessen'. Er was altijd ruimte voor wetenschappelijke discussies en als ik een keer hulp nodig had bij een experiment, bij data analyse of iets anders, dan hoefde ik daar nooit lang naar te zoeken. Ook denk ik graag terug aan de inspirerende sfeer op de 10e en 11e verdieping van het Huygens lab. Natuurlijk wil ik ook een aantal mensen specifiek bedanken:

Thomas Schmidt, voor de dagelijkse begeleiding en de vele nuttige discussies die we in de afgelopen jaren hebben gehad. Jij hebt me kennis laten maken met de fluorescentiemicroscopie en later met de ontwikkelingsbiologie, een zeer interessant vakgebied waar ik mij in de toekomst nog verder in wil verdiepen. Wouter van der Meer en Sylvie Olthuis bedank ik voor de ondersteuning in het lab en het verzorgen van de cellijnen. John van Egmond, zonder de fijnmechanische componenten die jij hebt gemaakt, zou mijn opstelling nooit zijn wat hij nu is. Fred Kranenburg, bedankt voor je geduld en hulp als de meetcomputer voor de zoveelste keer was gecrashed. Riet van Nieuwenhuijzen bedank ik voor het secretariële werk op de achtergrond.

Jesper Donsmark, Florian Kulzer en Jante Salverda, jullie hebben me aan het begin van mijn onderzoek de praktische aspecten van de optica bijgebracht. Van jullie heb ik ook het meest vervelende deel van experimenteren geleerd, het 'alignen' van de setup. Tobias Meckel, zo'n twee jaar lang zat je aan het bureau naast me en bestookte ik je regelmatig met allerlei biologische vragen, die je vervolgens ook uitgebreid beantwoordde. John van Noort, voor de altijd kritische vragen die je tijdens de labmeetings stelde.

Anastasia Loman, Anna Pezzarossa, Bram van den Broek, Fan-Tso Chien, Freek van Hemert, Joke van Vugt, Martijn de Jager, Paige Shaklee, Ruth Buning, Thijn van der Heijden, Stefan Semrau, Susanne Fenz en Wiepke Koopmans, jullie bedank ik voor de sfeer op de groep en de vele nuttige wetenschappelijke discussies die we hebben gehad.

Maarten Kruithof, je bent naast oud-collega een goede vriend, bedankt dat

130 Dankwoord

je mijn paranimf wil zijn.

I would also like to thank Marcos González-Gaitán for the fruitful collaboration. During my visits to Dresden and Geneva I have learned about the fascinations of developmental biology. There is still a lot to learn and I am looking forward to join your lab as postdoc. Ani Kicheva, you taught me how to dissect fruit-fly larvae and helped me with many experimental questions I had. Ortrud Wartlick, you took over when Ani left the lab. Franck Coumailleau, Max Fürthauer and Sylvain Loubéry, thanks for the collaboration on the SOP project. I thank all the other people in the González-Gaitán lab for the nice time we had outside working hours. I am looking forward to become one of your colleagues.

Verder wil ik al mijn vrienden bedanken voor hun steun, interesse en gezelligheid. In het bijzonder wil ik noemen: Hessel Winsemius, bedankt dat je op deze speciale dag mijn paranimf wil zijn. Marjolein van Esch, bedankt voor de uren die je in het ontwerp van de kaft van dit proefschrift hebt gestoken.

Tot slot wil ik mijn familie bedanken voor hun onvoorwaardelijke steun. Papa en mama, bedankt voor alle liefde, steun en adviezen. Arjen en Lieke, bedankt voor de gezelligheid in de avonden en weekenden dat ik wél op de Balpol was.